Contents

Strojniški vestnik - Journal of Mechanical Engineering
volume 68, (2022), number 11
Ljubljana, November 2022
ISSN 0039-2480

Published monthly

Papers

Strojniški vestnik - Journal of Mechanical Engineering 68(2022)11, 657-668
DOI:10.5545/sv-jme.2022.255
Original Scientific Paper
Received for review: 2022-06-25
Received revised form: 2022-09-06
Accepted for publication: 2022-10-04

Production of a Design Developed for the Assembly Filter Parts, Optimization of Welding and Field Test

Hakan Maden[1,*] – Kerim Çetinkaya[2]
[1] Ihlas Home Appliance, Turkey
[2] Antalya AKEV University, Faculty of Art and Design, Turkey

For the joining of non-removable plastic parts, methods such as friction welding, friction-stir welding, ultra-sonic welding, chemical joining, and hot-plate welding are used. Rotary friction welding is generally used for joining the filter parts of water treatment devices. After the rotating friction welding of the filter parts, semi-melted agglomerations are formed in the inner parts. To prevent semi-melted accumulation, a weld joint profile design was developed in the ABAQUS software in a previous study. In this study, injection moulds had been produced according to weld joint profile design. The taken plastic presses were welded with the friction welding machine and the joint was controlled and compared. It is seen that the semi-melted agglomeration was successfully confined. By performing Taguchi experimental method and ANOVA analysis on friction welding machine parameters, the optimum pressure conditions were determined in order to carry out static and dynamic tests according to NSF standards and field tests by producing 1500 pilot products, and it has been put into use. The lifetime of the developed filter depends on the material which was used in the manufacture. The next study is aimed to improve the lifetime of the developed filters.
Keywords: rotary friction welding, taguchi experimental method, ANOVA analysis, semi-melt agglomerations, NSF water purification, field test, static and dynamic testing

Highlights
- *The friction-welded profiles of plastic parts have been developed to prevent semi-melt agglomeration stacking.*
- *Comparison of the developed friction-welded profile injection press was made.*
- *The Taguchi experimental method friction welding machine parameter has been applied.*
- *The friction welded parts were field-tested.*

0 INTRODUCTION

The production stages of the plastic part are completed as design work, finite element method analysis (FEM), prototype production, mould-flow analysis, mould making, injection production, standard tests, and mass production. While the defects at the beginning can be corrected at a low cost in these stages, the cost increases as the stages progress. With FEM analysis, the structural defects in the part can be spotted before the material is produced and tested, which reduces the cost. After multiple verifications in the FEM process, the prototyping or moulding stage should be started; otherwise, the cost of correcting defects will be very high.

Parast et al. [1] 3D printed with acrylonitrile butadiene styrene (ABS) and polylactic acid (PLA) materials. ABS/ABS, PLA/PLA, and PLA/ABS were produced utilizing the rotary friction welding (RFW) process. Fatigue tests were performed on PLA and ABS samples. The findings revealed that PLA/PLA joints had superior fatigue resistance to non-welded PLA ones.

Cylindrical parts are made of AA1100 aluminium and H59 brass; combined with RFW. The RFW parameters were friction pressure of 90 MPa and welding time of 15 seconds. They combined the H59 brass material with RFW by preheating (600 K and 873 K). The tensile strength of preheated and non-preheated parts was compared. They found that the part joined by RFW without preheating had a 33 % lower tensile strength (30 MPa) [2].

Bindal et al. [3] combined two polypropylene (PP) materials by using the RFW method. In this joining, they analysed the effects of welding pressure and rotating speed. The joining distance of surfaces reached a maximum value of 64.1 kPa in 14.2 mm at 1100 rpm. Sahu et al. [4] conducted an experimental study of 6 mm thick PP plates using the friction stir welding (FSW) method; they could not blend thermoplastic material with the conical pin. A square pin and the PP plates were successfully welded, according to welds they achieved 59.82 % maximum weld strength productivity. They observed that to obtain a high-strength weld, the assembly rotation and assembly process speed are effective.

Hamade et al. [5] joined the high intensity polyethylene (PE) material at 1224 rpm rotation speed, 40 feed rate, and maximum compressive force at 1085 N by RFW with 13.5 seconds of welding time in their study. They achieved the maximum temperature of

*Corr. Author's Address: Ihlas Home Appliance, Istanbul, Turkey, hakanmaden74@gmail.com

approximately 250 °C which is above the required melting temperature.

Kasman et al. [6] joined AA7075-T651 aluminium alloy plates by the FSW method with tools that had three different pin geometries and using two different rotational speeds; they compared the mechanical property of weld zone and microstructures.

In Saju and Velu's study [7], Inconel 718 and Nimonic 80A materials were joined by electron beam welding (EBW) and RFW methods. The metallurgical and mechanical properties of the joined parts were compared. The radiography test performed on both weld pieces revealed a weld defect. They found that the tensile strength of RFW welded joints was higher than that of EBW welded joints. In contrast, EBW welded joints exhibited higher ductility than RFW welds.

In conventional welding and friction welding (FW) methods, undesirable microstructures are formed due to high peak temperatures and cooling rates. Taysom and Sorensen [8] used different methods for slowing down the cooling and temperature control with the rotary friction welding method. Preheating was done before RFW, and then cooling was slowed down. They found that without temperature and cooling rate control, martensite forms easily after a weld. With temperature and cooling rate control, martensitic transformations are completely prevented, and a pearlitic microstructure has been observed.

Schmicker et al. [9] performed a simulation of RFW metal parts. They designed weld joint profile design and made simulations to trap the semi-melted material that formed in the inner part after welding.

Inline sediment and semi-melted accumulations in the inner part of the activated carbon filters cause premature clogging of the filters and low water flow. The weld joint profile structure was developed using the ABAQUS program to contain semi-melt accumulation. After the welding joint profile structure was developed, the plastic volume mould was revised, and prints were taken on the injection machine. Static and dynamic tests were carried out in accordance with National Sanitation Foundation (NSF) standards to measure the strength of the welded joint profile structure. Then, the Taguchi experimental method was applied to the parameters of the welding machine, and the optimum parameter values were determined. The field test was carried out by making pilot production according to the optimum parameter values determined.

1 SEMI-MELTED ACCUMULATION DEFECTS AFTER FW AND DEVELOPMENT OF WELDING JOINT PROFILE DESIGN

Due to the moulding and assembly errors of the plastic parts inside the sediment filter, the melt accumulation after FW closes the water passage channels in the filter upper cover part and narrows the water passage. While the supposed semi-melted accumulation situation occurs in Fig. 1a, the channels indicated by the red arrows in Fig. 1b cause water passages to be blocked as a result of defects. Post-production controls are made with air, and in these tests, a pass is given as long as there is no complete blockage in the channels. However, problems occur in water passages and low water flow or premature clogging of the filters during the installation at the customer's house

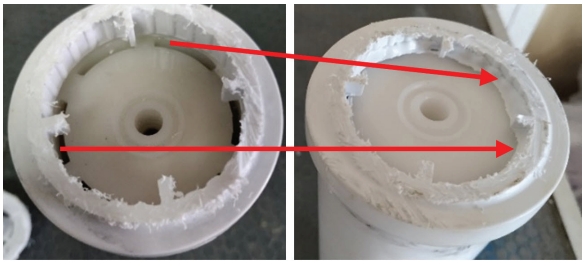

a) b)

Fig. 1. *a) Semi-melted agglomeration situation that should have been a sediment filter, and b) a semi-melted agglomeration situation with a faulty sediment filter*

As a result of the fact that the activated carbon filter body part is small after the plastic injection press and the activated carbon bottom cover part is large after the plastic injection press, the lower cover part is jammed before it is seated on the base. In addition, the active carbon upper cover part cannot be fully seated in the slot due to faulty assembly by the personnel. Because of these, semi-melted agglomeration flows onto the felt in the top cover piece. Fig. 2a shows the semi-melted accumulation state of the activated carbon filter after welding. Due to the printing and assembly error that occurred, the semi-melted agglomeration indicated by the red arrow in Fig. 2b flows and fills the felt. The usage size of the felt, which is Ø60 mm, decreases to approximately Ø50 mm and 30 % is lost.

Fig. 3a shows a vectorial drawing of the currently used weld joint profile design. Fig. 3b shows the half-sectioned state of the existing filter after RFW and the vectorial drawing of the semi-melt agglomeration state. The semi-melted accumulation structure formed after FW was simulated in the ABAQUS program, and the semi-melt accumulation was obtained. Fig. 3c shows the semi-melt agglomeration result of the

ABAQUS analysis. It is seen that the semi-melted accumulation state indicated by the red arrow in Fig. 3 is similar to the structure formed on the piece and the structure made after the analysis.

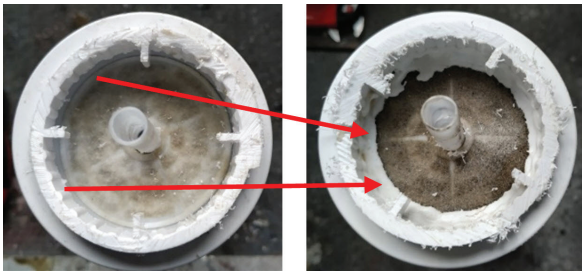

a) b)

Fig. 2. *a) Semi-melted agglomeration situation, which should be an activated carbon filter, and b) activated carbon filter faulty melt accumulation condition*

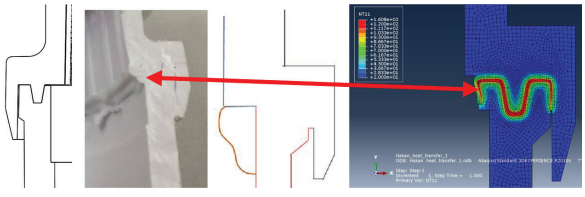

a) b) c)

Fig. 3. *Current part; a) weld joint profile design, b) the semi-melted agglomeration status, and c) the semi-melted agglomeration analysis* **[10]**

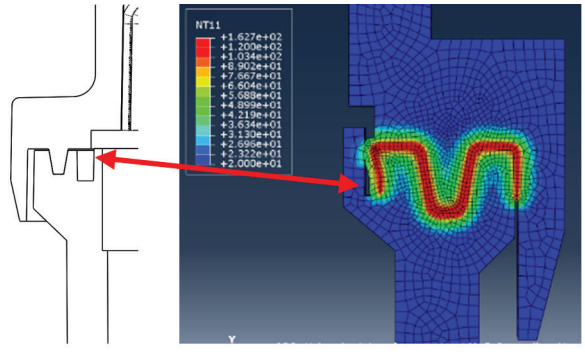

a) b)

Fig. 4. *a) Developed weld joint profile design, and b) the semi-melted agglomeration status analysis of the developed weld zone* **[10]**

In the ABAQUS software, three different weld designs were made to contain the semi-melted accumulation, and the weld joint profile design was developed by making simulations of these weld joint profile designs. Fig. 4a shows the vectorial drawing of design no. 3 weld joint profile design. Fig. 4b shows the design developed weld joint profile design no. 3 and the semi-melted accumulation simulation made in the ABAQUS program **[10]**. As a result of the analysis of the semi-melted accumulation, it is seen that the melt accumulation is successfully confined to the region indicated by the red arrow in Fig. 4.

2 THE MODIFICATION OF THE MOLDS IN ACCORDING TO DEVELOPED WELD JOINT PROFILE DESIGN

The design of the body and cover part of the filter of the developed welding joint profile design has been made. Moldflow analysis has been made to design parts to check defects as well as induction such as filling, merger marks and air voids **[11]**. Modifications have been made for the inline body and cover according to the designed part.

In Fig. 5, the inline body mould is seen. The existing inline body mould has been produced with four pores and inserts in the weld joint profile area. In the inline body mould's only pore, the inserts shown as A and B in Fig. 5 were manufactured and changed according to the developed design. Fig. 5 shows A, the change insert in the cavity side. Fig. 5 shows B, the changed insert on the core side.

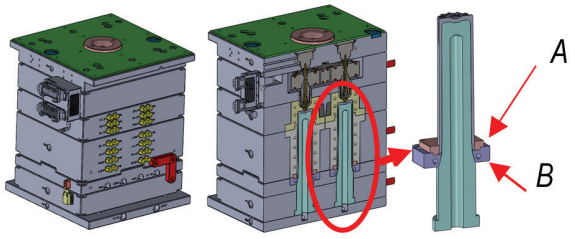

Fig. 5. *Design of the inline body mould*

In Fig. 6, the inline cover mould is seen. The existing inline cover mould has been produced with two pores and inserted in the weld joint profile area. In the inline cover mould only one pore and the six inserts shown as A, B, C, and D in Fig. 6 were manufactured and changed according to the developed design. Fig. 6 shows A, the dynamic Slide 1 piece, B, the dynamic Slide 2 piece, C, the inner core part, and D, the bottom support plate.

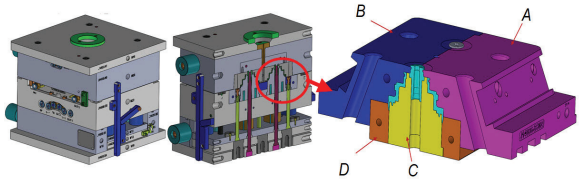

Fig. 6. *Design of the inline cover mould*

3 TAKING THE FIRST PRESS AND FRICTION WELDING

The mould insert parts, which were designed in accordance with the developed weld joint profile design, were manufactured and assembled. Then, the 20 parts in the first press were separated as junk in order to regulate the mould in the injection machine. After that, 300 pieces of inline body and cover parts have been pressed out. The parts pressed from the modified pore were separated, and the parts pressed from the other pore were sent for manufacturing. These parts will be used in the comprising analysis result and friction weld process, the determination of the optimum level of the welding machine, which is made with Taguchi experimental method and in the dynamic tests.

After the first press of the inline cover and body part, the design dimension and the other controls have been made. In the dimensional controls, it was seen that the difference between the design and the printed part was within the acceptable tolerance of DIN16901 [12]. The prints of the inline body and cover part are accepted.

Then, the consistency of the presses with each other us checked. In Fig. 7a, the first press of the inline body and cover can be seen in cut form. Fig. 7b shows the friction welding machine and the assembly of the parts. While the lower part is fixed in the friction welding machine, the upper part moves in both rotational and axial directions.

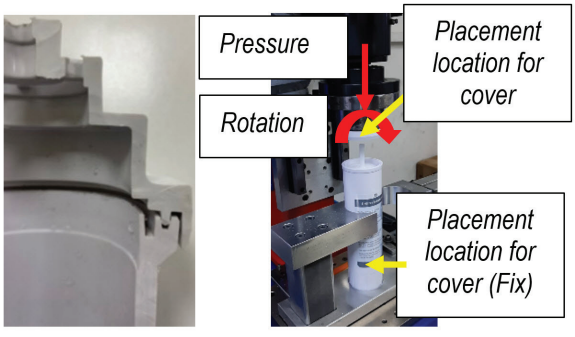

Fig. 7. *a) First press of inline body and cover, and b) friction welding machine and part layout*

Table 1. *The values which entered the friction weld machine are shown*

Input parameter name	Input parameter value
Rotation speed [rpm]	2490
Friction welding pressure [bar]	6
Friction welding duration [s]	2
Waiting time after friction welding [s]	3.5

The inline body cover piece has been joined with 10 pieces of 300 pressed-out pieces by a friction welding machine. The values used in the current production are entered as the welding machine parameter values. In Table 1, the values which entered our friction weld machine are shown.

In Fig. 8, the first press of the inline body and cover joined form are seen. It has been determined that there is no molten accumulation in the inner part of the 10 friction welds.

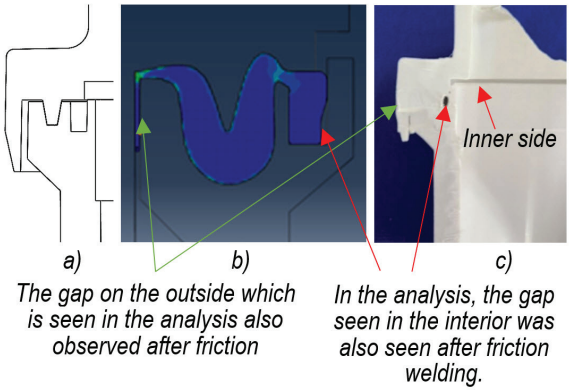

Fig. 8. *a) The design of generally used welding joint profile, b) ABAQUS analysis of weld joint profile with developed design [10], and c) the status of the existing semi-melted accumulation after friction welding*

The inline body and cover parts have been joined with the friction welding process. After the welding process, the cut view piece has been taken and whether there is semi-melted accumulation on the inner side is verified. In Fig. 8c, no semi-melted accumulation on the inner side has been observed. The semi-melted accumulation status acquired with ABAQUS software has been compared with the status of semi-melted accumulation after the welding process. It is observed that the semi-melted accumulation status is close to the structure acquired with the analysis result.

4 IMPLEMENTING TAGUCHI EXPERIMENTAL METHOD TO PARAMETERS OF FRICTION WELDING MACHINE

The Taguchi method is a well-developed experimental technique to determine the most optimum value range for a commonly used process. This method has a significant role in industry, when time and costs are very important. It is a helpful instrument for designing and developing high-quality systems. For these reasons, industries can significantly reduce product development time with the same cost by using the Taguchi method [13].

Van and Nguyen [14] combined AA6061 material by applying FSW. Welding machine parameters were developed by the Taguchi experimental method. The observed findings contributed significant data to determine optimal FSW parameters and enhance welding responses.

Singh et al. [15] combined the rotary friction welding process by adding aluminium and iron powder to plastic parts. Taguchi's experimental method was applied to the data input parameters of the friction welding machine. They found that the parameters combination for the added aluminium powder to the plastic parts is 775 rpm 0.045 rotation per mm with 6 seconds welding time and for the added metal powder to the plastic parts is 1200 rpm, and 0.045 rotation per mm with 8 seconds welding time.

Özçelik [16] optimizes the effects of injection parameters and welding lines on the mechanical properties of PP moulding by using the Taguchi method and regression analysis. Park et al. [17] determined product thickness to prevent welding lines and also optimize the process condition by minimizing the induction press for the automotive fog lights' blind cover.

A chiselling process has been made on a water-jet workbench in accordance with pressure advance rate and abrasive garnet amount of Anti-Proopiomelanocortin (POM-C). To determine the minimized surface roughness, the Taguchi experimental method was implemented. It was determined that on the water-jet workbench with 260 MPa pressure, 35 g/min garnet amount and 170 mm/min advance rate the surface roughness was the minimum rather than the other parameters [18].

The values of the FW machine are as important as the design of the welding structure on the joining quality of the inline body cover part. The Taguchi experimental method was applied to determine the optimum welding machine parameters.

5.1 Determination of Design Parameters

The effects of FW machine values such as rotation speed, friction welding pressure, friction welding time and waiting time on joint quality will be analysed. Minitab 15 [19] statistical software has been used to explain the effects of welding parameters and Taguchi experimental method analyses processes. The Taguchi method finds a solution by combining the three tools orthogonal experimental design, rate of signal/noise (S/N), and analysis of variance (ANOVA) to analyse and evaluate the numeric data [20] and [21].

In Table 2, the FW parameters and levels are shown. From these factors, the rotation speed level values were taken to be close to each other. If the speed is selected higher, it will cause the material to burn due to excessive friction in the weld area or the material structure will turn into an amorphous structure, causing an increase in brittleness. If the speed is selected low, there will not be a complete union because the heating in the weld area will not be excessive. Level values of other parameters were determined according to previous industry experience.

Table 2. *The factors and levels of FW machine*

Factors	Level 1	Level 2	Level 3	Level 4
Rotation speed [rpm] (A)	2310	2400	2490	2580
Friction welding pressure [bar] (B)	4	5	6	7
Friction welding duration [s] (C)	1.5	1.75	2	2.25
Cooldown time [s] (D)	2.5	3	3.5	4

Table 3. *The tests will test according to Taguchi L16 orthogonal*

Test number	Rotation speed (A)	Friction welding pressure (B)	Friction welding duration (C)	Cooldown time (D)
1	2310	4	1.5	2.5
2	2310	5	1.75	3
3	2310	6	2	3.5
4	2310	7	2.25	4
5	2400	4	1.75	3.5
6	2400	5	1.5	4
7	2400	6	2.25	2.5
8	2400	7	2	3
9	2490	4	2	4
10	2490	5	2.25	3.5
11	2490	6	1.5	3
12	2490	7	1.75	2.5
13	2580	4	2.25	3
14	2580	5	2	2.5
15	2580	6	1.75	4
16	2580	7	1.5	3.5

Four different level ranges (A, B, C, and D) were determined for four different parameters entered into the friction welding machine. If it is desired to perform experiments for each level shown in Table 2, 256 experiments from 4^4 are required. With the Taguchi experimental method, it is possible to find the optimum value with 16 experiments. For these factors, the L16 4^4 orthogonal index design was applied to be used in the Taguchi experimental design. After the determination of welding parameters, a Design of Experiments (DOE) has been generated from Taguchi's experimental design and based on L16 4^4

orthogonal matrix as shown in Table 3 [20] and [22] to [24].

The FW machine parameters have been set up as in Table 3 for the tests to be planned according to the L16 index. The machine has been run idle three times to calibrate parameter values. After that, three inline body and cover parts have been joined in accordance with determined parameters before for each of them with welding operation.

5.2 Determination of Durability of Combined Parts in the Parameters Determined According to the L16 Series

For the 16 different products that were welded with FW by considering the different levels of the factors in the experiments, the pressure tests have been made with a static pressure tool. The pressure was increased until each product exploded According to NSF/ANSI 58 5.1.3.2 hydraulic pressure test, in static pressure test value is 20.4 bar, in the dynamic pressure test for 5 seconds with 10.4 bar pressure and for 5 seconds without pressure, it is expected that 100,000 cycles are durable [25]. The pressure values here are accepted as the minimum value. These 16 different products have been tested until explode in the arbor press. In the static pressure test, the parts were tested in a transparent closed container.

The firm design has been developed by the signal-noise rate that was calculated from the values acquired from strategic computer simulation based on experimental design and used Taguchi method DOE orthogonal index [26].

S/N rate is a tool that statistically qualifies the Taguchi method's performance characteristic and a logarithmic function of the requested answer that is defined as an objective function [20] and [27]. In this study, since obtaining the highest pressure values is desirable, the best and highest S/N ratios are used in the equality calculations.

$$S/N = -10 \cdot \log\left(\frac{1}{n} \cdot \sum_{i=1}^{n} \frac{1}{y_i^2}\right). \quad (1)$$

In Eq. (1), y_i is the observed data at the i^{th} experiment and n is the number of experiments.

For each test determined in accordance with Taguchi experimental method, which is in Table 4, three FW processes and for each part the static pressure test has been made at arbor press. For each test number, the average pressure test result made before has been acquired and the S/N value is calculated according to the average value. In Table 4, the strength test results and the S/N values calculated for Minitab 15 software are shown.

Fig. 9. *Static test kit and the maximum pressure strength of 14/1 numbered test*

Table 4. *Tests' strength and S/N values results*

Test number	Rotation speed [rpm] (A)	Friction welding pressure [bar] (B)	Friction welding duration [s] (C)	Duration time [s] (D)	Strength [bar] (E)				S/N [dB]
					Test 1	Test 2	Test 3	Average	
1	2310	4	1.5	2.5	20.42	20.55	20.48	20.48	26.23
2	2310	5	1.75	3	23.73	23.45	23.53	23.57	27.45
3	2310	6	2	3.5	26.41	26.54	26.49	26.48	28.46
4	2310	7	2.25	4	25.86	26.08	26.12	26.02	28.31
5	2400	4	1.75	3.5	23.48	23.87	24.15	23.83	27.55
6	2400	5	1.5	4	24.35	24.67	24.52	24.51	27.79
7	2400	6	2.25	2.5	27.68	27.34	27.63	27.55	28.80
8	2400	7	2	3	27.14	27.32	27.36	27.27	28.72
9	2490	4	2	4	27.22	27.16	27.38	27.25	28.71
10	2490	5	2.25	3.5	28.05	28.41	28.33	28.26	29.03
11	2490	6	1.5	3	27.10	27.36	27.28	27.25	28.71
12	2490	7	1.75	2.5	27.89	27.64	27.75	27.76	28.87
13	2580	4	2.25	3	25.87	25.96	26.14	26.00	28.30
14	2580	5	2	2.5	27.58	27.44	27.62	27.55	28.80
15	2580	6	1.75	4	28.21	28.43	28.71	28.45	29.08
16	2580	7	1.5	3.5	26.32	26.54	26.78	26.54	28.48

In Fig. 9, the kit of arbor press where the static pressure test has been tested, the maximum value of 14/1 numbered combination's durability and the breaking point of the kit after the pressure test has been shown. After the friction welding process, a precise join and residue of a piece have been observed. In the static pressure test, the wall thickness in the weld area is high, so the part bursts from the weak part. The results of the weld structure and part strength test, which were tested with 16 different tests, have been accepted because the test results are higher than the 20.4 bar static pressure value, which is the minimum standard value for NSF/ANSI 58 [25].

5.3 Optimum Induction Parameter Value and ANOVA

ANOVA a statically method used to determine the effects of two or more weld parameters [28]. In the case of determining the significance of the parameters which have effects on performance characteristics as statistical, ANOVA is used. Furthermore, to check the accuracy of test results acquired with the Taguchi method, lastly, a verification test is applied [20] and [21]. When the S/N rate of parameter levels are analysed, the most effective parameter on the strength are respectively rotation speed, the pressure of FW, friction duration and cooldown time has been observed. All factors are at optimal levels when the S/N response-ability is at the highest level [10].

Table 5. *S/N response table of parameter levels*

	Rotation speed (A)	Friction welding pressure (B)	Friction welding duration (C)	Cooldown time (D)
	S/N	S/N	S/N	S/N
Level 1	27.61	27.69	27.80	28.18
Level 2	28.21	28.27	28.24	28.29
Level 3	28.83	28.76	28.67	28.38
Level 4	28.66	28.59	28.61	28.47
Delta	1.22	1.07	0.87	0.30

Table 5 shows the S/N and strength values. The values are determined as the rotation is 2490 rpm, friction welding pressure is 6 bar, friction duration is 2 seconds and cooldown time is 4 seconds for the optimum level values (A3 B3 C3 D4) and friction welding verification part.

ANOVA analysis is necessary for commenting on the S/N values acquired with tests, ANOVA analysis enables seeing more clearly the effects of the results acquired in accordance with the used factors and their related levels on product strength [28]. In Table 6, the results of the ANOVA analysis are shown.

In ANOVA analysis, whether a parameter affects the response is determined by looking at the P (significance/probability) value. Considering the 95 % confidence interval, it concludes that the parameter affects the response when $P < 0.05$ (5 % significance value) [29]. Since the P value is above 0.05 in the ANOVA table (Table 6), the cooling time has no effect on the friction weld quality. In Table 8, the effects of each factor's percentage of contribution on total variation are shown at the rightmost. The most effective parameters for the strength of friction welding area rates are 42.74 % for rotation speed, 31.85 % for friction welding pressure and 23.12 % for friction welding duration has been observed. Also, the least effective parameter was determined as cooldown time with 2.28 % rate.

5.4 Forecast Calculation of the Best Choice

The strength gauge in the verification parts can in advance approximately calculated with mathematical in accordance with S/N ratio. Kahraman and Basar [30] found the optimum parameter for acquiring the lowest surface roughness on aluminium parts' boring process with the Taguchi experimental method. They have determined the value of surface roughness that can occur with optimum parameters by calculating with S/N rate. After, they observed that the two values are close, which are the calculated value and the value of surface roughness that occurs after the process with the optimum parameter value.

Table 6. *ANOVA analysis*

Source	DF	Seq SS	Adj SS	Adj MS	F	P	Content ratio [%]
Rotation speed [rpm] A	3	3.565	3.565	1.18849	147	0.001	42.74
Friction welding pressure [bar] B	3	2.657	2.657	0.85563	110	0.001	31.85
Friction welding duration [s] C	3	1.929	1.929	0.64292	79.5	0.002	23.12
Cooldown time [s] D	3	0.19	0.19	0.06345	7.85	0.062	2.28
Error	3	0.024	0.024	0.00808			
Total	15	8.366					100

The estimated strength amount formula is as below.

$$F_t = \left(\max S/N_1 - N_m\right) + \left(\max S/N_2 - N_m\right) + \left(\max S/N_3 - N_m\right) + \left(\max S/N_4 - N_m\right), \quad (2)$$

where F_t is the sum of the differences between the selected best-levelled value of S/N and N_m, arithmetic average of S/N values for the calculated strength.

$$N_{hd} = F_t + N_m, \quad (3)$$

where N_{hd} is the calculated S/N rate for the test.

$$R_{day.} = 10^{\frac{N_{hd}}{20}} \text{ [mm]}, \quad (4)$$

where $R_{day.}$ is the amount of maximum estimated strength.

It is envisioned that the estimated strength amount would be 30.014 bar when the estimating formula applies to joining strength analysis values of inline body and cover.

5.5 The Verification Test for Friction Welding Joining of the Inline Body and Cover Part

The optimum parameter values are determined with Taguchi experimental method. However, mass manufacturing should not be started in accordance with found optimum values. Before that, production should be produced in accordance with the determined optimum value and compared.

Taguchi's experimental method was applied to a DVD-ROM's front plastic cover to increase the bending strength and optimum values. They had 17.1 % increase in the bending strength with the study of the front cover part [31].

Friction welding has been made to the body and cover parts in accordance with related test factors and levels for the verification test; five friction welding processes have been made to the parts. The bending strength values have been determined by applying the static pressure test to joined parts with friction welding. The determined strength and average strength values are shown in Table 7.

Table 7. *The Table of average strength values for the verification part*

Test 1 [bar]	Test 2 [bar]	Test 3 [bar]	Test 4 [bar]	Test 5 [bar]	Average strength [bar]
28.53	29.51	29.89	28.17	29.74	29.168

The average strength value for the parts joined with the friction welding process in accordance with optimum parameters is determined as 29.168 bar. At the calculation, the strength value of the product emerged as 30.014 bar. The error rate between the validation test and the calculated value was 2.81 %. In Fig. 12, the pressure value of test 1, which was produced with verification parameters, is shown. The test has shown that the side wall of the 1 numbered part exploded with cracked at the maximum strength in Fig. 10. It is observed that the joint area with friction welding resisted the pressure. In the static pressure test, the wall thickness in the weld area is high, so the part bursts from the weak part.

Fig. 10. *The measurement of the verification part test 1*

In Table 8, the calculated and measured strength values are shown.

Table 8. *The compassion between the value of verification part and calculated value*

The chosen parameter	Estimated calculated value [bar]	The average value of verification part [bar]
A3 B3 C3 D4	30.014	29.168

$R_{day.}$ with the implemented Taguchi experimental method, the friction welding parameters have been optimized. The acquired optimum level values (A3 B3 C3 D4) for the friction welding verification part were determined as 41.5 rps for rotation speed, 6 bar for friction welding pressure, 2 seconds for friction duration and 4 seconds for cooldown time. The average strength value for the part was made in accordance with friction welding optimum weld parameters acquired as 29.168 bar. The strength of the verification part can be estimated and calculated with mathematical calculation in accordance with the S/N rate in advance. According to this calculation, the strength value of the part is calculated as 30.014 bar. It can be observed that the strength value calculated and acquired with optimum parameters values emerged close. The difference has been accepted due to the effect on the quality of welding would be very low.

5.6 The Testing of Dynamic Friction Welding on Inline Body and Cover's Part

The strength of the friction welding joint profile structure that we have developed is above the desired level at the static pressure tests. On the joining point, the strength of static pressure can be high, although the strength of dynamic pressure can be low. The dynamic pressure has been tested in accordance with International NSF/ANSI 58 standard. In this test, it is desired that the part can be able to maintain its function and there should be no deformation for 5 seconds (<10.4 bar) with pressure and during 5 seconds without pressure with 100,000 cycles [25]. The dynamic test experiment has been implemented to this part, which is joined with friction welding for this purpose. In Fig. 11, the implementation of a dynamic test to the part joined with friction welding is shown.

Fig. 11. *The dynamic test*

In Fig. 11, five friction welded products' statuses are shown while performing the dynamic test. Due to lack of pressure on the city water, by way of a pump, the pressure has been increased up to 10 bar. The maximum pressure on the system was measured at 11.61 bar. The dynamic test started with 8 hours per day and the test has been completed in approximately 35 days (7 weeks). At the end of the test, approximately 105,000 cycles were implemented; it was observed that there are no deformation on the part form and no water leakage.

Filter parts joined by the friction welding process have successfully passed the dynamic tests. By producing 1500 pilot products, friction welded filters can be used at the customer's house in different weather conditions and water network pressures. It is intended to test such water leakage, cracking in the weld area, deformity of the filters and whether the improvement is beneficial or not.

6 RESULT & DISCUSSION

In inline filters used from water purification devices, semi-melted accumulations occur in the inner and outer parts after friction welding. The semi-melted accumulations formed in the interior cause clogging, a decrease in flow rate and clogging after the narrowing of the surface area in the activated carbon felt. Schmicker et al. [9] performed friction welding simulations of metal parts by rotating them in the software program they developed. To prevent metal semi-melted accumulation in the interior, a joint profile design has been developed and simulations have been carried out. To prevent metal semi-melted accumulation in the interior, a joint design has been developed and simulations have been practiced.

A finite element analysis method (ABAQUS) of the weld joint profile design has been developed to solve this problem and confine the semi-melted agglomeration in the interior. In Fig. 12, the semi-melted conditions of the developed weld joint profile designs are shown as a result of the analysis. From these melt conditions, it was observed that the welding joint profile design N3 imprisoned the semi-melted agglomeration.

Schmicker et al. [9] imprisoned semi-melted agglomerations in their study. In the results of the analysis made on the developed weld joint profile design, semi-melted agglomeration is imprisoned. Friction welding is applied to the plastic parts printed after the modifications made in the injection moulds.

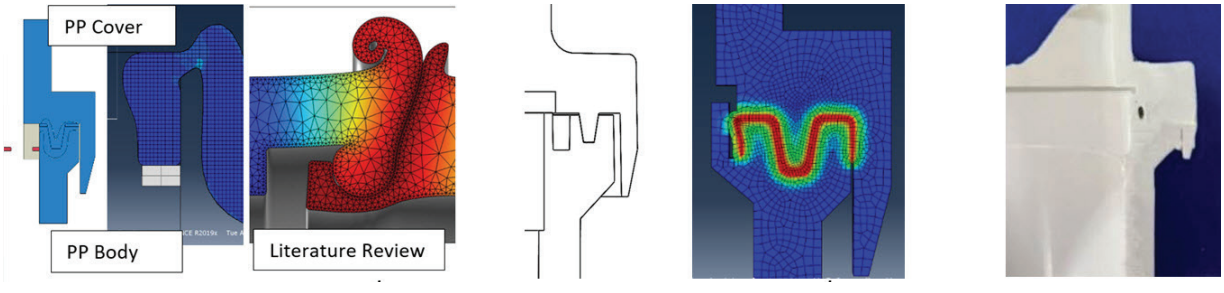

Fig. 12. *a) Existing semi-melted accumulation analysis [10], b) literature search [9], c) developed weld joint profile design no. 3, d) melt accumulation analysis no. 3 design, and e) semi-melted agglomeration situation after friction welding*

As a result of the analysis, a structure close to the semi-melted agglomeration was obtained and the semi-melted agglomeration was confined.

Filter parts joined by the FW process have successfully passed the static and dynamic tests according to NSF/ANSI 58, Chapter 5.1.3.2 standard [25]. By producing 1500 pilot products, friction welded filters can be used at the customer's house in different weather conditions and water network pressures. It is intended to test such water leakage, cracking in the weld area, deformity of the filters and whether the improvement is beneficial or not.

In the field test, 1500 already-existing manufactured products were sold, and 1500 new products produced with the design developed were followed up until the filter was changed after six months. Early replacement and defective filters were blocked from the filters in the following products. In Fig. 13, the semi-melted agglomeration status of the sediment filter is observed, and it is seen that there is no semi-melted agglomeration in the weld joint profile designed sediment filter and this result in reducing the failure rates.

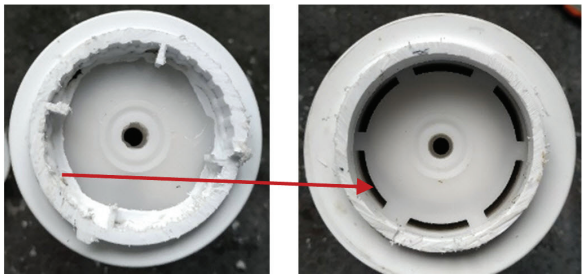

Fig. 13. *a) Current manufacturing sediment filter, and b) weld joint profile developed sediment filter*

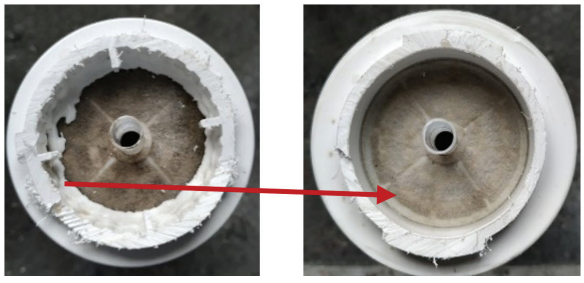

a) *b)*

Fig. 14. *a) Current manufacturing activated carbon filter, and b) weld joint profile developed activated carbon filter*

In Fig. 14, the semi-melted accumulation state of the activated carbon filter is observed, and it is seen that there is no semi-melted accumulation on the surface of the felt in the activated carbon filter with a weld joint profile design. It is seen that the developed weld joint profile design is beneficial for the activated carbon filter and reduces the failure rates.

In Fig. 15, enlarged pictures of the felt in the semi-melted agglomeration status of the activated carbon filter are shown. When the layered state of the felt is examined, particles larger than the pore diameter cause blockages. It prevents the passage of water.

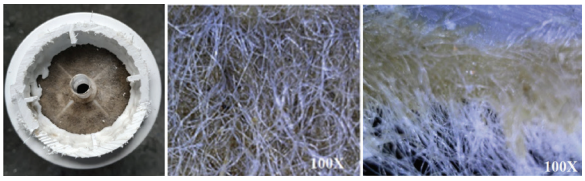

a) *b)* *c)*

Fig. 15. *a) Current manufacturing activated carbon filter, b) enlarged view of felt, and c) enlarged side section view of the felt*

In Fig. 16, enlarged pictures of the felt in the weld joint profile developed activated carbon filter are shown. When the layered state of the felt is examined, there are few blockages in the pores. However, these blockages do not prevent the passage of water.

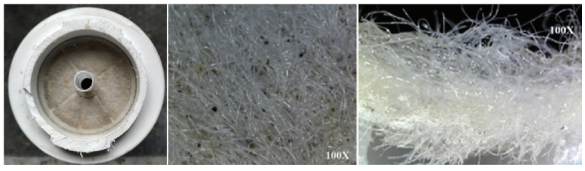

a) *b)* *c)*

Fig. 16. *a) Weld joint profile developed activated carbon filter, b) enlarged view of felt c) enlarged side section view of the felt*

When the products from the field are examined, two sediment filters and one activated carbon filter are used in each product. For this reason, 3000 sediment filters and 1500 activated carbons were followed in 1500 products.

As can be seen in Table 9, the improvement in the friction weld joint profile structure reduced the error rates caused by semi-melted accumulation to zero. It has been determined that the filter changes do not decrease much depending on the quality of the water from the network.

7 CONCLUSIONS

In this study, moulds have been produced and product presses have been taken out according to the developed friction welding joint profile design. The values below have been acquired by implementing the

Table 9. *Field test results of the filters produced*

	Sediment filter - 3000 pieces						Activated carbon filter (GAC) - 1500 pieces			
	Semi-melted stacking clogging		Low flow as a result of semi-melted accumulation		Early filter change		Premature clogging of felt due to semi-melted stacking		Early filter change	
	Error amount	Error rate [%]	Error amount	Error rate [%])	Error amount	Error rate [%]	Error amount	Error rate [%]	Error amount	Error rate [%]
Developed weld joint profile design manufacturing	0	0.00	0	0.00	15	0.50	0	0.00	28	1.87
Current manufacturing	92	3.07	104	3.47	63	2.10	187	12.47	42	2.80

Taguchi experimental method and ANOVA analysis of friction welding machine parameters.

- The welding parameters for the friction welding area should be A3 B3 C3 D4 (rotation speed 2490 rpm, friction welding pressure 6 bar, friction welding duration 2 seconds, cooldown time 4 seconds) for the maximum strength;
- The rotation speed parament has a 42.74 % rate effect on weld quality;
- The friction welding pressure parameter has a 31.85 % rate effect on weld quality;
- The cooldown time parament has no effect on welding quality;
- The parts produced according to acquired optimum parameters' static and dynamic tests have been made in accordance with NSF standards, and no negative aspects have been observed
- At the implemented static pressure test, the average strength value is 29.168 bar, at the dynamic pressure test 5 seconds without pressure and 5 seconds with pressure at 11.6 bar there are 105,000 on/off (min 100,000 on/off). No negativity has been observed.

A field test was conducted to see whether the developed weld joint profile design is significantly improved. As field test results:

- It has been determined that the filter change rates caused by the semi-melted accumulation in the interior of the sediment filters are reduced to zero;
- It has been determined that the filter change rates caused by semi-melted accumulation in the inner part of the activated carbon filters are reduced to zero;
- it is now possible to manufacture inline membrane filters since there is no semi-melted accumulation in the interior.

REFERENCES

[1] Parast, M.S.A., Bagheri, A., Kami, A., Azadi, M., Asghari, V. (2022) Bending fatigue behavior of fused filament fabrication 3D-printed ABS and PLA joints with rotary friction welding. *Progress in Additive Manufacturing*, **DOI:10.1007/s40964-022-00307-5**.

[2] Halbin, G., Gulfeng, X., Jingcheng, L. Hao, L. (2022). Rotary friction welding of püre aluminum to preheated brass. *Welding in the World*, vol. 66, p. 2371-2376, **DOI:10.1007/s40194-022-01367-5**.

[3] Bindal, T., Saxena, R.K., Pandey, S. (2020). Analysis of joint overlap during friction spin welding of plastics. *Materials Today: Proceedings*, vol. 26, p. 2798-2804, **DOI:10.1016/j.matpr.2020.02.581**.

[4] Sahu, S.K., Mishra, D., Mahto, R.P., Sharma, V.M., Pal, S.K., Pal, K., Banerjee, S., Dash, P. (2018). Friction stir welding of polypropylene sheet. *Engineering Science and Technology, an International Journal*, vol. 21, no. 2, p. 245-254, **DOI:10.1016/j.jestch.2018.03.002**.

[5] Hamade, R.F., Andari, T.R., Ammouri, A.H. Jawahir, I.S. (2019). Rotary friction welding versus fusion butt welding of plastic pipes - feasibility and energy perspective. *Procedia Manufacturing*, vol. 33, p. 693-700, **DOI:10.1016/j.promfg.2019.04.087**.

[6] Kasman, Ş., Kahraman,. F., Aydın, A. (2016). investigation of the effect of different stirrer pin geometries on welding performance of aa7075-t651 aluminum alloys joined by friction stir welding method. *International Symposium on Innovative Technologies in Engineering and Science*, p. 1393-1402.

[7] Saju, T., Velu, M. (2022). Characterization of welded joints of dissimilar nickel-based superalloys by electron beam and rotary friction welding. *Journal of Materials Engineering and Performance*, **DOI:10.1007/s11665-022-06958-3**.

[8] Taysom, B.S., Sorensen, C.D. (2020). Controlling martensite and pearlite formation with cooling rate and temperature control in rotary friction welding. *International Journal of Machine Tools & Manufacture*, vol. 150, art. ID 103512, **DOI:10.1016/j.ijmachtools.2019.103512**.

[9] Schmicker, D. Persson, P.O., Strackelijan, J. (2014). Implicit geometry meshing for the simulation of rotary friction welding.

Journal of Computational Physics, vol. 270, p. 478-489, **DOI:10.1016/j.jcp.2014.04.014**.

[10] Maden, H. and Çetinkaya, K. (2021). Joining analysis of polypropylene parts in rotary friction welding process and developing of joints profile. *Journal of Polytechnic*, vol. 24, no. 3, p. 1263-1273, **DOI:10.2339/politeknik.824615**.

[11] Maden, H., Çetinkaya, K. (2020). Making moldflow analysis to produce different geometry parts in the same mold. *2nd International Scientific-Practical Conference: Modern Information. Measurement and Control Systems: Problems and Perspectives*.

[12] DIN 16901 (1982). *Plastics Mouldings. Tolerances and acceptance conditions for linear dimensions*. from: https://www.apt-mold.com/wp-content/uploads/2018/02/DIN-16901.pdf, accessed on: 2022-06-25, Deutsches Institut für Normung, Berlin.

[13] Taguchi, G. (1990). *Taguchi. Introduction to Quality Engineering*. Asian Productivity Organization. Tokyo.

[14] Van, A.-L., Nguyen, T.-T. (2022). Optimization of friction stir welding operation using optimal taguchi-based ANFIS and genetic algorithm. *Strojniški vestnik - Journal of Mechanical Engineering*, vol. 68, no. 6, p. 424-438, **DOI:10.5545/sv-jme.2022.111**.

[15] Singh, R., Kumar, R., Feo, L., Fraternali, F. (2016). Friction welding of dissimilar plastic/polymer materials with metal powder reinforcement for engineering applications. *Composites Part B: Engineering*, vol. 101, p. 77-89, **DOI:10.1016/j.compositesb.2016.06.082**.

[16] Ozcelik, B. (2011). Optimization of injection parameters for mechanical properties of specimens with weld line of polypropylene using taguchi method. *International Communications in Heat and Mass Transfer*, vol. 38, no. 8, p. 1067-1072, **DOI:10.1016/j.icheatmasstransfer.2011.04.025**.

[17] Park, C.H., Pyo, B.G., Choi, D.H., Koo, M.S. (2011). Design optimization of an automotive injection molded part for minimizing injection pressure and preventing weldlines. *Transaction Korean Soc Automotive Engineers*, vol. 19, no. 1, p. 66-72.

[18] Altınsoy, A., Arslan, Y. (2021). Optimization of polyoxymethylene copolymer workability on water-jet machines using taguchi method. *International Journal őf Eastern Anatolia Science Engineering and Design*, vol. 3, no. 1, p. 333-349.

[19] Minitab 15. (2014). *User Manual Making Data Analysis Easier*. Minitab Inc. State College, San Francisco.

[20] Phadke, M.S. (1989). Quality engineering using robust design. In Dehnad, K. (ed.) *Quality Control, Robust Design, and the Taguchi Method*. Springer, Boston, **DOI:10.1007/978-1-4684-1472-1_3**.

[21] Yuin, W., Alan, W. (2000). *Taguchi Methods for Robust Design*. ASME Press, New York.

[22] Fowlkes, W.Y., Creveling, C.M. (1995). *Engineering Methods for Robust Product Design: Using Taguchi Methods in Technology and Product Development*. Addison-Wesley Publishing Company, Boston, Massachusetts.

[23] Schmidt, S.R., Creveling, C.M. (1997). *Understanding Industrial Designed Experiments*. Air Academy Press. Colorado.

[24] Peace, G.S. (1992). *Taguchi Method: A Hands-On Approach*. Addison Wesley Publishing, Boston .

[25] NSF/ANSI (2013). *Chapter 5.1.3.2, Hydrostatic pressure test - complete systems, NSF/ANSI 58 - 2013 Reverse Osmosis Drinking Water Treatment Systems*, p. 28; Michigan.

[26] Park, S.H. (1996). *Robust Design and Analysis for Quality Engineering*. Chapman and Hall. London.

[27] Ross, P.J. (1996). *Taguchi Techniques for Quality Engineering*. Mc Graw-Hill, New York.

[28] Bilici, M.K., Bakır, B., Bozkurt, Y., Çalış, İ. (2016). Taguchi analysis of dissimilar aluminum sheets joined by friction stir spot welding. *Pamukkale University Journal of Engineering Sciences*, vol. 22, no. 1, p. 17-23, **DOI:10.5505/pajes.2015.06641**.

[29] Savaşkan. M., Taptık, Y., Ürgen, M. (2004). Performance optimization of drill bits by experimental design method. *Istanbul Technical University Journal*, vol. 3, no. 6, p. 117-128.

[30] Kahraman, F., Basar, G. (2018). The application of taguchi method in drilling process for optimization of multi response problem. *International Journal of Scientific and Technological Research*, vol. 4, no. 10, p. 1-9.

[31] Öktem, H., Kır, D., Sarı, E.S., Çöl, M. (2018). Determination of the most appropriate injection process parameters affecting the mechanical properties of plastic products by Taguchi method. *Journal of Machine Design and Manufacturing*, vol. 14, no. 1, p. 8-16.

Strojniški vestnik - Journal of Mechanical Engineering 68(2022)11, 669-682
DOI:10.5545/sv-jme.2022.219
Original Scientific Paper
Received for review: 2022-06-02
Received revised form: 2022-08-09
Accepted for publication: 2022-10-13

Rigid-elastic Coupling Dynamic Model and Dynamic Characteristics of a Spring-type of Traction Robot

Jianguo Zhao[1,2,3,*] – Binfan Wang[1,3] – Qingyou Liu[1,3] – Guorong Wang[1,3] – Xiangfeng Zeng[4]

[1]Southwest Petroleum University, School of Mechantronic Engineering, China
[2]Sichuan Provincial Key Lab of Process Equipment and Control, China
[3]Southwest Petroleum University, Energy Equipment Institute, China
[4]Yunnan Shuifu Yuntianhua Co., China

The traditional anchoring mechanism of the traction robot is rigid and is easily stuck in the wellbore. To solve this problem, a novel anchoring mechanism is proposed based on the spring-type of anchoring mechanism of the inclined block. The key to the movement of the traction robot is whether the traction robot can be anchored in the wellbore under the action of the traction force. Therefore, a rigid-elastic coupling dynamic model of the spring-type of anchoring mechanism under the action of the traction force was established. On this basis, the effects of span, width, thickness, and chamfer parameters on the anchoring performance of the spring-type of traction robot were analysed to design the optimal structure of the anchoring arm. Through the experimental comparison, it was determined that the error between the theoretical supporting force and the experimental supporting force was only 6.1 %, and the error of the simulated maximum traction force and experimental maximum traction force was 4.9 %. The traction robot can provide a maximum traction force of 14262 N in 178 mm (7-inch) of wellbore pipe. Thus, experiments verified the correctness of the rigid-elastic coupling dynamic model. The research results of this paper lay a foundation for the structural design and engineering application of a spring-type of traction robot. It can effectively ensure the downhole safety of oil and gas wells.

Keywords: spring-type of traction robot, spring-type of rigid-elastic coupling dynamic model, spring-type of anchoring mechanism, motion anchoring

Highlights

- *A novel spring-type of anchoring mechanism of traction robot based on inclined blocks is proposed, which provides a large traction force for the robot and can avoid being stuck.*
- *The rigid-elastic coupling dynamic model of the spring-type of anchoring mechanism is established.*
- *The calculation method of boundary conditions of self-anchoring of the traction robot (safe or not) is created.*
- *The maximum traction forces under different structural parameters have been obtained, and the correctness of the theoretical maximum traction force has been verified by experiments.*

0 INTRODUCTION

Horizontal well exploitation has become an important way to increase the recovery of oil and gas fields. It is mainly applied to the exploration and development of deep-sea and complex petroleum resources. It is increasingly difficult to deliver drilling tools as the depth of horizontal wells and the length of horizontal sections continue to increase. Compared with several methods, such as coiled tubing conveyance **[1]** and **[2]**, drill pipe conveyance, and pump-in conveyance, the conveying method of downhole traction robots **[3]** to **[5]** can deliver instruments quickly and accurately, as well as significantly save time and reduce costs **[6]**.

According to the movement mode, downhole traction robots can be divided into wheeled-type **[7]** to **[10]**, telescopic-type **[11]** and **[12]**, crawler-type **[13]** and **[14]**, etc. Among them, wheeled and telescopic types are the most widely used in engineering. The conventional wheel-type traction robot has a group of expandable and collapsible anchoring arms, which hold the driving wheels against the wellbore wall. The rotating driving wheels drive the wheel-type traction robot to move in the horizontal well by the friction force between the driving wheel and the wellbore. The conventional telescopic traction robot is anchored in the wellbore wall by two or more sets of anchoring arms that can be opened and closed alternately. One group of anchoring arms is held stationary on the wellbore wall. At this point, another set of cylinders or motors slides towards or behind each other to achieve directional movement of the robot in the wellbore. For telescopic traction robot, rigid anchoring arms are mostly adopted between the anchoring mechanism and the wellbore wall to anchor the wellbore wall to perform traction action. The rigid anchoring arm has more constraints, which leads to fewer degrees of freedom in the mechanism, so it easily becomes stuck during the working process.

In addition, the anchoring mechanism of telescopic traction robot can adopt an elastic anchoring method. However, most of the elastic

*Corr. Author's Address: School of Mechantronic Engineering, Chengdu 610500, China, zhaojianguo_1@qq.com

anchoring mechanisms designed by Gao et al. [15] and Liu et al. [16] and [17] are connected with rods and pins, at which points the forces on them are mainly concentrated. The position of the connecting rod and pin cannot achieve the strength requirements, so that the mechanism is deformed. Moreover, the schemes of the elastic anchoring methods only considered the motion characteristics under the rigid conditions but did not optimize its anchoring structures or determine its maximum traction force.

Therefore, based on previous studies, a novel telescopic downhole traction robot based on the spring-type of anchoring mechanism of the inclined block [18] is proposed in this paper. The traction robot has the characteristics of large traction force and automatic un-anchoring, which can to some extent prevent the occurrence of being stuck. This paper focuses on analysing the influencing factors of the spring-type of anchoring mechanism and optimizing its structures. The maximum traction force of the spring-type of anchoring mechanism under different wellbores is determined.

1 WORKING MECHANISM

On the basis of analysing and determining the strengths and weaknesses of existing traction robots, this paper proposes a spring-type of hydraulic telescopic downhole traction robot. It adopts a leaf spring with elastic restoring force as the anchoring arm, which can provide greater traction force while better adapting to the wellbore wall. This traction robot is lowered into the horizontal section through coiled tubing. The primary function of the robot is to deliver downhole pipe strings in horizontal wells or large displacement wells for other operations, such as logging and well workovers. The traction robot connects coiled tubing at the end and the downhole tools at the front, and its power and signals are transmitted through the cables and signal lines inside the coiled tubing. The application form of the robot is shown in Fig. 1.

It can be seen from Fig. 1 that the spring-type of telescopic downhole traction robot includes a front working section, a rear working section, and a control section. The front working section includes a front anchoring mechanism and a front telescopic mechanism, and the rear working section includes a rear anchoring mechanism and a rear telescopic mechanism. The executive parts of the working mechanism include four double-acting hydraulic cylinders (front support cylinder, front telescopic cylinder, rear support cylinder, rear telescopic cylinder). The action mechanism will be described below in conjunction with the action sequence in Fig. 2.

(1) From the initial status to status A: The hydraulic oil is injected into the front support cylinder, and the push rod of the front support cylinder is pushed to move to the right. The anchoring arms extend to anchor the wellbore wall.

(2) From status A to status B: The front and rear telescopic cylinders are simultaneously injected with hydraulic oil. The control section and rear working section simultaneously walk forward a telescopic cylinder stroke *S*. At this point, the traction robot has completed the first forward motion.

(3) From status B to status C: The rear support cylinder is injected with hydraulic oil and pushes the rear support cylinder push rod to move to the

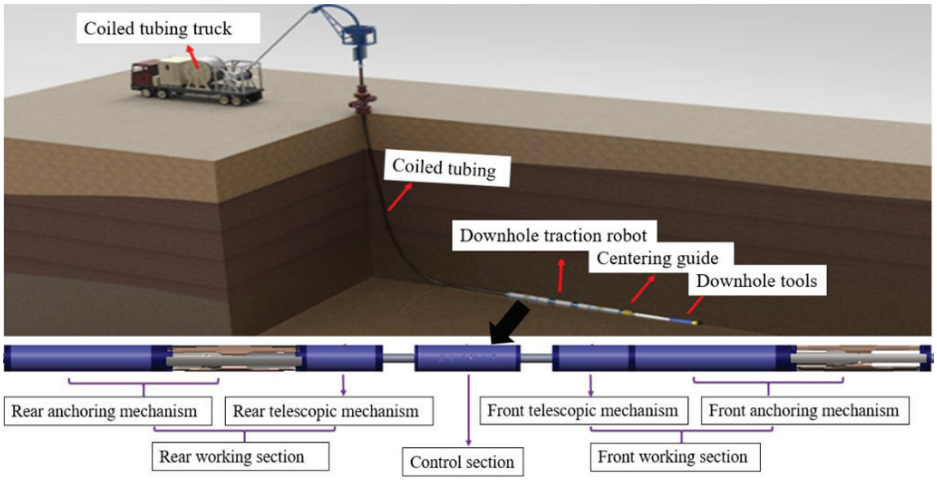

Fig. 1. *Application form of spring-type of hydraulic telescopic downhole traction robot*

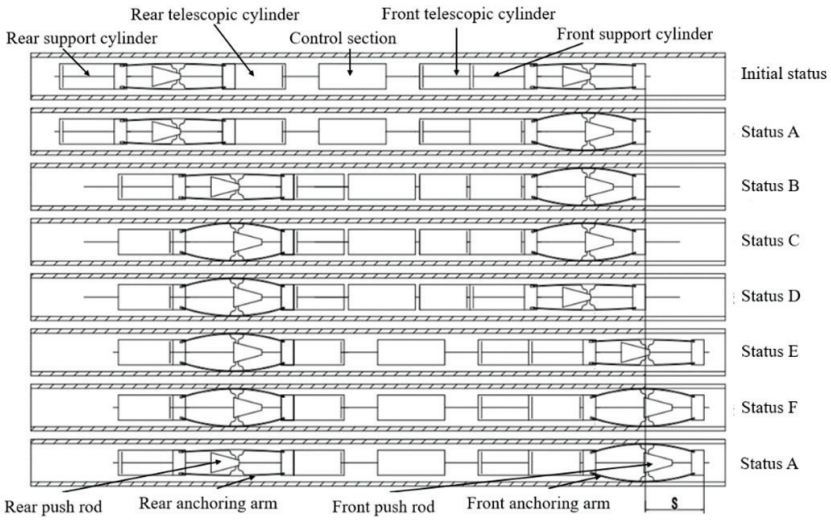

Fig. 2. *Schematic diagram of the working mechanism of the downhole traction robot*

right. Under the action of the rear push rod joint, the rear anchoring arms extend to anchor the wellbore wall to prepare for the alternate work of the front and rear working sections.

(4) From status C to status D: The front support cylinder is injected with hydraulic oil. At this time, the front anchor arms are restored to their initial state to prepare for the movement of the rear telescopic cylinder.

(5) From status D to status E: Hydraulic oil is injected simultaneously into the rear telescopic cylinder and the front telescopic cylinder. The control section and the front working section are simultaneously crawling forward for one telescopic cylinder stroke *S*. At this time, the traction robot completes the first stretch.

As shown in Fig. 2, it is a complete motion cycle of the traction robot from the initial status to status *F*. The front and rear working section are operated alternately to achieve forward telescopic crawling.

2 DYNAMIC CHARACTERISTICS

The mechanical model of the spring-type of anchoring mechanism is shown in Fig. 3 during the traction process. In this chapter, the relationship between the supporting force F_S of the supporting cylinder, the traction force F_T and the elastic restoring force F_2 can be obtained through the analysis of the mechanical model. The elastic restoring force and the maximum stress of the spring-type of anchoring arm with different structural sizes can be obtained using ABAQUS simulation analysis [19]. The

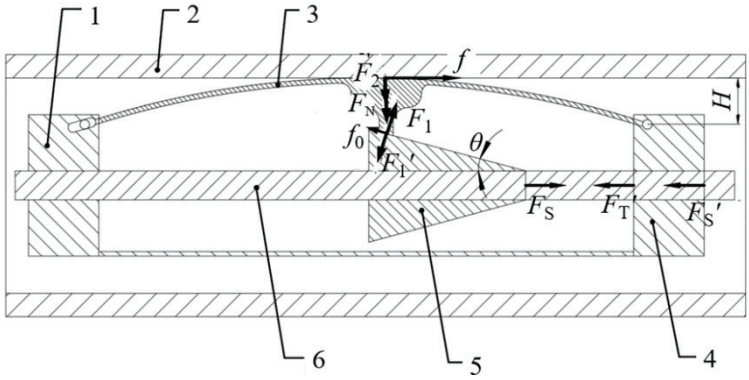

Fig. 3. *Schematic diagram of stress analysis of spring-type of anchoring mechanism; 1 left support frame, 2 wellbore pipe, 3 spring-type of anchoring arm, 4 right support frame, 5 push rod joint, and 6 central axis*

optimal structure of the spring-type of anchoring arm that meets the safe mechanical conditions and can overcome the friction force of the hydraulic cylinder seal ring to achieve automatic recovery will be determined under no-load conditions. Finally, the values of F_S and F_2 of the spring-type of anchoring arm with the optimal structural size in different sizes of the wellbore are obtained.

2.1 Mechanical Characteristics of Traction Process of Spring-Type of Anchoring Mechanism

After the spring-type of anchoring mechanism of the traction robot anchors the wellbore wall, the telescopic mechanism of the traction robot starts to drag the downhole tool to move forward. At this point, the friction between three spring-types of anchoring arms and the wellbore wall will overcome the load traction force of the downhole tools to achieve forward motion.

It can be seen from Fig. 3 that the push rod joint is subjected to the supporting force F_S and the reaction force of supporting force F_1' in the process of rightward movement. A spring-type of anchoring arm is subjected to the supporting force F_1, the wellbore wall supporting force F_N, its elastic restoring force F_2, and the whole anchoring mechanism is subjected to the friction force *f*. At the same time, the left support frame of the spring-type of anchoring arm is solidly connected to the right support frame. In the process of moving the push rod joint to the right, the right support frame will generate the reaction force F_S', which is equal to the supporting force F_S and opposite to the direction, and the load reaction force F_T' which makes the downhole tools achieve forward motion.

Take a single spring-type of anchoring arm as the research object. F_1 is the supporting force generated by the push rod joint. F_N is the supporting force generated by the wellbore wall. F_S' is the reaction force of the supporting force. F_T' is the reaction force of the traction force. *f* is the friction force generated by the wellbore wall to the whole anchoring mechanism. Three spring-types of anchoring arms are uniformly distributed along the central axis in space, so that the resultant force of three frictional forces between three spring-types of anchoring arms and push rod joint is 0 *N* in the radial direction. The gap between three spring-types of anchoring arms and push rod joint is matched, and there is a lubrication device, so the friction between them can be ignored. Through ABAQUS simulated analysis, θ is selected as 13.6° according to the design structure. *H* is the radial displacement of the spring-type of anchoring arm, which is determined by the different inner diameters of the wellbore. According to the mechanical equilibrium relationship, there is the following relationship equation.

According to $\Sigma X=0$, the following equation can be obtained:

$$F_1 \sin\theta + \frac{f}{3} = \frac{F_s^{'}}{3} + \frac{F_T^{'}}{3}. \tag{1}$$

According to $\Sigma Y=0$, the following equation can be obtained:

$$F_1 \cos\theta = F_2 + F_N. \tag{2}$$

In addition, it is assumed that the friction coefficient between the wellbore wall and spring-type of anchoring arm is μ, which is taken a value as 0.25 (the value of μ is 0.2 to 0.3, and the intermediate value of 0.25 is taken for theoretical research). Then there is the relationship equation:

$$\frac{f}{3} = \mu F_N. \tag{3}$$

Substituting Eqs. (2) and (3) into Eq. (1) yields:

$$\left(\frac{f}{3\mu} + F_2\right)\tan\theta + \frac{f}{3} = \frac{F_s^{'}}{3} + \frac{F_T^{'}}{3}. \tag{4}$$

For the traction robot to crawl forward, the friction force *f* must be greater than or equal to the traction force F_T' on the traction robot, namely:

$$f \geq F_T^{'}. \tag{5}$$

If the friction force is equal to the traction force of the traction robot, the relationship between the supporting force F_S of the support cylinder and the reaction force F_T' of the traction force can be derived by bringing Eq. (5) into Eq. (4):

$$F_S^{'} = \frac{F_T^{'}}{\mu}\tan\theta + 3F_2\tan\theta. \tag{6}$$

In Eq. (6), the reaction force F_T' of traction force is determined by the load. From Eq. (6), the supporting force F_S can be obtained to overcome different load traction forces in wellbores with different inner diameters.

2.2 Optimization Research of Structure Parameters of Spring-type of Traction Robot

The spring-type of anchoring arm of the traction robot is designed with the purpose of the leaf spring. When the traction robot has unexpected conditions in the well (such as power failure, solenoid valve out of control), the leaf spring can use its elastic restoring

force to overcome the friction generated by the seal in the support cylinder to avoid being stuck. The traction robot has two support cylinders, and the O-ring is a seal inside the support cylinder. Therefore, it is necessary to calculate the size of the friction resistance generated by the O-ring [20] in the support cylinder. Xu [21], Xiao [22], and Zuo and Zhang [23] studied the friction force generated by the O-ring in the hydraulic cylinder. From the design dimensions and relevant parameters of the traction robot, the frictional resistance of the sealing ring that needs to be overcome is 647 N when the piston is automatically reset by the restoring force of the leaf spring. Therefore, the leaf spring must fulfil this restoring force to achieve the function of automatic un-anchoring of the spring-type of anchoring mechanism.

From Eq. (6), it can be known that the main factor affecting the supporting force under the same wellbore and the traction force is the elastic restoring force of the spring-type of anchoring arm. Therefore, ABAQUS is used to simulate the span, thickness, width, and chamfer that affect the elastic restoring force of the spring leaf. The spring-type of anchoring arms are deformed under force, and its different radial displacements generate the corresponding elastic restoring forces. The design diameter of the traction robot is 118 mm, and it is suitable for a maximum pipe diameter of 178 mm (inner diameter (ID) 166 mm) wellbore. Therefore, for a 178 mm wellbore, the radial displacement H of the spring-type of anchoring arm is 24 mm, as shown in Fig. 3. Consequently, it is necessary to obtain the elastic restoring force with radial displacement of 24 mm.

According to the outside diameter of the traction robot and the design installation requirements, each parameter of the spring-type of anchoring arm is shown in Fig. 4, and the values are taken as illustrated in Table 1.

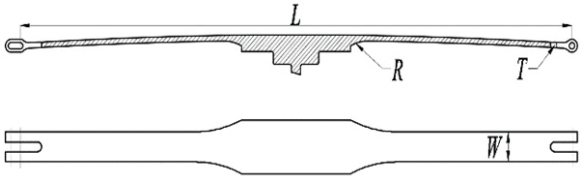

Fig. 4. *Schematic diagram of the spring-type of anchoring arm*

Under the same width, thickness, and chamfering radius of the spring, the changes of the elastic restoring force and the maximum stress of the spring with different spans are shown in Fig. 5.

Table 1. *The value of each parameter of anchoring arm*

Designation	Value [mm]				
Span (L)	412	462	512	562	612
Width (W)	25	30	35	40	45
Thickness (T)	4	4.5	5	5.5	6
Chamfering radius (R)	20	40	60	80	100

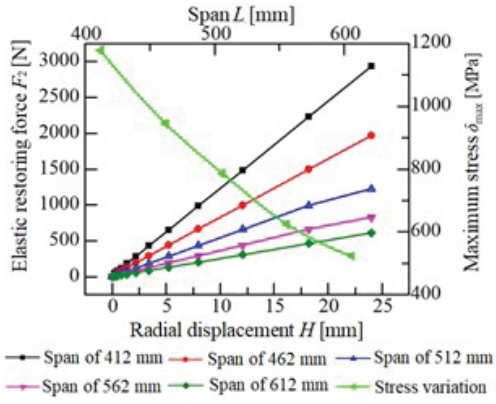

Fig. 5. *Change of elastic force and stress with span*

It can be seen from Fig. 5 that the larger the span of the leaf spring had, the smaller the maximum stress and the elastic restoring force would become. When the radial displacement of the leaf spring was 24 mm, the elastic restoring force of the leaf spring with a span of 412 mm was the largest (2,907 N). However, its maximum stress had exceeded the yield limit of the material (the material of 60Si2Mn, the yield strength of 1,176 MPa), resulting in plastic deformation. The leaf spring with a span of 612 mm had the smallest elastic restoring force (611 N), but the leaf spring could not overcome the frictional resistance of the O-ring. Therefore, the elastic restoring force of 462 mm, which was larger and much lower than the yield strength of the material, was the optimal value of the leaf spring span.

In the case of a spring span of 462 mm with the same width and thickness, the changes in the elastic restoring force and the maximum stress of the spring with different chamfer radii are shown in Fig. 6.

It can be seen from Fig. 6 that the maximum stress was larger and should not be selected when the chamfering radius is 20 mm and 100 mm. The elastic restoring forces of the spring of the rest of the chamfer radii were similar, but the chamfer radius of 40 mm was the smallest maximum stress. Considering the yield limit and the elastic restoring force, the chamfering radius of 40mm was the optimal value of the chamfering radius of the leaf spring.

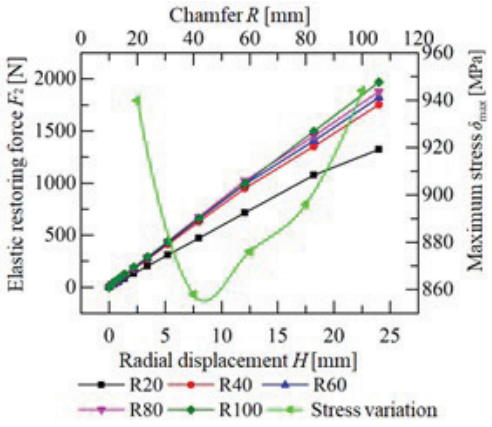

Fig. 6. *Change of elastic force and stress with chamfer*

In the case of a spring span of 462 mm, chamfer radius of 40 mm, and the same width, the changes in the elastic restoring force and the maximum stress of the spring with different thicknesses are shown in Fig. 7.

Similarly, the elastic restoring force and the maximum stress were positively correlated with the thickness by the analysis in Fig. 7. If the leaf spring was too thin, its stress met the material requirements, but its elastic restoring force did not satisfy the requirements. If the leaf spring was too thick, its elastic restoring force met the requirements, but its stress was extremely close to the yield limit of the material and did not meet the material requirements. Under the condition that other parameters remained unchanged if the thickness of the spring was selected as 5 mm, the maximum elastic restoring force was 1,753 N, and the maximum stress was 858 MPa. Both the restoring force and stress were suitable, so the thickness of 5mm was the optimal value in the spring leaf.

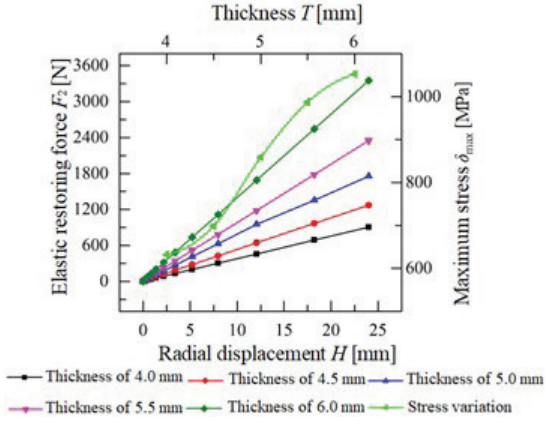

Fig. 7. *Change of elastic force and stress with thickness*

The variation curves of elastic restoring force and maximum stress for different widths of the leaf spring at a span of 462 mm, a chamfer radius of 40 mm, and a thickness of 5 mm are shown in Fig. 8.

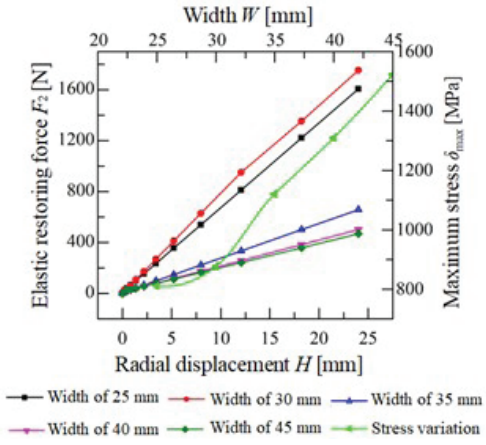

Fig. 8. *Change of elastic force and stress with width*

According to the analysis in Fig. 8, with the increase of the width of the spring, the elastic restoring force of the spring increased first and then decreased, and the maximum stress of the spring increased gradually. When the width of the leaf spring was 30 mm, the maximum elastic restoring force of the leaf spring was 1,753 N, and the maximum stress was 853 MPa. When the spring width was 45 mm, the maximum elastic restoring force of the spring was at least 451 N, and the maximum stress was 1,523 MPa. Obviously, the reason for the first increase in the elastic restoring force of the leaf spring was that its maximum stress was within the yield limit of the material. In addition, the reason for the sudden sharp decrease was that its maximum stress had exceeded the yield limit of the material, resulting in the plastic deformation. At a width of 35 mm, the analysis of the maximum stress diagram illustrated that the leaf spring had undergone plastic deformation in the weaker place, where is the chamfer of the spring of anchoring arm. Therefore, when the width of the spring piece was 30 mm, the stress was smaller and the elastic restoring force was appropriate. The width of 30 mm was the optimal value of the leaf spring width.

After the optimization of the structure parameters of the leaf spring, the final structure of the spring-type of anchoring arm was chosen to have a span of 462 mm, a chamfer radius of 40 mm, a width of 30 mm and a thickness of 5 mm. Through the data analysis of ABAQUS simulation, the relationship between the

restoring force F_2 and the radial displacement H of the spring arm can be obtained. The relationship is shown in Eq. (7):

$$F_2 = 14.7 + 73.7H. \tag{7}$$

Bring Eq. (7) into Eq. (6) to obtain the final expression of the supporting force required by the traction robot:

$$F_s = 3 \times \left(14.7 + 7H\right) \tan\theta + \frac{F_T^{'}}{\mu} \tan\theta. \tag{8}$$

Taking the radial displacement H (0 mm to 24 mm) as the independent variable and the supporting cylinder supporting force F_S as the dependent variable, the curve of the supporting force of supporting cylinder with the radial displacement of the leaf spring was obtained by fitting Eq. (8), as shown in Fig. 9.

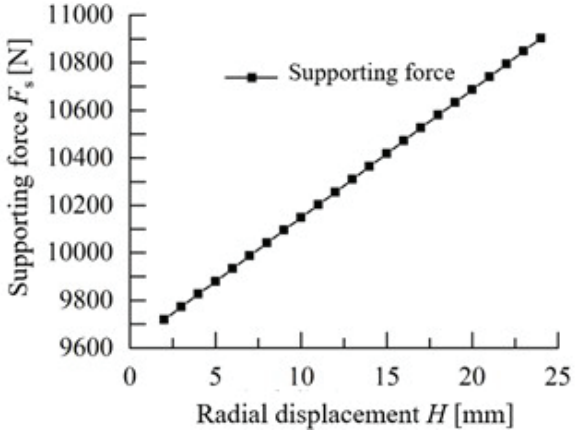

Fig. 9. *Curve of supporting force with radial displacement*

Table 2. *Supporting force of different wellbore*

Wellbore size [mm]	H [mm]	F_2 [N]	F_S [N]
178 (7-inch)	24	1,784	10,901
165 (6.5-inch)	15	1,120	10,417
152 (6-inch)	11	825	10,203

From Fig. 9, the magnitude of the required supporting force was obtained for different wellbore pipes with a design traction force of 10,000 N. From Eq. (7), it can be obtained that the radial displacement of the leaf spring needs to be greater than 8.6 mm to overcome the frictional resistance of the O-ring of 647 N and to have the ability to automatically unlock. Therefore, only the movement of the spring-type of traction robot in 152 mm (140 mm ID), 165 mm (148 mm ID) and 178 mm (161 mm ID) wellbore pipe was studied. From Eq. (7) and Fig. 9, the elastic restoring force and the required supporting force of the spring-type of anchoring arm can be obtained when different wellbores move, as shown in Table 2.

3 MODELING AND SIMULATION ANALYSIS

In this chapter, using ABAQUS and ADAMS [24] for co-simulation, a rigid-elastic coupled dynamic model was established and compared with the rigid model to verify the superiority of the rigid-elastic coupled dynamic model. Whether the spring-type of anchoring mechanism satisfied the anchoring performance under its design traction force was further verified. Finally, the maximum traction force of the spring-type of anchoring mechanism under different wellbores was determined.

3.1 Rigid-elastic Coupling Model of a Spring-type of Anchoring Mechanism

ABAQUS was carried out to establish a elastic model of the spring-type of anchoring arm. The procedure was as follows:

The spring-type of anchoring arm of the final structure determined in Chapter 2 is used to establish a three-dimensional model. The three-dimensional model was imported into the ABAQUS software. The material properties were defined in the software (the elastic modulus was 2.06×10^5 MPa, the Poisson's ratio was 0.29, and the mass density was 7.85×10^6 kg/mm^3). Two connection points of the spring leaf were defined as hard points, constraints were added, modal analysis was carried out to determine the form of the model, and a modal neutral file can be obtained. Finally, the modal neutral file was exported as an mnf file.

After the simulation model of spring-type of anchoring mechanism was built in the SolidWorks software, it would be imported into the ADAMS software. The three components of the left joint of the leaf spring, the right joint of the leaf spring and the fixed connecting rod, which were in a fixed relationship, were integrated into one component through a Boolean operation. Then they were called a "fixed connection body". At this point, the leaf spring is still a non-deformable rigid spring, and the model is rigid. Then, the modal neutral file of mnf of the spring was imported into ADAMS to replace the rigid spring. A rigid-elastic coupled dynamics model was generated, as shown in Fig. 10. The rigid model can be compared with the rigid-elastic coupled model for simulation.

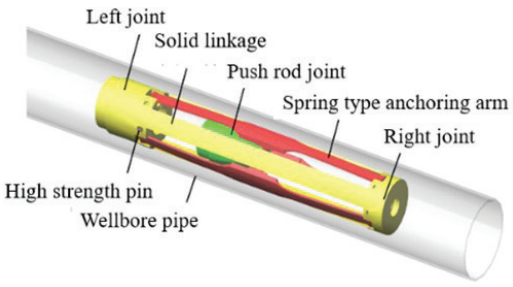

Fig. 10. *Rigid-elastic coupled dynamics model*

To perform dynamic analysis on the rigid-elastic coupled model, it is necessary to define the way of movement between the two contact mechanisms of the model, so that the model has a unique kinematic regularity. The wellbore is defined as a fixed frame, namely a fixed pair. The motion mode between the spring and the left and right support frames is defined as the rotational pair, with a total of six rotational pairs. The motion mode between the spring and the push rod joint is defined as the moving pair, and the motion mode between the central axis and the left and right support frames is defined as the moving pair, with a total of five moving pair.

From the dynamic analysis, it can be known that traction robot was mainly affected by the supporting force F_S and its reaction force F_S', the traction force F_T, the restoring force F_2 of the leaf spring and the friction force f in the traction process. From Table 2, when the traction robot drags the load forward in the 178 mm wellbore, the push rod joint was subjected to a supporting force of 10,901 N, and the fixed body was subjected to a reaction force of the supporting force of 10,901 N and a reaction force of the traction force of 10,000 N. The above loads were applied to the rigid-elastic coupled dynamic model.

In addition, the quality of the spring-type of anchoring mechanism is about 8 kg. Its gravity is 80 N, which can be neglected compared with other forces of several thousand N. The contact between the push rod joint and three spring-types of arms of anchoring mechanisms, and the contact between three leaf-spring and the wellbore were defined as "collision constraint", and the contact type was "spring-type of body to rigid body". The parameter values that used ADAMS to simulate and analyse contact pairs are shown in Table 3. "Contact resilience factor" is the stiffness, which reflects the ability of the two contacting bodies to resist deformation. "Force index" is used to calculate the index of the contribution of the material stiffness term in the instantaneous normal force.

Table 3. *Calculating parameters of contact force*

Parameters	Numerical value
Coefficient of static friction between the spring-type of anchoring arm and pipe wall (μ_1)	0.5
Coefficient of dynamic friction between the spring-type of anchoring arm and pipe wall (μ_2)	0.25
Contact resilience factor [N/mm]	10^5
Force index	1.5
Damping coefficient [N×s/mm]	1,000
Penetration depth [mm]	0.01

3.2 Simulation Analysis of Influencing Factors of Mechanical Characteristics of Spring-type of Anchoring Mechanism

Using the ADAMS/View software, the rigid model and the rigid-elastic coupling model were used to simulate the friction curve and the velocity curve of radial displacement of the spring-type of anchoring arm. In the initial state, a support force of 10,901 N and a load traction force of 10,000 N are applied to the two models respectively for five seconds, and the results are shown in Figs. 11 and 12.

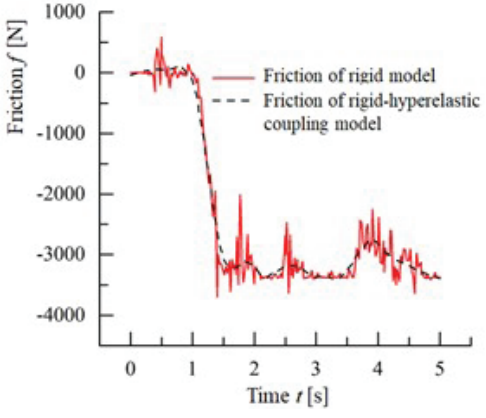

Fig. 11. *Friction curve of rigid model and rigid-elastic coupling dynamic model*

It can be seen from Figs. 11 and 12 that the rigid-elastic coupling model was more stable, more accurate, and superior to the rigid model data. The rigid-elastic coupling model can better reflect the motion characteristics of the spring-type of anchoring mechanism. Therefore, the rigid-elastic coupling model was used to simulate the spring-type of anchoring mechanism. The initial state of the rigid-elastic coupled model was loaded for 5 seconds, during which the force and velocity changes can be obtained.

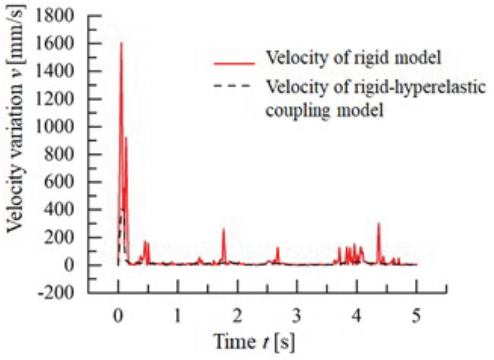

Fig. 12. *Velocity curve of rigid model and rigid-elastic coupling dynamic model*

Fig. 13 shows the force and velocity curves of the traction process of the spring-type of anchoring mechanism under the conditions of the supporting force of 10,901 N and the traction force of 10,000 N.

It can be seen from Fig. 13 that the friction force on a spring-type of anchoring arm also remained fluctuating around 3,333 N, which is the theoretical frictional force obtained from Eq. (3), after the traction force reached 10,000 N to maintain the level. This phenomenon indicated that the friction force generated by three spring-type of anchoring mechanism (about 10,000 N) can overcome the traction force to anchor the wellbore wall. The velocity of radial displacement started to fluctuate when it was first stressed, and finally gradually remained stationary with the wellbore wall. It indicated that the theoretically calculated supporting force of 10,901 N was able to overcome the traction force of 10,000 N applied to the traction robot to keep it locked with the wellbore wall.

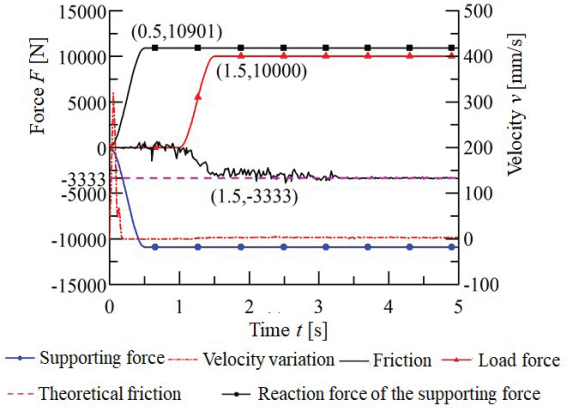

Fig. 13. *Force and velocity curves of the spring-type of anchoring mechanism (10,000 N)*

Figs. 14 and 15 show the force and velocity curves of radial displacement of the spring-type of anchoring mechanism in the 178 mm wellbore with traction forces of 14,000 N and 15,000 N respectively when the supporting force of 10,901 N remained constant.

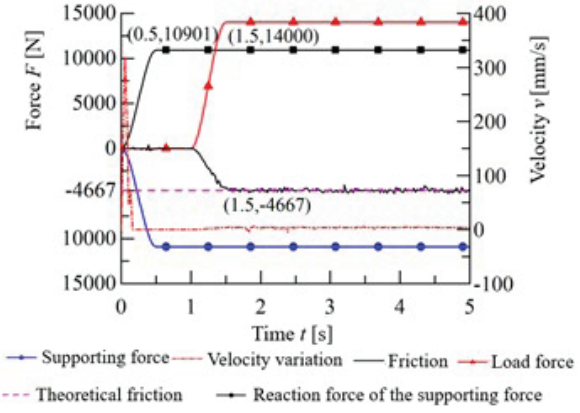

Fig. 14. *Force and velocity curves of the spring-type of anchoring mechanism (14,000 N)*

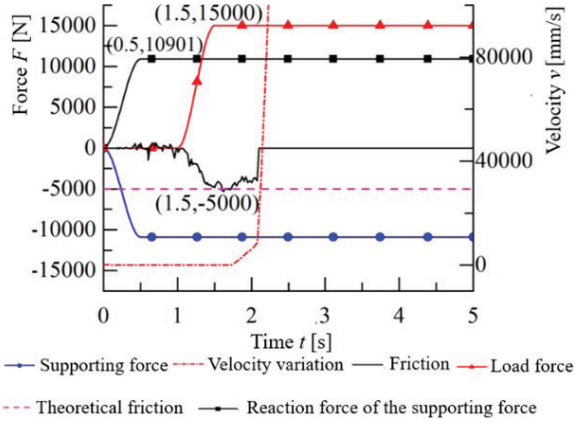

Fig. 15. *Force and velocity curves of the spring-type of anchoring mechanism (15,000 N)*

From Figs. 14 and 15 it can be observed that the spring-type of anchoring mechanism could continue anchoring when the traction force was 14,000 N. When the traction force was 15,000 N, it broke away from the wellbore wall after 1.9 s, and the anchoring failed. This phenomenon demonstrated that the anchoring mechanism cannot conquer the traction force of 15,000 N under the supporting force of 10,901 N, and the traction robot cannot sustain the anchoring with the wellbore wall. Thus, the maximum traction force interval of the spring-type of anchoring mechanism was gained between 14,000 N and 15,000 N in a 178 mm wellbore.

In order to observe the anchoring ability of the spring-type of traction robot under other sizes of the

wellbores, the motion of the traction robot in 165 mm wellbore and 152 mm wellbore was selected as the object of study in this paper. Their anchoring performance was simulated and analysed by applying theoretical supporting force of 10,417 N and 10,203 N respectively, as shown in Figs. 16 to 19.

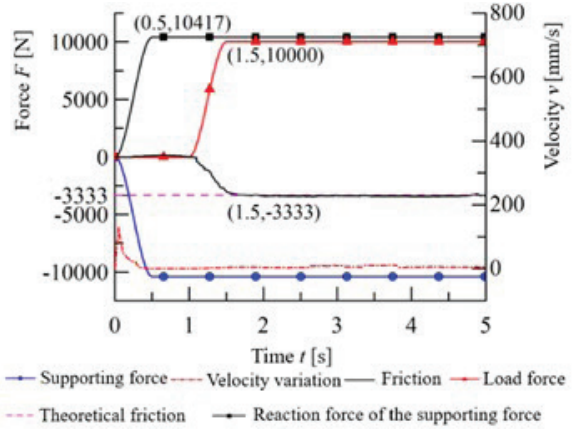

Fig. 16. *Force and velocity curves of anchoring mechanism in 165 mm wellbore (10,000 N)*

Similarly, it can be understood from Figs. 16 to 19 that the spring-type of anchoring mechanism was able to conquer the traction force of 10,000 N under the supporting force of 10,417 N in a 165 mm wellbore and 10,203 N in a 152 mm wellbore, respectively, to anchor it with the wellbore wall. The maximum traction force interval of the spring-type of traction robot was 12,000 N to 13,000 N and 10,000 N to 11,000 N separately.

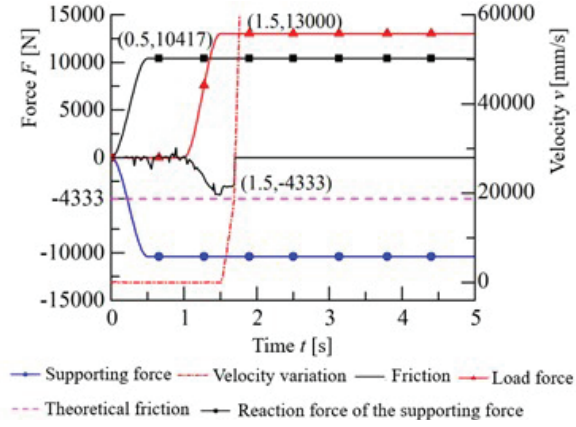

Fig. 17. *Force and velocity curves of anchoring mechanism in 165 mm wellbore (13,000 N)*

It was verified that the spring-type of traction robot can preserve anchoring under a design traction force of 10,000 N with 152 mm, 165 mm and 178 mm wellbores. At the same time, the maximum theoretical traction force intervals of 10,000 N to 11,000 N, 12,000 N to 13,000 N, and 14,000 N to 15,000 N were acquired for the corresponding sizes of wellbores. It was indicated that the maximum traction force of the traction robot would increase with the increase of the wellbore pipe diameter.

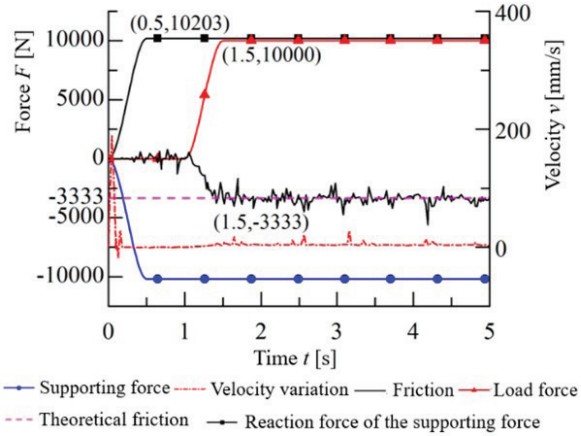

Fig. 18. *Force and velocity curves of anchoring mechanism in 152 mm wellbore (10,000 N)*

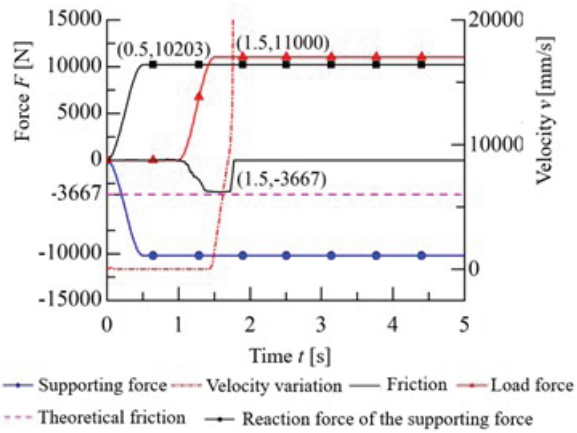

Fig. 19. *Force and velocity curves of anchoring mechanism in 152 mm wellbore (11,000 N)*

4 EXPERIMENTAL RESEARCH

The spring-type of anchoring arm of the final structure (span of 462 mm, chamfer radius of 40 mm, width of 30 mm and thickness of 5 mm) determined in Chapter 2 was made into an experimental prototype, which is shown in Fig. 20.

Fig. 20. *Spring-type of anchoring mechanism*

A simulation diagram of the experimental prototype is shown in Fig. 21 to better present its structure. The prototype was used to verify that the spring-type of anchoring mechanism can overcome the traction force of load to achieve anchoring to the wellbore wall under the theoretical support force of the supporting cylinder. The actual maximum traction force of the traction robot can be obtained from the prototype experiment. Also, the recovery effect of the spring-type of anchoring arm was observed after the unloading of the anchoring mechanism.

4.1 Experimental Steps

The experimental scheme of the anchoring mechanism of the spring-type of traction robot is shown in Fig. 22. The experimental procedure of the traction process was as follows:

(1) Hydraulic cylinder 1 was injected with liquid, so that the spring-type of anchoring arms contacted the wellbore wall. Then the voltage signal of the S-shaped pressure sensor was recorded.

(2) Hydraulic cylinder 1 continued to have fluid injected, so that the cylinder generated a supporting force of 10,901 N (voltage signal of S-shaped sensor is 4.48 V).

(3) Hydraulic cylinder 2 was filled with fluid, so that the hydraulic pressure in the cylinder reached 10,000 N (voltage signal of the spoke sensor is

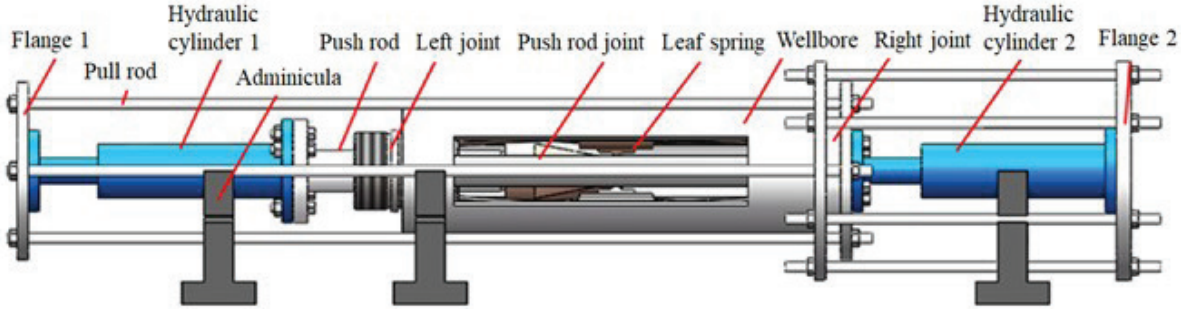

Fig. 21. *Schematic diagram of experimental equipment*

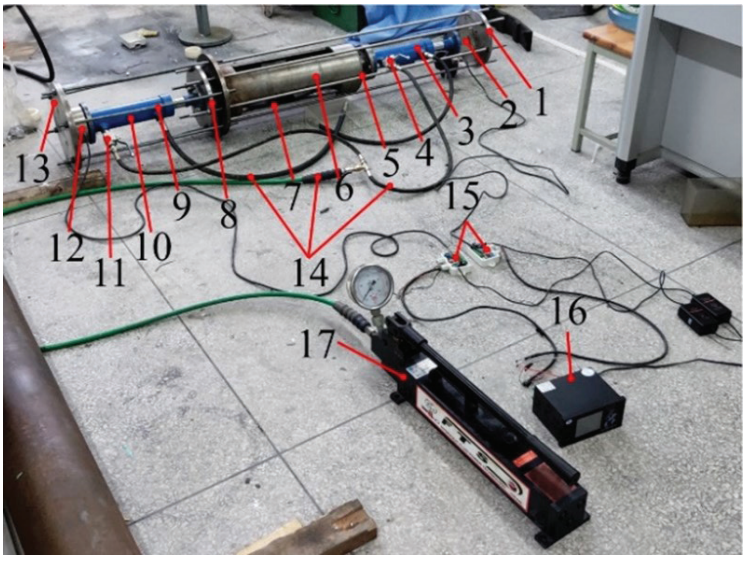

Fig. 22. *Experimental scheme and experimental system of spring-type of anchoring mechanism; 1 and 8 -flange 1, 2 s-type pull pressure sensor, 3 hydraulic cylinder 1, 4 and 11 manual high-pressure ball valve, 5 and 9 pull rod, 6 178 mm of wellbore pipe, 7 spring-type of anchoring mechanism, 10 hydraulic cylinder 2, 12 spoke pull pressure sensor, 13 flange 2, 14 hydraulic tube, 15 pressure transmitter, 16-Paperless recorder, 17-Manual high-pressure pump*

0.76 V). The anchoring condition of the anchoring mechanism was recorded.

(4) If the anchoring mechanism anchored the wellbore wall, hydraulic cylinder 1 continued to add pressure until the wellbore moved to the right. Also, the pressure in hydraulic cylinder 2 was recorded when the wellbore moved.

(5) Then, finally, the pressure in hydraulic cylinder 2 and hydraulic cylinder 1 was removed to observe the recovery of the spring-type of anchoring arm.

All measuring instruments had been calibrated before the experiment. All experimental instruments have a temperature compensation function, and the temperature has no effect on the measurement data. Therefore, the experimental errors are within the allowable range.

4.2 Experimental Results

The voltage data collected by the paperless recorder were converted into pressure data using the proportional coefficient. The pressure variation curves in hydraulic cylinder 1 (supporting force) and hydraulic cylinder 2 (traction force) are obtained as shown in Fig. 23.

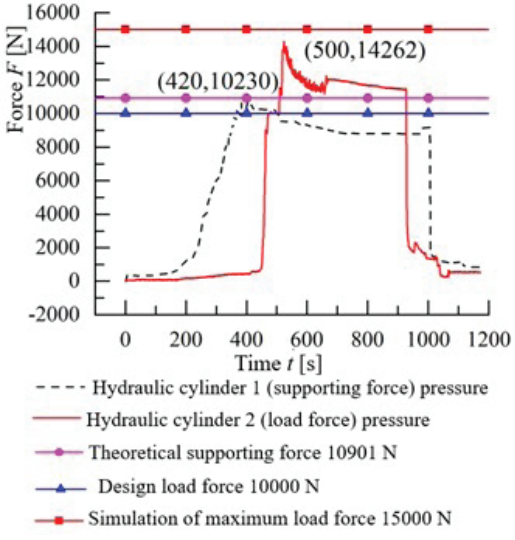

Fig. 23. *Theoretical and experimental support force curve*

Fig. 23 shows that after 400 s the pressure in hydraulic cylinder 1 (supporting force) was kept at 10,230 N, and the pressure in hydraulic cylinder 2 was maintained at about 10,000 N. The spring-type of anchoring mechanism remained relatively stationary with the wellbore. The reasonableness of the theoretical calculation was verified. The anchoring state between the anchoring mechanism and the wellbore wall is shown in Fig. 24, and the distance between the wellbore and the flange was 30 mm.

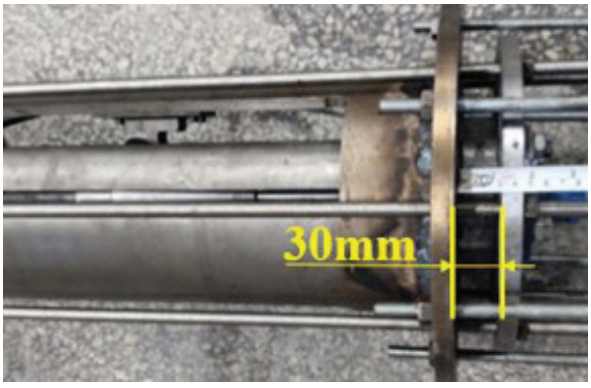

Fig. 24. *Anchoring state of spring-type of anchoring mechanism*

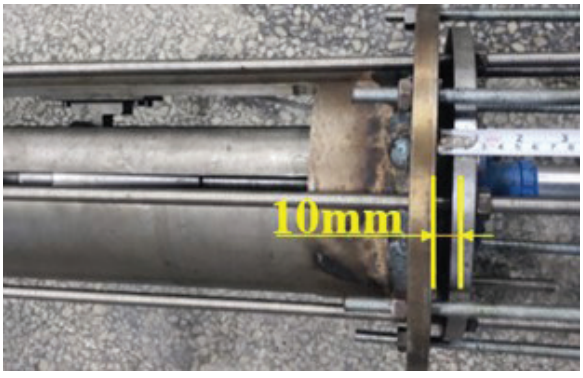

Fig. 25. *Anchoring failure state of spring-type of anchoring mechanism*

Continuing to feed liquid to hydraulic cylinder 2, its pressure was increased to 14,262 N and then began to decrease, while the pressure of hydraulic cylinder 1 began to decrease. Here relative sliding occurred between the anchoring mechanism and the wellbore wall, and the anchoring failed. It was illustrated that the maximum traction force was 14,262 N. The relative position of the wellbore and the spring-type of anchoring mechanism is shown in Fig. 25 after the experiment, and the distance between the wellbore and the flange was 10 mm.

Table 4. *Comparison of theoretical and experimental data of support force and traction force*

	The supporting force	The maximum traction force
Experimental value [N]	10,230	14,262
Simulation value [N]	10,901	15,000
Deviation [%]	6.1	4.9

From Table 4, the experimental results showed that the simulation values did not differ much from the experimental values. the correctness of the mechanical analysis, the optimization of the leaf spring and the rigid-elastic coupling model were verified. However, the experimental results also exposed some problems. After hydraulic cylinder 1 was decompressed, the spring did not reset quickly, and only slowly retreated after an external force was applied. The reason for this was due to safety concerns. Hydraulic cylinder 1 released the pressure slowly, so that the elastic restoring force of the spring-type of anchoring arm was also slowly reduced, and resulted in the arm returning slowly.

5 CONCLUSIONS

(1) In this paper, a novel spring-type of anchoring mechanism of a traction robot based on inclined blocks was proposed, which can provide a large traction force for the robot and can avoid being stuck. Meanwhile, the mechanical analysis of the traction process was completed, and the structure of the spring-type of anchoring mechanism was optimized.

(2) Through establishing the rigid-elastic coupling model of the spring-type of anchoring mechanism, it was determined that the rigid-elastic coupling model can better reflect the motion characteristics of the traction robot compared with the rigid model. At the same time, through analysis of the rigid-elastic coupling model simulation, the correctness of the theoretical mechanical calculation of the spring-type of anchoring mechanism was verified, and the maximum traction force under different structural parameters was obtained.

(3) Through the experiment, it was verified that the experimental supporting force required to overcome the load of 10,000 N was 10,230 N, which was 6.1 % different from the theoretically calculated value. The maximum traction force that the traction robot anchoring mechanism can provide was 14,262 N, which was 4.9 % different from the simulated calculated value. The experiment result showed the correctness of the theoretical calculation, the optimization of the structure of the anchoring arm, and the simulation of the rigid-elastic coupling model.

The research results of this paper lay a foundation for the structural design and engineering application of spring-type of traction robot. It can effectively ensure the downhole safety of oil and gas wells.

6 ACKNOWLEDGEMENTS

This work was funded by the National Natural Science Foundation of China (No. 52004232, U19A200380), the Sichuan Science and Technology Program (23QYCX0060, JG2021-624, 2021YFS0305, 22QYCX0196) and the Sichuan Provincial Key Lab of Process Equipment and Control (GK202006). The authors also sincerely thank the editors and the reviewers for their efforts in improving this paper.

7 REFERENCES

[1] Saeed A., French, A., Moore, N.B. (2020). Analysis and case study: Comparing CT slim tractor performance using different CT sizes in 3 wells. *SPE/ICoTA Well Intervention Conference and Exhibition*, art. ID SPE-199871-ms, **DOI:10.2118/199871-ms**.

[2] Zhao, J., Han, S., Liu, Q., Zhang, Y., Xiao, X., Dong, R., Fang, S., Tu, C. (2022). Combined control mechanism of weight on bit and rate of penetration with a downhole robot in the coiled-tubing drilling process. *SPE Journal*, vol. 27, no. 1, p. 153-166, **DOI:10.2118/208570-PA**.

[3] Alsaiood, H., Otaibi, A., Duthie, L., Aybar, U., French, A. (2020). Powerful hydraulic coil tubing tractor facilitates stimulation application in extended reach wells thru completion operations. *SPE/ICoTA Well Intervention Conference and Exhibition*, art. ID SPE-199851-MS, **DOI:10.2118/199851-ms**.

[4] He, L., McAllister, J., Hawkins, J., Turner, M. (2020). Application of downhole tractor in gas well zonal isolation. *SPE/ICoTA Well Intervention Conference and Exhibition*, art. ID SPE-199830-MS, **DOI:10.2118/199830-ms**.

[5] Xiao, X., Dai, J., Zhu, H., Zhao, J. (2021). Experimental and numerical simulation research on eccentric flow channel erosion of drilling robot. *Journal of Southwest Petroleum University (Science & Technology Edition)*, vol. 43, no. 2, p. 167-177, **DOI:10.11885/j.issn.1674 5086.2020.11.02.01**. (in Chinese)

[6] Badeghaish, W., Noui-Mehidi, M.N., Al-Mulhem, A.A. (2018). Comprehensive review of well tractor technology in highly extended reach wells. *SPE/ICoTA Coiled Tubing and Well Intervention Conference and Exhibition*, art. ID SPE-189906-MS, **DOI:10.2118/189906-ms**.

[7] Denney, D. (1999). Wireline-tractor production logging in horizontal wells. *Journal of Petroleum Technology*, vol. 51, no. 3, p. 80-81, **DOI:10.2118/0399-0080-JPT**.

[8] Heaney, F.M., Lee, M.L., Gupta, S. (2022). New torque balancing algorithm improves pulling force and speed with wireline electro-mechanical tractor. *SPE/ICoTA Well Intervention Conference and Exhibition*, art. ID SPE-209010-MS, **DOI:10.2118/209010-ms**.

[9] Saeed, A., Duthie, L., Yaklovlev, T., Sagr, H. (2017). Development and world's first field deployment of 2.125? tridem coiled tubing tractor for extended reach open hole horizontal wells with ESP completions. *Abu Dhabi International Petroleum Exhibition & Conference*, art. ID SPE-188283-MS, **DOI:10.2118/188283-ms**.

[10] Tyagi, C., Singh, V., Nayak, J.P., Pinto, T. (2017). Unique milling bit deployed via e-line intervention enables operator to achieve early production. *SPE/ICoTA Coiled Tubing and Well Intervention Conference and Exhibition*, art. ID SPE-184786-MS, **DOI:10.2118/184786-ms**.

[11] Formica, J., Wise, J., Boye-Moller, C., Davis, B., Godfrey, B., Walker, C. (2004). Tractor-conveyed sensors and chemical packer are utilized to remediate an extended-reach horizontal uncemented slotted liner completion in a siliceous shale reservoir, Kern County, California, USA. *SPE International Thermal Operations and Heavy Oil Symposium and Western Regional Meeting*, art. ID SPE-86938-MS, **DOI:10.2118/86938-ms**.

[12] Nakazato, Y., Sonobe, Y., Toyama, S. (2012). Development of in-pipe micro mobile robot using peristalsis motion driven by hydraulic pressure. *Micromechanics and Microactuators, Mechanisms and Machine Science*, vol. 2, p. 23-29, **DOI:10.1007/978-94-007-2721-2_3**.

[13] Grigore, L.S., Oncioiu, I., Priescu, I., Joita, D. (2021). Development and evaluation of the traction characteristics of a crawler EOD robot. *Applied Sciences*, vol. 11, no. 9: art. ID 3757, **DOI:10.3390/app11093757**.

[14] Nagase, J.Y., Fukunaga, F., Shigemoto, Y. (2017). Cylindrical elastic crawler mechanism for pipe inspection. *Advances in Cooperative Robotics*, p. 304-311, **DOI:10.1142/9789813149137_0037**.

[15] Gao, S., Li, C., Sun, W. (2014). Structural design and mechanical analysis of expansion brake for downhole tractor. *Science & Technology Information*, vol. 12, no. 19, p. 92-95, **DOI:10.16661/j.cnki.1672-3791.2014.19.170**.

[16] Liu, Q., Zhao, J., Zhu, H., Zhang, W. (2019). Mechanical model of drilling robot driven by the differential pressure of drilling fluid. *Arabian Journal for Science and Engineering*, vol. 44, p. 1447-1458, **DOI:10.1007/s13369-018-3578-3**.

[17] Liu Q., Zheng W., Yang Y., Zhang S., Zhu H. (2018). Two-way locking mechanism design for telescopic downhole tractors. *Journal of Southwest Petroleum University (Science & Technology Edition)*, vol. 40, no. 1, p. 1, DOI:10.11885/j.issn.1674-5086.2016.12.24.01. (in Chinese)

[18] He, C., Zhao, J., Li, Z., Wang, Z., Han, S., Zhang, Y., Xiao, J. (2021). Design method and mechanical analysis of gripping mechanism of drilling robot. *Arabian Journal for Science and Engineering*, p. 11197-11209, **DOI:10.1007/s13369-021-05898-9**.

[19] Yaakoubi, M., Kchaou, M., Dammak, F. (2013). Simulation of the thermomechanical and metallurgical behavior of steels by using ABAQUS software. *Computational Materials Science*, vol. 68, p. 297-306, **DOI:10.1016/j.commatsci.2012.10.001**.

[20] Zhao, J., Peng, H., Fang, S., Wang, K., Han, S., Zhang, Y., Zhu, Z., Tu, C. (2021). Study on dynamic sealing performance of combined sealing structure of telescopic type of downhole robot by using HTHP coupling method. *Science Progress*, vol. 104, no. 3, **DOI:10.1177/00368504211013214**.

[21] Xu, F. (1989). *Calculation of Friction Force Caused by O-ring. Petroleum Machinery*, no. 08, pp. 9-10+35. (in Chinese)

[22] Xiao, S. (2001). Calculation of frictional force of o-type sealing ring in hydraulic vat. *Journal of Southern Institute of Metallurgy*, no. 1, p. 18-20, **DOI:10.13265/j.cnki.jxlgdxxb.2001.01.005**. (in Chinese)

[23] Zuo, X., Zhang, J. (1989). Study on Friction Force of O-type Auxiliary Seal Ring of Mechanical Seals. *Journal of Fluid Engineering*, no. 04, p. 1-8. (in Chinese)

[24] Yan, H., Li, J., Kou, Z., Liu, Y., Li, P., Wang, L. (2022). Research on the traction and obstacle-surmounting performance of an adaptive pipeline-plugging robot. *Strojniški vestnik - Journal of Mechanical Engineering*, vol. 68, no. 1, p. 14-26, **DOI:10.5545/sv-jme.2021.7361**.

Strojniški vestnik - Journal of Mechanical Engineering 68(2022)11, 683-692
DOI:10.5545/sv-jme.2022.321
Original Scientific Paper
Received for review: 2022-08-08
Received revised form: 2022-10-01
Accepted for publication: 2022-10-17

Optimization Techniques for Green Layout Design in Manufacturing Industries: A Meta-Heuristic Analysis

Sheik Sulaiman Sherfudeen[1,*] – Muthiah Athinamilagi[2] – Janakiraman Venkataramanujam[3]

[1]Francis Xavier Engineering College, Department of Mechanical Engineering, India
[2]P.S.R.Engineering College, Department of Mechanical Engineering, India
[3]Vaigai College of Engineering, Department of Mechanical Engineering, India

Many research papers and much legislation has been published in recent years to control or reduce factory pollution. However, only a few articles have discussed pollution from manufacturing facilities, specifically shop floors, even though this a specific single objective problem. In this research framework, a new variant technique of the jelly fish concept adaptive salp swarm optimization (ASSO) with a familiar Lagrangian relaxation model for lowering Total Material Handling Costs (TMHC) and carbon dioxide (CO_2) emissions is presented. Using the Mat Lab software and the improved ASSO, the dragon fly optimization (DFO) algorithm technique, experimental simulations of the existing and recognized design of the studied industry were performed. The simulation results were validated and compared to those of other optimization techniques such as ant bee colony (ABC), simulated annealing (SA), and genetic algorithm (GA). It was determined that the proposed methodology, ASSO, was the most efficient, resulting in 40 % reduction compared to ABC, 38 % DFO, 50 % SA, and 40 % GA in the lowest TMHC, as well as an average 20 % reduction of emission rate in green layout design. These techniques could be combined into a hybrid format for further reduction of the emission rate up to 80 %.

Keywords: adaptive salp swarm optimization, bi-objective function, emission, evolutionary computation, layout design, and total handling costs

Highlights

- *This study will improve the efficiency of workflow within the workplace allowing workers and equipment being more productive.*
- *A new variant technique of the jelly fish concept - adaptive salp swarm optimization and dragon fly optimization techniques were introduced for design optimization.*
- *Lowering total material handling costs and CO_2 emissions a Lagrangian relaxation model equation derived.*
- *The experimental results are compared with five different optimization techniques with specified algorithm of programs.*

0 INTRODUCTION

The logistic network dilemma (LNDP) has received much attention recently. This problem is divided into two parts: (i) a location problem, which involves deciding where logistics nodes (such as logistics parks, distribution centres, and logistics terminals) should be located, and (ii) an allocation problem, which involves routing the flow of goods from origin to destination [1]. One of the most important strategic considerations for logistics companies is where to establish logistics facilities and which ones should service which customers. Environmental considerations are increasingly being considered in classic capacitated facility site problems in response to the introduction of sustainable supply chain management. The logistics process aims to reduce transportation-related costs, such as distance travelled, time, route flexibility, and reliability. Furthermore, based on present trends in fuel consumption and carbon dioxide (CO_2) emissions, these are expected to rise by approximately 50 % by 2030 and by 80 % by 2050 [2]. As a result, transportation businesses and governments are beginning to explicitly include emission reduction goals in the development of their work plans [3].

Converting existing logistics systems to be more environmentally friendly can save money while still allowing them to meet traditional logistical goals in some cases [4]. Furthermore, the green transportation system might be completed by defining emission characteristics and measuring vehicle emissions by integrating them into logistics system networks [5]. In view of current environmental concerns and high levels of entrepreneurship, enterprises [6] should benefit from using bi-objective optimization (BOO) improvement tactics when developing distribution networks [7], allowing them to satisfy multiple primary objectives at the same time.

Optimization methodologies [8], such as BOO and vehicle carbon tax legislation, can help reduce CO_2 emissions. As a result, the salp swarm model has been taken bi-objective problems into account while modelling and optimizing the logistics centre location and allocation problems for better reliability [9]. The intelligence of natural swarms, herds, schools, or flocks of animals is the basis for swarm intelligence techniques. The primary foundation

*Corr. Author's Address: Francis Xavier Engineering College, Department of Mechanical Engineering, India, sssulaiman1980@gmail.com

of these algorithms is derived from the collective behaviour of a group of organisms [10]. Scientific research on this organism remains in its early stages due to the difficulty of accessing their natural habitats and keeping them in laboratory surroundings. A numerical example in which the impacts of fuzziness on issue optimization are measured and a comparison between the CO_2 emission optimization approaches were made. An improved multi-objective algorithm has been developed for optimization of supply chain management in natural gas handling industries [11] and this model is to minimize economic and environmental costs. Similarly, a closed loop [12] supply chain logistics model was implemented in manufacturing industries for the reduction of handling costs.

A fuzzy multi-objective optimization model was developed [13] for a network design including the design of both forward and reverse supply chain for reduction of total handling costs and CO_2 emission rates [14]. The optimization module is used to minimize the following constraints: raw material, semi-finished, finished product flows, and outsourcing decisions [15].

A hybrid algorithm introduced by Peng et al. [16] to define various neighbourhood operations and the vehicle operations at full workload conditions. Asghari et al. [17] proposed a classification scheme based on its variants considered in three major and applicable streams, including internal combustion engine vehicles, alternative-fuel-powered vehicles, and hybrid electric vehicles, to reduce CO_2 emission [18].

In variations of green vehicle route problem (GVRPs), it has been suggested that multi-objective optimization models be considered, as well as to establish a green vehicle route [19] offer a branch and price (BAP) improved algorithm for solving the heterogeneous fleet green car routing problem with time frames with precision. Xu et al. [20] introduced a genetic algorithm, an excess rectangle fill algorithm, which frames a specific type of inner structure and is incorporated into the model to distribute facilities to many blocks.

To minimize the total costs, which includes both investment and running expenditures, a quantitative method for assigning facilities is provided. Coral reefs optimization is a recently developed evolutionary-type technique to tackle numerous complex optimization issues [21].

Pourhassan and Raissi [22] has provided an approach to address the dynamic facility layout problem because material handling and related expenses can be minimized mathematically, and a modified non-dominated sorting genetic algorithm (NSGA-II) is projected to discover the best layout that meets the two important objective functions. The model for facility layout problem anticipated [23] is discussed. To implement the heuristic technique for updating layout design, a modified multi-objective particle swarm optimization algorithm is given.

Latifi et al. [24] present an integrated solution to the problem of process plant layout that takes into account both profitability and protection considerations. A new mathematical model is constructed for a facility layout that accounts for potential fire and explosion scenarios as well as the danger of a fatal toxic leak. D'Antonio et al. [25] introduced a mathematical model for defining a hybrid product-process architecture employing hybrid facility layout mathematical modelling and based on a genetic algorithm (GA).

1 PROBLEM FORMULATION

The primary focus of this research is to develop and evaluate search heuristics to find nearer-to-optimal solutions to the facility layout problems related to manufacturing industries. In this research work, a mathematical model will be formulated to address the major current issues of unequal area facility layout problems considering block layout, detailed facility layout issues like inter department layout, input/output (I/O) locations, and flow path (for materials) layout design and to cover the wide range of layout problems.

The integrated layout design issue of poorly balanced facilities and sites considering procurement and management and pickup, and the circulation networks are all addressed in this article. A medical equipment producer with small batch production of complex medical vital systems is the driving force behind it. Emissions from handling operations between divisions are analysed in order to develop a computational formula for vehicle CO_2 emissions on the plant floor. In this paper, two major issues are addressed: CO_2 emissions and the machine's total handling costs in terms of materials. The performance of vehicle carbon tax regulation in lowering vehicle CO_2 emissions in the logistics network is based on evidence of the benchmark, i.e., Pareto solutions [26], supplied by BOO in a numerical instance [27].

The vehicle CO_2 emissions of the final block arrangement, as expressed by the optimization problem: the basic data must be structured before the block layout can be built. The initial step is to create

a partial block layout of the departments with the greatest E_{ij} value, then gradually add the rest to finish the final plant layout as

$$\sum E_{ij}(q,d) = d_{ij} \times \left(\frac{q_{f1} - q_{f2}}{Q} \right) p_{ij} + q_{el}. \quad (1)$$

Eq. (1) represents $E_{ij}(q,d)$ is the CO_2 emissions from a vehicle [kg/km] with the variable of load q [10^3 kg] and d in [km]. q_{f1} and q_{f2} is CO_2 emissions of a fully loaded and the CO_2 emissions of an empty vehicle. Q is the volume capacity of a vehicle. $E_i \leftrightarrow E_j, \forall, j \in [1,n]$. The second sub-problem is the rule-based approach to the "block layout" design [28].

1.1 Constraints with Scheduling Model

To locate a delivery route that satisfies the requirements of distribution points and obtains the shortest travelled expenses and the least amount of emitted CO_2 while visiting each customer with respect to vehicle's capacity constraints, see Eq. (2)

$$\sum\sum\sum \text{cost}_{ij} \times x_{ij}. \quad (2)$$

1.2 Research Gap Findings

The following research gap findings were observed:

- Solutions have been derived as single objective optimization techniques only.
- In manufacturing layout, inter-cell department production material movements (number of times) and distance moved are not taken into account.
- Emission control systems (CO_2), material handling vehicles travelled in and between productions departments are not highlighted.
- Energy consumption of machines, material handling systems, and workmen density are not accounted.
- Multi-objective function solutions are minimal and detailed layout-design study is more required.

2 METHODOLOGY- SOLUTION FOR PROBLEM FINDING

Some objectives are suggested to enhance efficiency and material consumption, such as total material handling cost (TMHC) and decreasing CO_2 total emission (E) from various equipment during production time. Apart from CO_2 emissions, the main goal of this bi-objective problem to cost criteria is to address highly significant aspects in the location process. Then CO_2 emissions for industrial companies are not only a legal need, but also a production process for corporations to compete. The output regularity is closely related to the suggested plant layout design; however, the interdepartmental flow values and functional annotation are very important variables to consider in the cell process [29].

The energy consumption of a commonly used material handling vehicle [30] on an industrial floor shop is primarily determined by the number of hours and shifts that it has been utilized. The Gas Technology Institute (GTI) projected yearly runtimes in various industries ranging from 500 hours to 3500 hours for battery-powered material handling vehicles and 1800 hours to 1900 hours for internal combustion engine-powered vehicles in 1995 [30]. The first agency's centre length is calculated first, and then the other agencies' centres are measured, resulting in the centre-to-centre length between each section. Measurements were taken, and the distance between each division was recorded; in total, 15 systems can be considered, as in Fig.1.

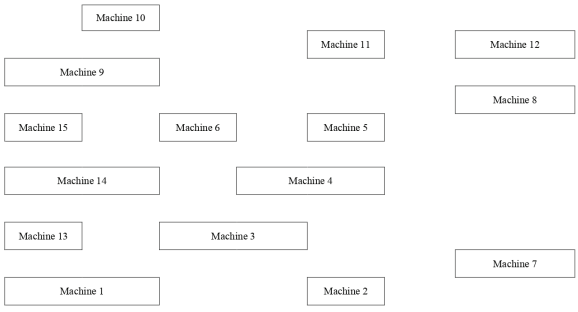

Fig. 1. *Existing layout*

2.1 Objectives of Proposed Model

The following objectives of proposed model were observed:

- The goal of our research is to develop route and transport strategies that provide the optimal balance of TMHC travel and CO_2 emissions.
- To create the best layout while taking into account of the distance between departments for manufacturing materials management among terminals
- The focus is to reduce the overall CO_2 emissions using an Adaptive Salp Swarm Optimization (ASSO), i.e., Meta heuristic optimization technique.
- To compare the outcomes of the ASSO models with those of other methods, such as ant bee

colony (ABC), dragon fly optimization (DFO), simulated annealing (SA), and genetic algorithm (GA), in terms of the goals.

2.2 Mathematical Modelling for the Optimization Technique

The BOO approach, as a result, produces a transaction situation in which the responsible party has the ability to visualize the design along with adequate options to meet all of the primary objectives. The final layout design aims to lower the total CO_2 emissions from the workstation. The proposed optimization technique, ASSO, has a positive correlation with the reduction of overall flow and energy consumption at the various department positions. The resulting operating plans must then be as cost-effective as possible while also reducing CO_2 emissions. These two goals are not always in sync; in some situations, they are in direct opposition to one another.

a) Total Material Handing Cost (TMHC). Materials management costs are an important part of a manufacturer's profit calculation. If these are disregarded while assessing production costs, the company's potential profit will be overestimated. Analysing material costs also aids the organization in devising strategies to cut future costs. Costs differ depending on the industry and location [30]. To reduce handling costs and maximize available space, the functional areas should be organized close together but not in conflict with one another. This is described below in Eq. (3) and Eq. (4).

$$TMHC = \sum T_{ij} \cdot M_{ij} \cdot D_{ij}, \tag{3}$$

$$\min(E) = weight(TMHC), \tag{4}$$

here, T_{ij} are the cost for the material transport between the machines, M_{ij} materials flow between the machines and D_{ij} distance between machines. If a corporation distributes multiple products at once, it must divide handling costs among them to acquire an accurate estimate of each product's actual cost [30].

b) CO_2 Emission Level. The rate of CO_2 emission provides a clear picture of an industrial organization's international environmental approach. Pollution from the engine can be calculated using the quantity of gas consumed. Forklifts generally utilize conventional diesel, and since they are off-road vehicles, they are not subject to road fees. The total amount of CO_2 produced per ton of vehicle is determined by the number of vehicles, the average distance travelled, and the amount of fuel consumed in vehicles, as well as the unpredictable impacts of climate change. This is written in the equation Eq. (5).

$$E_{total} = E_{start} + E_{hot} + E_{Evaporative}, \tag{5}$$

here E_{total} is the total emission, E_{hot} it denotes emission during hot engine conditions, E_{start} denotes emission during the start of the engine, $E_{evaporative}$ denotes emission due to evaporation. Whenever an engine motor is restarted at a lower-than-normal operating temperature, typically, the criteria utilized to construct a matrix of length, duration, and price between all distribution centres and the depots are separation, time, and cost. The goal now is to develop routes that emit the least amount of CO_2 into the atmosphere; to accomplish this, a vehicle with CO_2 emission matrix based on the estimated CO_2 emitted between every link must be created [31].

2.3 Procedure of Salp Swarm Optimization

Salps play a role in the reconciling process; it includes a swarm. Their cells are remarkably similar to those of jellyfish. It travels in the same way that jellyfish do, with liquid pumped through the body as an impetus to move forward. Normally, the swarm's goal is to take the most space from a food supply. Going with the scenario is suggested to inform the present status, as well as a flow diagram shown in Fig. 2.

(i) Initialization: The system structure weights are relegated as the initial solution when using the salps. The number of assignments is decided by the additional sub term occurrences [31], in the material depicting the machine and the function represented in condition mentioned in Eq. (6).

$$\mathbf{R} = \begin{bmatrix} R_{11} & R_{12} & \ldots & R_{1n} \\ R_{21} & R_{22} & \cdots & R_{2n} \\ \vdots & \vdots & \ddots & \vdots \\ R_{n1} & R_{n2} & \ldots & R_{nn} \end{bmatrix}. \tag{6}$$

The vector terms in the R direction of cypher to minimize the optimization problem via a benchmarking problem are derived from constraints Eq. (6).

(ii) Objective Function for Condition Evaluation. This trend is important for both information cost and emissions in any situation where the cost and emission rate must be kept to a minimal. Its fitness appears to be in good shape Eq. (7).

$$\min \sum \sum \text{TMHC and emission cost.} \quad (7)$$

(iii) New solution Updating Procedure: The first vector is the leading salp. It will, to some extent, migrate towards food as the leader to fulfil its leadership role. Normally, the swarm's purpose is to obtain food from the hunt space, which is seen in Fig. 3, the following condition Eq. (3) to Eq. (5) is proposed to update the leader's situation:

$$Swram\ (New)_j^1 = \begin{cases} T_j + Q_1\left[\left(H_j - L_j\right)Q_2 + L_j\right], Q_3 \geq 0 \\ T_j - Q_1\left[\left(H_j - L_j\right)Q_2 + L_j\right], Q_3 < 0 \end{cases}, \quad (8)$$

$$Q_{1...3} = 2e^{(-4l/L)}, \quad (9)$$

$$weight_j^i = \frac{1}{2}\left[w_j^i + w_j^{i-1}\right]. \quad (10)$$

where T_j^1 signifies the position of the first part (leader) in j^{th} cell. The position of the machines in j^{th} cell is symbolized as T_j; the upper bound and lower bound is indicated as H_j and L_j; Q_1, Q_2 and Q_3 indicates a random number randomly generated in the interval of [0,1].

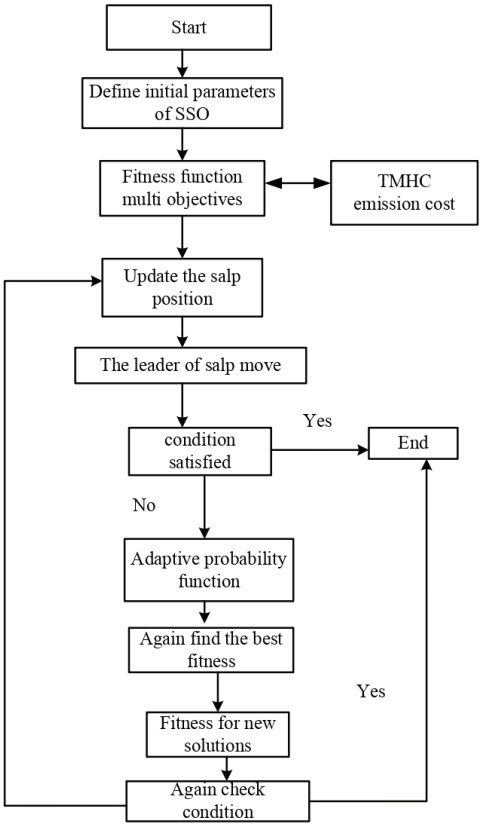

Fig. 2. *Flow chart for ASSO*

The coefficient is the most essential parameter in SSO since it affects the exploration and exploitation shown in Eq. (10), as well as the next step: weight discovery The food supply will be refreshed during optimization, as the salp chain is known for exploring and exploiting the space around it in pursuit of a better solution.

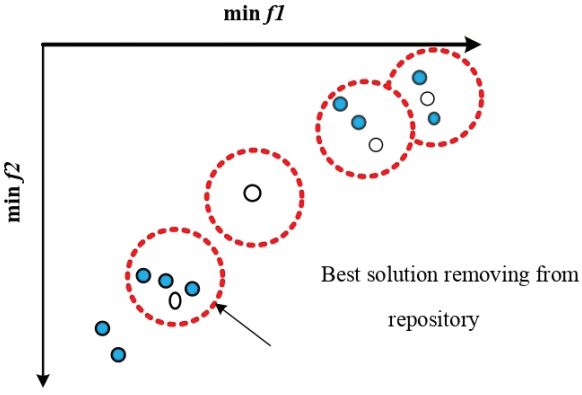

Fig. 3. *Repository update*

(iv) Adaptive function. To find a new solution for perfect fitness, use the coefficient vector acquired from the flexible probability function. The best features include less parameter dependence, the elimination of the need to describe the initial parameter, and the ability to change step size or position towards an ideal solution based on its functional fitness value through iteration, in order to discover the coefficient vector received by the flexible probability function.

$$y \Rightarrow \text{Probability} = \begin{cases} \dfrac{C_1(f_{\max} - f_x)}{(f_{\max} - F_{avg})}, & f_x \geq F_{avg} \\ C_3, & f_x \leq f_{avg} \end{cases}, \quad (11)$$

where $f_{\min}$ and $f_{\max}$ as greatest and least fitness functions, and C_1 and C_3 range between (0, 1). Throughout the iteration, the position toward an ideal solution adapts as indicated by its functional fitness value. As a result, when meta-heuristic algorithms are combined with adaptive systems, less computing time is required to find an optimal solution, nearby minimum avoidance is avoided, and convergence is faster.

The method for dealing with the green logistics problem is as follows:

- The location of each salp is obtained by initialising the salp population.

- The objective function is used to calculate the fitness for each salp position (TMHC and emission cost).
- Sort through all of the fitness and choose the best one to use as a food source.
- The first half of the people were picked as leaders, while the rest were chosen as followers.
- Update the salp leader's position using an equation, as well as the salp followers' positions.
- Use the salp's global optimum position as a new feeding source.

3 RESULTS AND DISCUSSION OF SIMULATION ANALYSIS

The test issue is supplied in the division using this input data and the mathematical model created in MATLAB 2020a with an Intel core i5 and 4GB RAM system setup. The efficiency of an answer in terms of minimizing travel lengths is compared using our method in contrast to other meta-heuristics such as ABC, DFO, SA, and GA, as shown in Table 1.

Table 1. *Simulation parameters for modelling*

Parameters	Values
Population size	120
Number of iterations	300
Fix handling cost	2151829
Number of machine shops	15

An assessment of the resolution quality in terms of minimizing travel lengths is made by comparing this improved technique with other methodologies that have not been attempted or for which a feasible solution has not been found in the literature. One goal of the comparison is to reduce the routing cost to the lowest level possible [32]. With respect to the number of iterations, our suggested optimizing technique delivers a minimum emission rate and TMHC with populations of 60 and 120 in Table 2.

Table 2. *Bi- objectives results of ASSO model*

Iteration	Population size= 60		Population size= 120	
	TMHC	Emission rate	TMHC	Emission rate
100	2153000	248.82	2151278	244.2
150	2152390	233.64	2151193	236.6
200	2152305	221.3	2151013	179.25
250	2151829	215.68	2150923	162.16
300	2151824	187.9	2150834	134.6

Fig. 4 depicts the convergence graph as population size changes, including ABC, DFO, SA, and GA with proposed optimization issues for TMHC comparison. While traditional single-objective vehicle routing algorithms are unable to investigate the conflicting behaviour of objectives, the ASSO algorithm is capable of doing so for a bi-objective vehicle routing problem. In addition, inventory management emissions are decreased by reducing cycle time, which reduces the quantity of replenishment items and, as a result, reduces energy consumption. Considering the relationship between energy consumption and emission in various logistics activities [19], the appropriate cycle time for an efficient solution must be short enough to minimize total energy consumption while still being long enough to avoid too frequent replenishing.

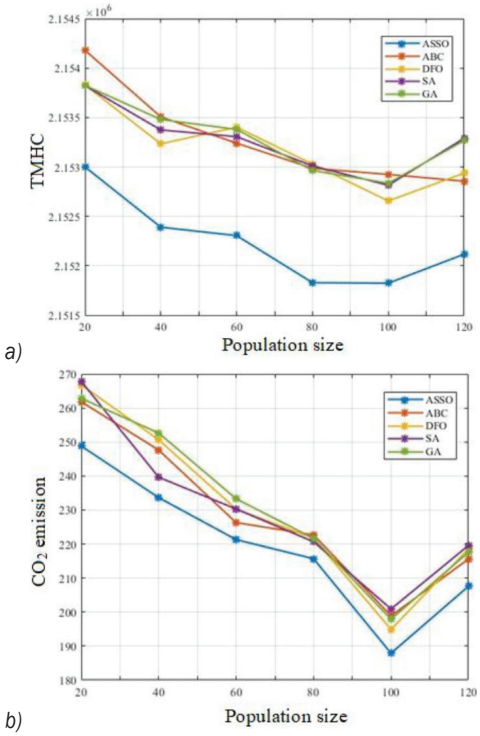

Fig. 4. *Convergence graph respect to population size; a) THMC, and b) CO_2 emission*

Total cost and total emission rate estimations include transportation, inventory management, and material-handling processes [33]. Material-handling operations include loading and unloading the utilized vehicle with products for refilling the goals. The utilized vehicle is restocked at the design constraint (DC) before being dispatched to resupply each sub-tour on each cycle trip. The final layout design's purpose is to lower the total CO_2 emissions from the workstation [1]. The reduction of total flow and energy consumption in proportion to population size

is strongly correlated with the locations of various departments in ASSO. One goal of the comparison is to reduce the routing cost to the lowest level possible. In terms of solution quality, the suggested model has proven to be economical with the finest available approaches. Fig. 5 shows the emission of TMHC as a function of iteration from 100 to 300, with the curve decreasing as the iteration level increases. Similarly to emission parameters, the difference between iteration level and objective function is 0.13 % to 0.25 %.

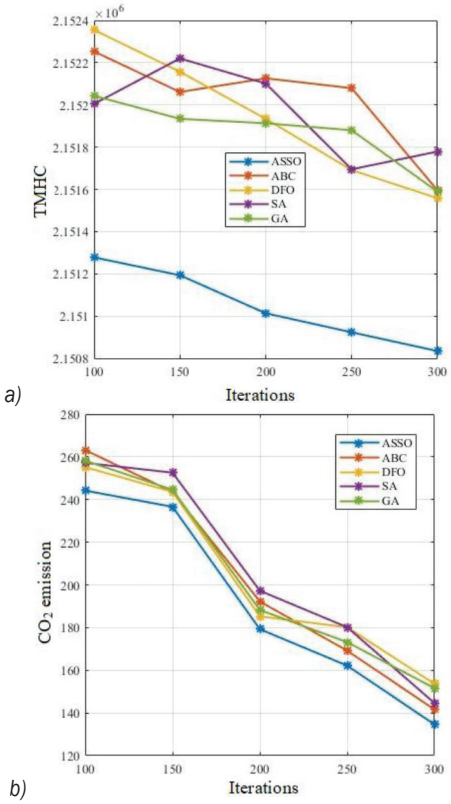

Fig. 5. *Convergence respect to number of iterations: a) THMC, and b) CO_2 emission*

The bi-objective function of the green logistics issue is shown in Fig. 6. Because customer demands are unpredictable, the following operations are repeated multiple times for each entire trip, with the average utilized to calculate the total travel cost [35]. The reason for this is that if there are too few customer queries for a certain route, truck capacity may be wasted, raising the overall cost of the route. The values of all objective functions are shown in this table as a function of population size. The difference between TMHC in ASSO and ABC is 10 %, while DFO's other algorithm is 12 %, 19 %, and emission parameters are similar.

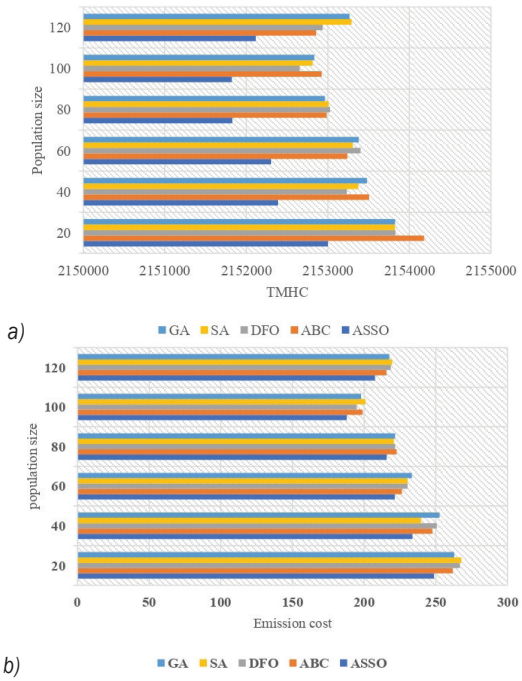

Fig. 6. *Comparative analysis for bi-objective function (iteration =300); a) THMC, and b) CO_2 emission*

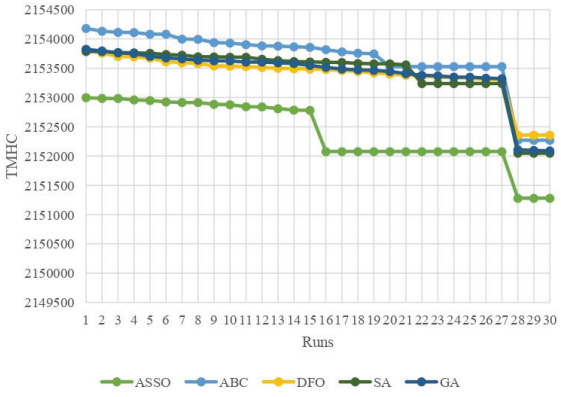

Fig. 7. *Number of runs based results for TMHC (population size = 90, iteration = 300)*

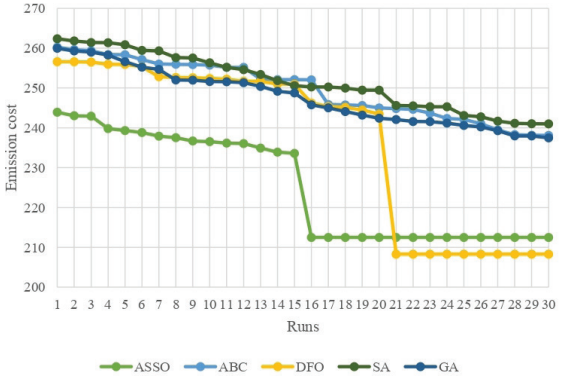

Fig. 8. *Number of runs based results for CO_2 emission (population size = 90, iteration = 300)*

Figs. 7 and 8 depict the several runs of the objective function in the carrying-out section, which is one of the membrane framework's key strengths. In ASSO, communication is between the control subsystem and the two operating systems [34], where the control subsystem applies a guiding approach to speed up convergence and improve solution quality. It can be seen that ASSO outperforms other optimization methods in terms of identifying solutions with lower overall costs shows in Fig. 6; this advantage is especially apparent when optimizing the total cost goal, and Fig. 7 shows the reduced emission rate.

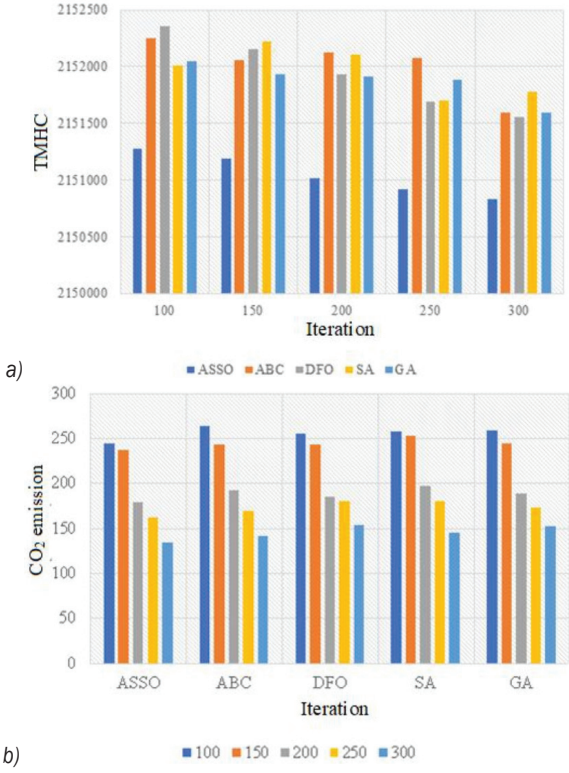

Fig. 9. *Comparative analysis; a) THMC, and b) CO_2 emission*

Fig. 9 depicts a comparison of the objective function TMHC and the emission cost, with one goal in mind: minimizing the route cost over the viable options. In terms of solution quality, the suggested algorithm has demonstrated the best available solutions. Fig. 9a depicts the optimization technique's TMHC values. It will be a nonlinear graph. Fig. 9b shows the emission rate comparison values for various optimization procedures, as well as the emission cost and emission rate that are close the best solutions The best facility layout [35] can be selected after running simulation results for different iterations and temperature conditions, as per set Table 1 parameters, and final layout after simulation runs, as shown in Fig. 10.

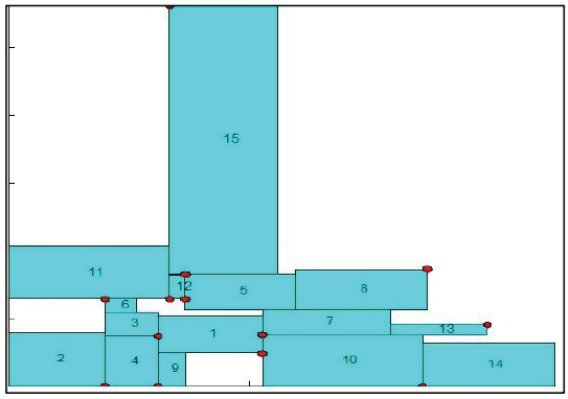

Fig. 10. *Best shop floor layout*

The new variant ASSO optimization technique has demonstrated significant cost savings in terms of material handling, with savings averaging 50 % when compared to other chosen techniques, according to this comparative analysis. Additionally, graphs of comparative emission rates for lower emission levels are shown. This implementation methodology can be effective in lowering emission rates and is very helpful for setting up new plant layouts prior to the installation of equipment. The main flaw in this methodology is that it necessitates complete layout design constraints for algorithm setup and development. In a select few instances, it will create intricate plant layout arrangements while taking into account all available resources [36].

4 CONCLUSION

The goal is to create workspaces that reduce vehicle emissions. This study looked at three major sources of CO_2 emissions in industries: TMHC associated with interdepartmental traffic, and emissions with gas consumption and electric consumption [37]. The target function in the proposed optimization ASSO model reflects a mix of the above three variables to make a green layout with as optimal vehicle emission rates as possible.

- The ASSO method uses a string of customer identities to signal the delivery sequence that a vehicle should cover throughout its route, functioning as a separator between two alternative swarm paths. Several experiments were conducted in order to exhibit the efficiency of the projected measures. The search history,

trajectory, average fitness, and closure curve were used as the first qualitative metrics.

- The proposed method was reasonably sufficient in comparison to the best available marks and the standard ASSO compared to ABC, DFO, SA, and GA performances were adequate, according to the results. This green layout design, 50 % TMHC and 25 % minimal emission rate were compared to other optimization techniques.

5 FUTURE SCOPE

Different hybrid optimization techniques will be used in the future to address the objective function in green logistics problems. Furthermore, the methods used to estimate the optimal adjustments can converge at the local optimal points **[38]**, as this will result in a useful plant layout.

6 NOMENCLATURE

E total emission from a vehicle, [kg/min]
q load, [kg]
d path way/distance travelled, [km]
Q volume capacity at full load, [kg]
$\mathbf{R}$ random matrix variable selection from constraints,
y probability function.

7 ACKNOWLEDGEMENTS

We ae very grateful and would like to extend our thanks to the supported industry in which the research is carried out in a productive way. It has been a great honour to be part of this industry through this research article. It is incredibly informative and useful for future research.

9 REFERENCES

[1] Atmayudha, A., Syauqi, A., Purwanto, W.W. (2021). Green logistics of crude oil transportation: A multi-objective optimization approach. *Cleaner Logistics and Supply Chain*, vol. 1, art. ID 100002, **DOI:10.1016/j.clscn.2021.100002**.

[2] Azadeh, A., Shafiee, F., Yazdanparast, R., Heydari, J., Fathabad, A.M. (2017). Evolutionary multi-objective optimization of environmental indicators of integrated crude oil supply chain under uncertainty. *Journal of Cleaner Production*, vol. 152, p. 295-311, **DOI:10.1016/j.jclepro.2017.03.105**.

[3] Cheaitou, A., Cariou, P. (2019). Greening of maritime transportation: a multi-objective optimization approach. *Annals of Operations Research*, vol. 273, p. 501-525, **DOI:10.1007/s10479-018-2786-2**.

[4] Gupta, P., Mehlawat, M.K., Aggarwal, U., Charles, V. (2018). An integrated AHP-DEA multi-objective optimization model for sustainable transportation in mining industry. *Resources Policy*, vol. 74, art. ID 101180, **DOI:10.1016/j.resourpol.2018.04.007**.

[5] Harris, I., Mumford, C.L., Naim, M.M. (2014). A hybrid multi-objective approach to capacitated facility location with flexible store allocation for green logistics modeling. *Transportation Research Part E: Logistics and Transportation Review*, vol. 66, p. 1-22, **DOI:10.1016/j.tre.2014.01.010**.

[6] Paksoy, T., Pehlivan, N.Y., Özceylan, E. (2012). Fuzzy multi-objective optimization of a green supply chain network with risk management that includes environmental hazards. *Human and Ecological Risk Assessment: An International Journal*, vol. 18, no. 5, p. 1120-1151, **DOI:10.1080/10807039.2012.707940**.

[7] Nurjanni, K. P., Carvalho, M.S., Costa, L. (2017). Green supply chain design: A mathematical modeling approach based on a multi-objective optimization model. *International Journal of Production Economics*, vol. 183, p. 421-432, **DOI:10.1016/j.ijpe.2016.08.028**.

[8] Attia, A.M., Ghaithan, A.M., Duffuaa, S.O. (2019). A multi-objective optimization model for tactical planning of upstream oil & gas supply chains. *Computers & Chemical Engineering*, vol. 128, p. 216-227, **DOI:10.1016/j.compchemeng.2019.06.016**.

[9] Nujoom, R., Mohammed, A., Wang, Q. (2018). A sustainable manufacturing system design: a fuzzy multi-objective optimization model. *Environmental Science and Pollution Research*, vol. 25, p. 24535-24547, **DOI:10.1007/s11356-017-9787-6**.

[10] Zhang, S., Zhuang, Y., Tao, R., Liu, L., Zhang, L., Du, J. (2020). Multi-objective optimization for the deployment of carbon capture utilization and storage supply chain considering economic and environmental performance. *Journal of Cleaner Production*, vol. 270, art. ID 122481, **DOI:10.1016/j.jclepro.2020.122481**.

[11] Zamanian, M. R., Sadeh, E., Amini Sabegh, Z., Ehtesham Rasi, R. (2020). A multi-objective optimization model for the resilience and sustainable supply chain: a case study. *International Journal of Supply and Operations Management*, vol. 7, no. 1, p. 51-75, **DOI:10.22034/IJSOM.2020.1.4**.

[12] Ma, W., Ma, D., Ma, Y., Zhang, J., Wang, D. (2021). Green maritime: A routing and speed multi-objective optimization strategy. *Journal of Cleaner Production*, vol. 305, art. ID 127179, **DOI:10.1016/j.jclepro.2021.127179**.

[13] Lanza, G., Moser, R. (2014). Multi-objective optimization of global manufacturing networks taking into account multi-dimensional uncertainty. *CIRP Annals*, vol. 63, no. 1, p. 397-400, **DOI:10.1016/j.cirp.2014.03.116**.

[14] Jayarathna, C.P., Agdas, D., Dawes, L., Yigitcanlar, T. (2021). Multi-objective optimization for sustainable supply chain and logistics: A review. *Sustainability*, vol. 13, no. 24) art. ID 13617, **DOI:10.3390/su132413617**.

[15] Cao, C., Li, C., Yang, Q., Zhang, F. (2017). Multi-objective optimization model of emergency organization allocation for sustainable disaster supply chain. *Sustainability*, vol. 9, no. 11, art. ID 2103, **DOI:10.3390/su9112103**.

[16] Peng, Bo, Wu, L., Yi, Y., Chen, X. (2020). Solving the multi-depot green vehicle routing problem by a hybrid evolutionary

algorithm. *Sustainability*, vol. 12, no. 5, art. ID 2127, **DOI:10.3390/su12052127**.

[17] Asghari, M., Al-e-hashem, S.M.J.M. (2021). Green vehicle routing problem: A state-of-the-art review. *International Journal of Production Economics*, vol. 231, art. ID 107899, **DOI:10.1016/j.ijpe.2020.107899**.

[18] Moghdani, R., Salimifard, K., Demir, E., Benyettou, A. The green vehicle routing problem: A systematic literature review. *Journal of Cleaner Production*, vol. 279 art. ID 123691, **DOI:10.1016/j.jclepro.2020.123691**.

[19] Yu, Y, Wang, S., Wang, J., Huang, M. (2019). A branch-and-price algorithm for the heterogeneous fleet green vehicle routing problem with time windows. *Transportation Research Part B: Methodological*, vol. 122, p. 511-527, **DOI:10.1016/j.trb2019.03.009**.

[20] Xu, S, Wang, Y., Feng, X. (2020). Plant layout optimization for chemical industry considering inner frame structure design. *Sustainability*, vol. 12, no. 6, art. ID 2476, **DOI:10.3390/su12062476**.

[21] García-Hernández, L., Salas-Morera, L., Garcia-Hernandez, J.A., Salcedo-Sanz, S., Valente de Oliveira, J. (2019) Applying the coral reefs optimization algorithm for solving unequal area facility layout problems. *Expert Systems with Applications*, vol. 138, art. ID 112819, **DOI:10.1016/j.eswa.2019.07.036**.

[22] Pourhassan, M.R., Raissi, S. (2017). An integrated simulation-based optimization technique for multi-objective dynamic facility layout problem. *Journal of Industrial Information Integration*, vol. , p. 49-58, **DOI:10.1016/j.jii.2017.06.001**.

[23] Li, S., Liang, Y., Wang, Z., Zhang, D. (2021). An optimization model of a sustainable city logistics network design based on goal programming. *Sustainability*, vol. 13, no. 13, art. ID 7418, **DOI:10.3390/su13137418**.

[24] Latifi, S.E., Mohammadi, E., Khakzad, N. (2017). Process plant layout optimization with uncertainty and considering risk. *Computers & Chemical Engineering*, vol. 106 p. 224-242, **DOI:10.1016/j.compchemeng.2017.05.022**.

[25] D'Antonio, G., Saja, A., Ascheri, A., Mascolo, J., Chiabert, P. (2018). An integrated mathematical model for the optimization of hybrid product-process layouts. *Journal of Manufacturing Systems*, vol. 46, p. 179-192, **DOI:10.1016/j.jmsy.2017.12.003**.

[26] Sun, Y., Lu, Y., Zhang, C. (2019). Fuzzy linear programming models for a green logistics center location and allocation problem under mixed uncertainties based on different carbon dioxide emission reduction methods. *Sustainability*, vol. 11, no. 22, art. ID 6448, **DOI:10.3390/su11226448**.

[27] Luo, Q., Zhu, J., Jia, H., Xu, Y. (2019). A two-stage layout method for functional areas in logistics park. Advances in Mechanical Engineering, vol. 11, no. 3, art. ID 1687814019829954, **DOI:10.1177/1687814019829954**.

[28] El Bouzekri El Idrissi, A., Elhilali Alaoui, A. (2014). Evolutionary algorithm for the bi-objective green vehicle routing problem. *International Journal of Scientific & Engineering Research*, vol. 5, no. 9, p. 70-77.

[29] Haddou Amar, S., Abouabdellah, A. (2016). Layout planning design: a mathematical-genetic approach for green logistics modeling. *3rd International Conference on Logistics Operations Management*, p. 1-7, **DOI:10.1109/GOL.2016.7731698**.

[30] Sulaiman, S.S., Jancy, P.L., Muthiah, A., Janakiraman, V., Gnanaraj, S.J.P. (2021). An evolutionary optimal green layout design for a production facility by simulated annealing algorithm. *Materials Today: Proceedings*, vol. 47, p. 4423-4430, **DOI:10.1016/j.matpr.2021.05.256**.

[31] Rau, H., Budiman, S.D., Widyadana, G.A. (2018). Optimization of the multi-objective green cyclical inventory routing problem using discrete multi-swarm PSO method. *Transportation Research Part E: Logistics and Transportation Review*, vol. 120, p. 51-75, **DOI:10.1016/j.tre.2018.10.006**.

[32] Gopi, R., Muthusamy, P., Suresh, P., Kumar, C.G., Santhosh, G., Pustokhina, I.V., Shankar, K. (2022). Optimal confidential mechanisms in smart city healthcare. *Computers, Materials & Continua*, vol. 70, no. 3, p. 4883-4896, **DOI:10.32604/cmc.2022.019442**.

[33] Niu, Y., Zhang, Y., Cao, Z., Gao, K., Xiao, J., Song, W., Zhang, F. (2021). MIMOA: A membrane-inspired multi-objective algorithm for green vehicle routing problem with stochastic demands. *Swarm and Evolutionary Computation*, vol. 60, art. ID 100767, **DOI:10.1016/j.swevo.2020.100767**.

[34] Guan, C., Zhang, Z., Liu, S., Gong, J. (2019). Multi-objective particle swarm optimization for multi-workshop facility layout problem. *Journal of Manufacturing Systems*, vol. 53, p. 32-48, **DOI:10.1016/j.jmsy.2019.09.004**.

[35] Hozdić, E., Kozjek, D., Butala, P. (2020). A cyber-physical approach to the management and control of manufacturing systems. *Strojniški vestnik - Journal of Mechanical Engineering*, vol. 66, no. 1, p. 61-70, **DOI:10.5545/sv-jme.2019.6156**.

[36] Cui, D., Wang, G., Zhao, H., Wang, S. (2020). Research on a path-tracking control system for articulated tracked vehicles. *Strojniški vestnik - Journal of Mechanical Engineering*, vol. 66, no. 5, p. 311-324, **DOI:10.5545/sv-jme.2019.6463**.

[37] Taghavipour, A., Alipour, A. (2021). HIL evaluation of a novel real-time energy management system for an HEV with a continuously variable transmission. *Strojniški vestnik - Journal of Mechanical Engineering*, vol. 67, no. 4, 142-152, **DOI:10.5545/sv-jme.2020.7017**.

[38] Liu, Y., Li, Y., Zhang, X., Chen, B. (2021). Trajectory-tracking control for manipulators based on fuzzy equivalence and a terminal sliding mode. *Strojniški vestnik - Journal of Mechanical Engineering*, vol. 67, no. 9, p. 433-444, **DOI:10.5545/sv-jme.2021.7220**.

Strojniški vestnik - Journal of Mechanical Engineering 68(2022)11, 693-701
DOI:10.5545/sv-jme.2022.344
Original Scientific Paper
Received for review: 2022-08-25
Received revised form: 2022-11-02
Accepted for publication: 2022-11-07

Effect of Tool Geometry in Stir Zone for Hook Formation of Dissimilar Aluminium Alloys: A Parametric Investigation on Metallurgical and Mechanical Characteristics

Nandakumar Navaneethakannan* – Periyasamy Sivanandi – Balakrishnan Somasekaran
Government College of Technology, Department of Mechanical Engineering, India

A recently developed solid-state joining technique called "friction stir spot welding" (FSSW) is used to combine metal alloys with low weldability. Significant experimental work for this study is concentrated on the FSSW of AA6063 and AA5083. The study involved fixture setup and welding pattern parameters for the sizes of the material, all of which were done on a milling machine. A cylindrical shoulder with a concave (10°) square pin profile was taken into consideration using various process parameters. The tool material is heat-treated high-carbon steel. The Taguchi L9 orthogonal array is employed for the experimental model. The influence of FSSW factors including spindle speed, time, and depth was studied, along with the relationship between tensile strength, hardness at the contact region, and hook development, which would be a nominal metallurgical pledge established in the welding zone among the interacting sheet plate. The hook structure was found in the area of contact, and thermomechanical effects were seen in the spot-welding area. It has been determined that the influencing variables are spindle speed and plunge depth. As a consequence, it was determined that a tool spindle speed of 1200 rpm, a time of 25 seconds, and a plunge depth of 0.10 mm offer better mechanical properties. The microstructural analysis of welded region was carried out using a scanning electron microscope (SEM).

Keywords: microstructure, hook geometry, stir zone, multiple regression, ANOVA

Highlights

- *FSSW operating parameters, including the spindle speed, time, and depth of penetration, were considered.*
- *The mechanical properties, such as tensile strength and hardness of the FSSW-welded region, were obtained.*
- *The formation of the hook structure was observed during the FSSW process using SEM.*
- *Percentages of the contribution of each process parameter were obtained based on the ANOVA results.*

0 INTRODUCTION

The most important factor in the current automobile sector is fuel efficiency, and losing weight is one of the simplest ways to reduce fuel usage. Lighter components such as aluminium and magnesium alloys are helping to improve fuel efficiency. In contrast, flame-curable Al alloys require more complicated fusion welding techniques. As a result, TWI's friction stir spot welding (FSSW) has drawn much interest since it offers a variety of advantages, including minor welding faults, relatively low stresses, an electrodeless weld, weight reduction, and the ability to use less power. Recent years have seen an increase in the utilization of aluminium body welds for FSSW.

Al 6082-T6 sandwich plates' mechanical performance during FSSW was examined using a square pin instrument by Ravi, et al. **[1]**. Sandwich plates can be attached using a squared pattern tool that has a solid pin and plain joint, as well as a tool with a curved shoulder, although at the price of joint output. Siddhartha and Senthilkumar **[2]** studied FSSW apertures in order to produce Al 5086 boards of equal quality. ANOVA analysis has been utilized to confirm the applicability of the established model at a response rate of more than 95 %. Rana et al. **[3]** investigated the mechanical properties, hook structure, particle shape, toughness, and heat radiation of aluminium plates. The hook size widens and the hook length lengthens with increased spindle speed. The hook topologies are defined by the heat generated, and the device's rotating speed affects the quantity of energy generated. This length of plunge demonstrates a change in product blending at the link surface and is inversely proportional to the ultimate tensile fatigue strength.

Research by Garg and Bhattacharya **[4]** examines how spindle speed, longer waiting times, and different pin profile configurations affect the lap strength qualities of welding effectiveness. However, employing the rectangular shape pattern results in an increased elastic modulus, which significantly increases stress in the base materials. The lap-shear fracture load increases as welding limitations are raised up to a certain degree and then decreases as welding constraints are raised further, according to Tashkandi et al. **[5]**. The load for lap-shear fracture increased if the spindle speed was increased to 1120

*Corr. Author's Address: Government College of Technology, Department of Mechanical Engineering, India, nandakumar@gct.ac.in

rpm. Shubhavardhan and Rahman [6] investigated the hook structure and fracture power of Al6060-T5/ Al6060-T5. As the tool spindle speed increased from 500 rpm to 1000 rpm, a rise in contact region especially increased hooked length. Hook length remained constant as spindle speed increased from 1000 rev/min to 2000 rev/min. Satheesh et al. [7] investigated the various friction stir welding input process parameters, such as traverse speed, tool rotational speed, axial force and pin profile using response surface methodology and found the optimal process parameters which exhibited improvement in mechanical properties.

Cao et al. [8] investigated the relationship between the shape of the hook and the hooks' maximum tensile strength as well as the direction of the hook effect in relation to plunge height. Increases in spindle speed, join duration, or plunge distance resulted in longer hooks and inefficient welding. According to Piccini and Svoboda [9], effective binding increases the chance when welding with small pin instruments and improves device propagation distance. In this regard, the decrease in the distance between the attachment and the low position of the shoulder has shown an improvement in the thermo-mechanical impact of the welding device. According to Piccini and Svoboda [10], the thermo-mechanical impact of the workpiece is primarily related to the thickest low distance between the controller and the shoulder layer. When the equipment depth is raised for lap welding, the Al 6063 (top) / Al5052 (bottom) configuration performs fairly well.

The primary objective of the research is to investigate the weld performance of the aluminium alloys 6063-T6 and 5083-O-H111 in terms of ultimate tensile toughness, stiffness, and hook shape under different processing conditions. The predicted values of tensile shear stress, stiffness, and hook shape are determined using regression analytical techniques. ANOVA is used to evaluate the impact of various features and effects on the outcome, and Taguchi's approach is used to determine the appropriate test parameter.

1 MATERIALS AND METHOD

1.1 Selection of Material

The marine-grade aluminium alloys used in this work are AA6063-T6 and AA5083-O-H111. Compared to other aluminium alloys, it is the most corrosion-resistant. The matrix-consistent deposition of a subsequent phase strengthens the thermal metal AA6063-T6. According to T6, the metal must be heated to a certain temperature before being extruded for corrosion resistance. Table 1 displays AA 6063's chemical composition. Another alloy employed in the research is AA5083-O-H111, in which the O symbol denotes total softness and the updated diagnosis ranges from 345 °C to 650 °C, with subsequent cooling to such an uncontrolled back level. The last number and the second digit, which is defined as 1/8, are typically utilised on rotational forms that need to be streamlined after welding to meet stiffness requirements. The strain toughened without treatment, as seen in H111. Table 2 contains a summary of Al5083-O-chemical H1's composition.

Table 1. *Chemical content of AA 6063*

Elements	Mg	Fe	Si	Si	Zn	Ti	Cr	Cu	Al
%	0.45	0.35	0.2	0.2	0.1	0.1	0.1	0.1	rest

Table 2. *Chemical content of AA 5083*

Elements	Mg	Mn	Fe	Si	Cr	Zn	Ti	Cu	Al
%	4.9	1	0.4	0.4	0.25	0.25	0.15	0.1	rest

1.2 Experimental Design

Significant influencing parameters in FSSW were discovered to be spindle speed, dwell time, and plunge depth. Therefore, it is necessary to investigate the ideal settings for productive joint processing. The pin wears out very quickly due to a lower spindle speed that results in an insufficient rise in heat at the weld. The dwell period is determined by the heat transfer into the samples. Axial force is caused by the depth of the drop on the top and bottom sheets [11]. When analysing the effects of multiple parameters simultaneously, Taguchi optimization techniques are efficient and simple to utilize. This approach is ideally suited to the use of a mean output characteristic quality that is close to the goal level rather than a rating that is subject to those calculation restrictions. The efficiency and quality of the materials will therefore increase. Numerous samples must be taken even as the number of input variables increases. The samples were converted to the initial number of experiment samples using a special orthogonal array structure. A signal-to-noise ratio, an evaluation of the desired valuation standard's capabilities, was created from the modified valuation data. Three input parameters and three levels were used in this investigation's design, and the operational parameters are displayed in Table 3.

Table 3. *Welding operating parameters and their levels*

Parameters	Unit	Level 1	Level 2	Level 3
Spindle speed (N)	rpm	1000	1100	1200
Dwell time (t)	s	20	25	30
Plunge depth (D)	mm	0.10	0.15	0.20

1.3 Experimental Details

The studies were carried out on a semi-automated vertical milling machine with such a tool mounted on an axle with a suitable collet and samples set up in a fixture and weld template. The vertical tool head could be pushed along the horizontal Z-axis while the longitudinal bed could be moved along the X- and Y-axes. The investigation used 3 mm thick plates of the aluminium alloys that were chosen (AA6063-T6 and AA5083-O-H111). The welding surfaces of the trial plates are mounded in the longitudinal bed to the smallest origin gaps connected to the centreline of the FSSW tool with the aid of a specially made fixture [12]. The backing plate and template need to be firmly fastened together. The experimental setup for clamping the FSSW plate is shown in Fig. 1. The spot-welded section's dimensions are plotted in a figure as illustrated in Fig. 2.

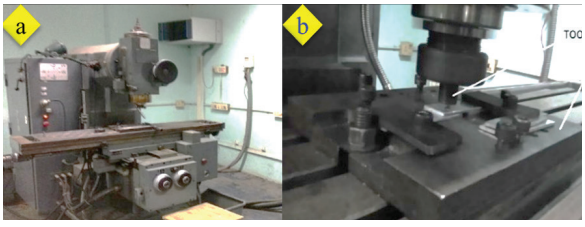

Fig. 1. *a) Semi-automated vertical milling machine, b) specimen fixture*

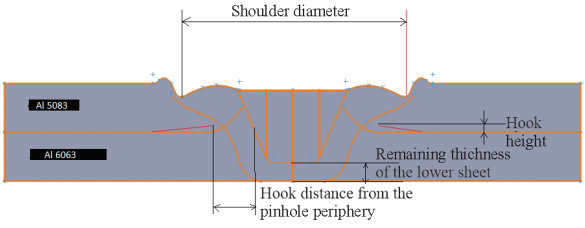

Fig. 2. *Schematic plot of the dimensions measured on the spot welded section*

1.4 Testing of Mechanical Properties

Samples prepared in accordance with ASTM-E8M requirements underwent tensile shear strength tests. The typical welding sample dimensions for shear strength testing are shown in Fig. 3. The computerized UTM 100 is used to estimate the TSS of the weld region. The FSSW of the AA6063 and AA5083 specimens used for TSS testing is shown in Fig. 4. A Vickers hardness measurement apparatus with a load of 5 kg is utilized for the hardness test. A diamond indenter is used to measure the hardness horizontally and perpendicular to the welding keyhole of 90-degree deviations around component attributes. Later, micrographic analysis was carried out at the touch region using optical techniques to determine the hooked distance and width from the pinhole boundary. Fig. 5 displays the FSSW of AA6063 and AA5083 samples for hardness analysis examination.

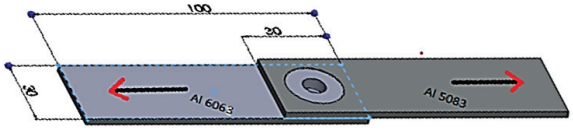

Fig. 3. *Standard dimension for tensile shear test, all dimensions are in mm, ASTM E8M*

Fig. 4. *Tensile test welded specimens*

Fig. 5. *Hardness test welded specimens*

1.5 Microstructure Examination

The base metal and fuse field were compromised during the metallurgical categorization on the welded sample, utilizing an optical inverted microscope. The conventional microstructure method has been applied to prepare the sample for the test. The binding region significantly affects the weld zone's weight behaviour competence, particularly during shear strength testing. If the bonding region were wider, the breaking load would be higher. Hook morphology also determines how tough a joint is. Both the hook height and the distance can be used to depict it. A weaker joint result from hook insertion in the pinhole direction; conversely, a stronger joint follows from hook placement in the opposite direction. The joint's

stability would increase with the size of the gap between the hooks and the pinhole boundary. At the same time, welding becomes weaker as hook size and length increase.

2 RESULTS AND DISCUSSION

2.1 Results of Mechanical Properties

The welded samples underwent a tensile test. To ascertain the tensile strength of the weld samples, they are loaded into the apparatus and subjected to a tensile load. Fig. 6 shows the topmost and bottommost portions of the weld zone after a maximum force has been applied to fracture it. Fig. 7 displays the bottom section of a weld sample following the tensile test. It has been noted that this zone's nugget zone area is larger than others' and that it has a sizable TMAZ area and HAZ area, both of which contribute to the generation of more frictional heat between the tool and the materials.

Fig. 6. *Welded specimen a) Al 6061 top view, and b) AL 5058 bottom view*

Table 4 shows the TSS for the samples obtained during the tests, with the sample from experiment 9 (1200 rpm, 30 s, 0.15 mm) with the highest TSS and the sample from experiment 1 with the lowest TSS (1000 rpm, 20 s, 0.10 mm). Fig. 8 demonstrates that experiment 9's tensile strength is higher than that of the other experiments. The experimental circumstances specimen had the lowest hardness of 81.74 at 1000 rpm, 25 s, and 0.15 mm, while the specimen from study 7 had the highest hardness at 1200 rpm, 20 s, and 0.20 mm). Fig. 8 shows the FSSW joints' tensile shear and Vickers hardness values.

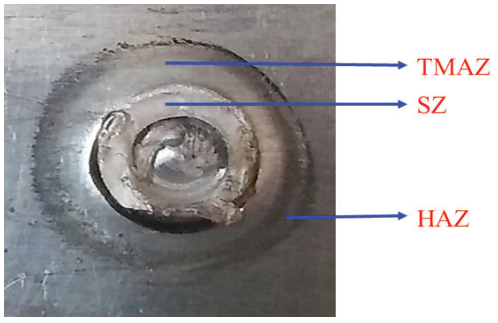

Fig. 7. *The bottom section of a weld (after tensile test)*

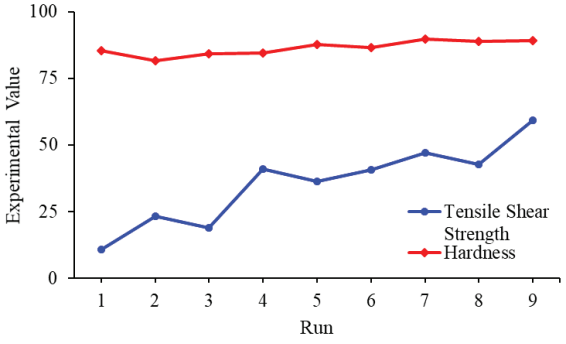

Fig. 8. *Experimental values of mechanical properties*

2.2 Results of Microstructure Study

The results of a microstructural analysis show that there are essentially three different sorts of regions

Table 4. *Experiment results with signal to noise (S/N) ratio for mechanical properties*

Run	Input parameters			Experimental results		S/N ratio	
	Spindle speed	Dwell time	Plunge depth	Tensile shear strength	Hardness	Tensile shear strength	Hardness
1	1000	20	0.1	10.9	85.33	20.7485	38.622
2	1000	25	0.15	23.3	81.74	27.3471	38.2487
3	1000	30	0.2	18.9	84.25	25.5292	38.5114
4	1100	20	0.15	40.9	84.5	32.2345	38.5371
5	1100	25	0.2	36.2	87.75	31.1742	38.8649
6	1100	30	0.1	40.6	86.5	32.1705	38.7403
7	1200	20	0.2	47	89.75	33.4420	39.0607
8	1200	25	0.1	42.6	89	32.5882	38.9878
9	1200	30	0.15	59.2	89.25	35.4464	39.0122

that occur during welding: the stir zone (SZ), the thermal mechanically affected zone (TMAZ), and the heat affected zone (HAZ), which are classified from the section's centre to its superiority. Fig. 9 shows that for the sample of experiments run at a spindle speed of 1200 rpm, dwell time of 30 s, and depth of 0.15 mm, the maximum hook height was 0.673 mm, and the smallest hook height was 0.239 mm for the specimen of experiments run at a spindle speed of 1200 rpm, dwell time of 25 s, and depth of 0.10 mm. The distance from the pinhole perimeter varies on the procedure parameters, as shown in Fig. 10. Table 5 shows that the greatest hook height was 0.673 mm for the welded specimen of trial 9 (1200 rpm, 30 s, 0.15 mm), while the minimum hook height was 0.239 mm for the specimen of experiment 8. Hook height and distance of the TSS discovered in microstructure analysis (1200 rpm, 25 s, 0.10 mm). that the sample

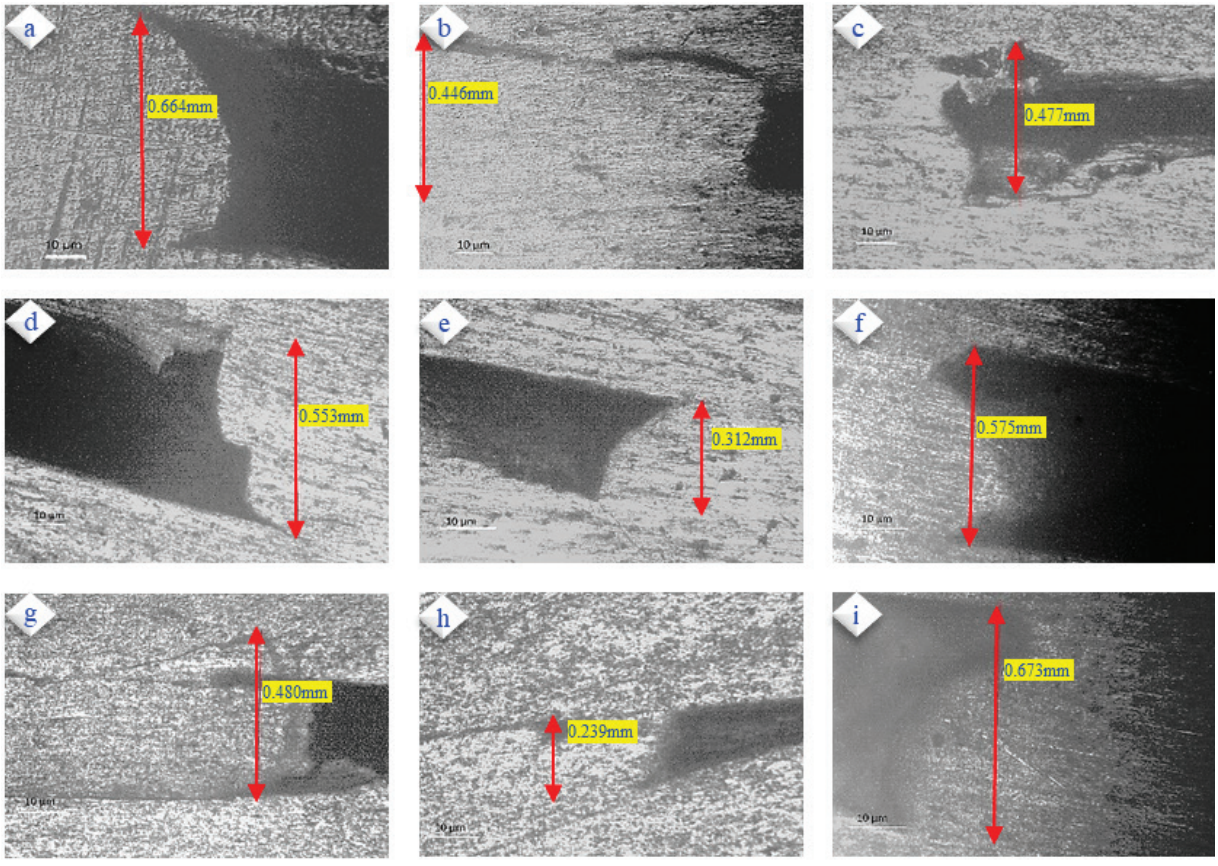

Fig. 9. *Microstructure examination of hook height*

Table 5. *Experimental results with snr for response variable*

Run	Spindle speed	Dwell time	Plunge Depth	Hook geometry		S/N ratio	
				Height	Distance	Height	Distance
1	1000	20	0.10	0.664	1.974	3.5566	5.90694
2	1000	25	0.15	0.446	1.824	7.0133	5.22050
3	1000	30	0.20	0.477	1.851	6.4296	5.34813
4	1100	20	0.15	0.553	1.210	5.1455	1.65571
5	1100	25	0.20	0.312	1.916	10.1169	5.64791
6	1100	30	0.10	0.575	1.934	4.8066	5.72913
7	1200	20	0.20	0.480	1.864	6.3752	5.40892
8	1200	25	0.10	0.239	2.061	12.4320	6.28156
9	1200	30	0.15	0.673	2.246	3.4397	7.02820

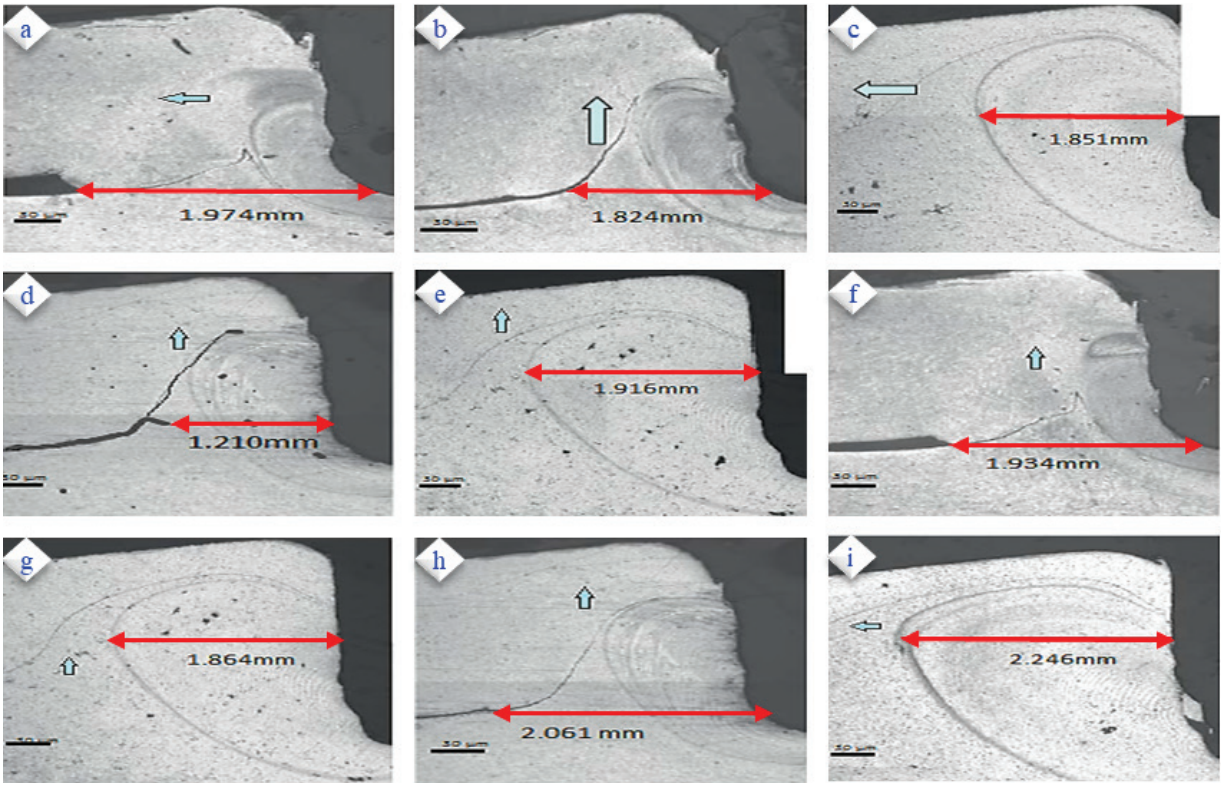

Fig. 10. *Distance from the pinhole periphery*

from experiment 9 (1200 rpm, 30 s, 0.15 mm) had the greatest hook distance from the peripheral while the welded specimen from trial 2 had the smallest hook distance, measuring 1.824 mm (1000 rpm, 25 s, 0.15 mm).

2.3 Main Effect Plot of SN Ratio

The FSSW variables are standardized throughout this research; therefore, TSS and hardness are appropriate characteristics for identifying dependents. The "Larger is Better" design was applied during the S/N ratio evaluation because the highest possible tensile shear strength and hardness are required. Table 4 shows the S/N ratios of the welded joints made from Al 6063 and Al 5083 based on the results of the testing. The highest S/N ratio in Fig. 11 indicates that the welding input settings are very effective. The ideal spindle speed is 1200 rpm since the TSS S/N ratio increases continuously from 1000 rpm to 1100 rpm and then from 1100 rpm to 1200 rpm, as illustrated in Fig. 11a. In line with this, the S/N ratio of dwell time increases from 20 s to 25 s, then progressively increases from 25 s to 30 s, with 30 s being the maximum dwell duration. A 0.20 mm ideal plunge depth is reached when the S/N ratio of the number of plunge depths improves from 0.10 mm to 0.15 mm, then increases from 0.15 mm to 0.20 mm. This analysis shows that the maximum TSS recorded from the welding situation is 1200 rpm, 30 s, and 0.15 mm. Fig. 11b shows the hardness plot with the largest influence on the S/N ratio chart. The above-mentioned method to calculate the hardness value: 1200 rpm, 20 s, and 0.20 mm, was used to estimate the maximum hardness attained under the welding conditions. The "Smaller is Better" formula was employed in the study utilizing the S/N ratio because hook height is one of the methodological flaws for the stir region. The S/N ratio of the connections leading to trials for the AA6061 and AA7075 is shown in Table 5. Fig. 12 displays the principal effect chart, which focuses mainly on the SN ratio. The optimal spindle speed is 1200 rpm, which has the maximum value, as the S/N ratio increases from 1000 rpm to 1200 rpm, as shown in Fig. 12a. Accordingly, the dwell time S/N ratio increases from 20 s to 25 s before falling from 25 s to 30 s, proving that 25 s is the ideal dwell time. Indicating that 0.20 mm is the maximum plunge depth, the S/N ratio of plunge depth then decreases from 0.10 mm to 0.15 mm, then increases from 0.15 mm to 0.20 mm above

the 0.10 threshold. Similar techniques are used to evaluate the hook distance S/N ratio diagrams, and it can be deduced from Fig. 12b that the maximum hook distance that can be obtained from a variable is 1200 rpm, 30 s, and 0.10 mm.

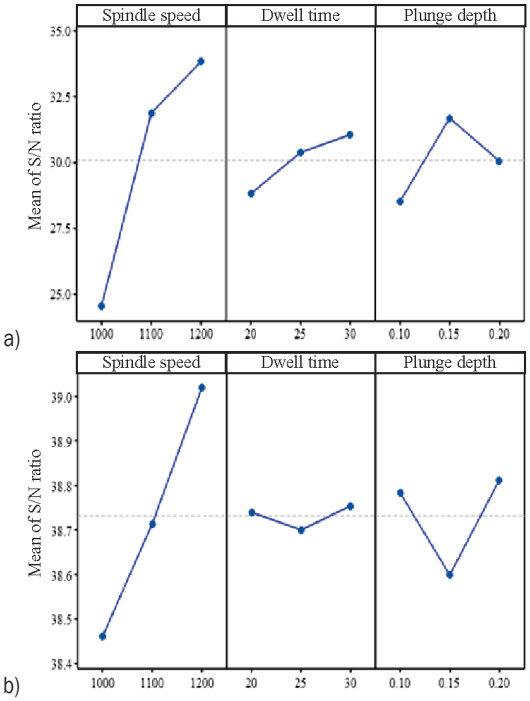

Fig. 11. *Main effect plot for S/N ratio a) TSS, b) hardness*

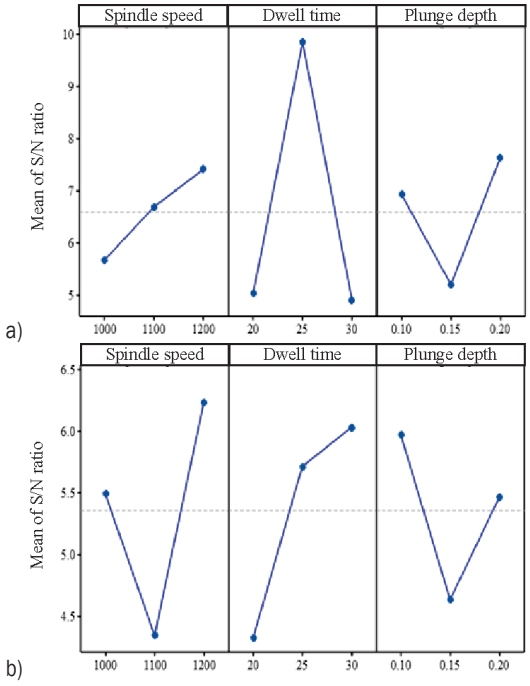

Fig. 12. *Main Effect plot for SN ratio Hook a) height, b) distance*

2.4 Analysis of Variance

ANOVA has been used to compare the effects of different welding operation conditions on TSS and hardness. To assess the severity of various operating circumstances, the ANOVA is used. The P-value displays the percentage of unexpected quantities that are classified as sound, and Tables 6 to 9 display the optimal values of customizable operational parameters to maximize hardness. The highest F value and lowest P value are therefore preferred, and any variable with a probability of less than 5 % is taken to be a significant characteristic. From Table 6, it can be inferred that the variable has a statistically significant F value of 131.64. From Table 7, it can be inferred that the variable has a statistically significant F value of 23.277.

Table 6. *ANOVA for TSS*

Source	DF	Seq SS	Adj SS	AdjMS	F	P
Spindle speed	2	1588.76	1588.76	794.38	131.64	1.008
Dwell time	2	75.83	75.83	37.91	6.28	0.137
Plunge depth	2	152.91	152.91	76.45	12.67	0.073
Error	2	12.07	12.07	6.03		
Total	8	1829.57				

Table 7. *ANOVA for hardness*

Source	DF	Seq SS	Adj SS	AdjMS	F	P
Spindle speed	2	46.554	46.554	23.277	10.51	0.087
Dwell time	2	0.405	0.405	0.202	0.09	0.916
Plunge depth	2	7.617	7.617	3.808	1.72	0.368
Error	2	4.430	4.430	2.215		
Total	8	59.006				

Table 8. *ANOVA for Hook height*

Source	DF	Seq SS	Adj SS	AdjMS	F	P
Spindle speed	2	0.00688	0.00688	0.00344	0.28	0.780
Dwell time	2	0.11342	0.11342	0.05671	4.64	0.177
Plunge depth	2	0.02708	0.02708	0.01354	1.11	0.475
Error	2	0.02446	0.02446	0.01223		
Total	8	0.17184				

When welding dissimilar aluminium alloys with FSSW, the F-test is utilized to determine the key operating element that impacts hook height and length. The F value of 0.28 and 1.20 in Tables 8 and 9 respectively represent the mean value of some well-operating conditions to reach minimum hook height, while the 'P' value offers the potential for disproportionate inputs. A maximum F value and an average P value are therefore needed. Similarly, dwell duration corresponds with the highest hook distance

by 27.85 %, whereas spindle speed connects with the greatest hook distance by 12.51 %.

Table 9. *ANOVA for Hook length*

Source	DF	Seq SS	Adj SS	AdjMS	F	P
Spindle speed	2	0.20597	0.20597	0.10298	1.20	0.454
Dwell time	2	0.17624	0.17624	0.08812	1.03	0.493
Plunge depth	2	0.07924	0.07924	0.03956	0.46	0.684
Error	2	0.17138	0.17138	0.08569		
Total	8	0.63272				

2.5 Effect of Contribution of Operating Parameters

Calculating the percentage contribution of operating parameters involves comparing the sum of the squares of variation to the sum of the squares of variation. The percentage contribution of each shear strength and hardness parameter is shown in Fig. 13. Fig. 13a shows that the spindle speed makes up 86.3 % of the total contribution, with dwell time making up 4.14 % and dive depth accounting for 8.35 %. Fig. 13b shows that the spindle speed contributes 78.89 % of the total, followed by dwell time with 0.68 % and dive depth with 12.92 %. The TSS and hardness of the specimen are shown to be significantly influenced by spindle speed, a key process parameter. The percentage influence of each parameter on hook height and distance is depicted in Fig. 14's chart.

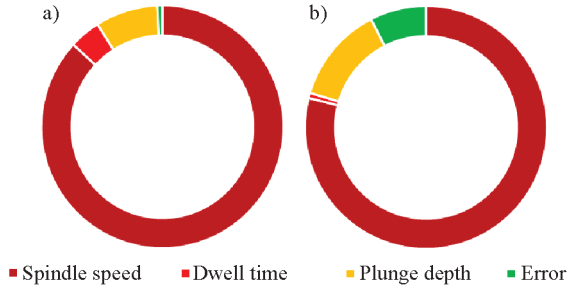

Fig. 13. *Contribution % of process parameters, a) tensile shear stress, and b) hardness*

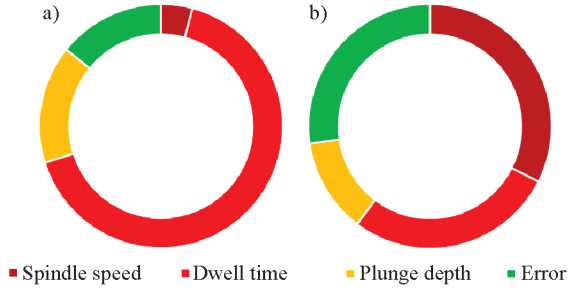

Fig. 14. *Contribution % of process parameters; a) hook height b) hook distance*

Fig. 14a shows that the spindle speed makes up 86.3 % of the total contribution, with dwell time making up 4.14 % and plunge depth making up 8.35 %. Thus, it is obvious that dwell time plays the largest role in achieving the lowest hook height. Accordingly, in FSSW, spindle speed is the most important parameter to manage the welding process's distinctive property hook height. Fig. 14b shows that the spindle speed makes up 32.55 % of the contribution, followed by dwell duration at 27.85 % and dive depth at 12.51 %. The main hook distance is shown to be influenced by spindle speed.

2.6 Multiple Regression Equations

The findings of the experiments determine the correlation coefficient between the friction spot welding operating settings and the efficiency measures. significance at a 95 % confidence level to conduct the experiment. Eqs. (1) to (4) explain the regression equations for the following variables: tensile shear strength (*TSS*), Vickers hardness (*HV*), hook height (*H*), hook distance (*L*) from the welding operating condition, spindle speed (*N*), length of dwell (*t*), and depth of plunge (*d*).

$$TSS = -161 + 0.159N + 26.7d + 0.663t, \quad (1)$$

$$HV = 55.1 + 0.0278N + 3.1d + 0.014t, \quad (2)$$

$$H = 0.930 - 0.000325N - 0.70d + 0.0009t, \quad (3)$$

$$L = 0.27 + 0.00087N - 1.13d + 0.0328t. \quad (4)$$

3 CONCLUSIONS

A successful parametric investigation on the mechanical and metallurgical properties of welded dissimilar aluminium alloys and their impact on tool geometry in the stir zone for hook production has been carried out. An overview of the research's findings is provided below.

- Spindle speed is found to be a key operating factor influencing welding strength for the Al6063-T6 and Al5083-O-H111 plates. Spindle speed (N = 86.83 %) has the biggest impact on specimen tensile strength, followed by plunge depth (D = 8.35%) and dwell time (t = 4.14%). The specimen's tensile strength varies depending on where the weld connection is strongest. The ideal parameters for high tensile strength, according to Taguchi research, are 1200 rpm, 30 s dwell duration, and 0.15 mm plunge depth.

- The most important factor influencing the hardness control is dwell time. The other factors that affect hardness are spindle speed and plunge depth, in that order of significance. The results of this investigation show that the dwell time (t = 66.00 %), plunge depth (D = 15.74 %), and spindle speed (N = 4.00 %) have the biggest effects on the hardness of the sample. The strength of the joint is inversely correlated with its hardness.
- According to the metallurgical examination, the minimum hook height will be formed by welding operating conditions such as spindle speed of 1000 rpm, dwell time of 25 s, and depth of 0.20 mm, with parameters contributing N = 4.2 %, t = 66.23 %, and D = 15.75 %, and the mean hook width will be formed by welding conditions such as 2000 rpm, 3 s, and 0.10 mm, with parameters contributing N = 32.55 %, t = 27.

4 ACKNOWLEDGEMENTS

The authors thank the Government College of Technology, Coimbatore, Tamilnadu, India, which gave full support in conducting the experimental research work in this paper.

5 REFERENCES

[1] Ravi, K.K., Narayanan, R.G., Rana, P.K. (2019). Friction Stir Spot Welding of Al6082-T6/HDPE/Al6082-T6/HDPE/Al6082-T6 sandwich sheets: Hook formation and lap shear test performance. *Journal of Materials Science & Technology*, vol. 8, no. 1, p. 615-622, **DOI:10.1016/j.jmrt.2018.05.011**.

[2] Siddhartha, S., Senthilkumar, T. (2018) Development of friction stir spot welding windows for dissimilar Al5086/C10100 spot joints. *Materials Today Proceedings*, vol. 5, no. 2, p. 6550-6559, **DOI:10.1016/j.matpr.2017.11.310**.

[3] Rana, P.K., Narayanan, R.G., Kailas, S.V. (2018) Effect of rotational speed on friction stir spot welding of AA5052-H32/HDPE/AA5052-H32 sandwich sheets. *Journal of Material Processing Technology*, vol. 252, p. 511-523, **DOI:10.1016/j.jmatprotec.2017.10.016**.

[4] Garg, A., Bhattacharya, A. (2017). Strength and failure analysis of similar and dissimilar friction stir spot welds: Influence of different tools and pin geometries. *Materials and Design*, vol. 127, p. 272-286, **DOI:10.1016/j.matdes.2017.04.084**.

[5] Tashkandi, M.A., Al-jarrah, J., Ibrahim, M. (2017). Spot welding of 6061 aluminum alloy by friction stir spot welding process. *Engineering Technology & Applied Science Research*, vol. 7, no. 3, p. 1629-1632, **DOI:10.48084/etasr.1125**.

[6] Shubhavardhan, R.N., Rahman, M.M. (2017). Effect of FSW parameters on Hook formation, microstructure and fracture strength of Al, Mg alloys. *International Journal of Engineering Development and Research*, vol. 5, no. 2, p. 1730-1736.

[7] Satheesh, C., Sevvel, P., Senthil Kumar, R. (2020) Experimental identification of optimized process parameters for FSW of AZ91C Mg alloy using quadratic regression models. *Strojniški vestnik - Journal of Mechanical Engineering*, vol. 66, no. 12, p. 736-751, **DOI:10.5545/sv-jme.2020.6929**.

[8] Cao, J.Y., Wang, M., Kong, L., Guo, L.J. (2016). Hook formation and mechanical properties of friction spot welding in alloy 6061-T6. *Journal of Materials Processing Technology*, vol. 230, p. 254-262, **DOI:10.1016/j.jmatprotec.2015.11.026**.

[9] Piccini, J.M., Svoboda, H.G. (2015). Effect of the tool penetration depth in friction stir spot welding (FSSW) of dissimilar aluminum alloys. *Procedia Materials Science*, vol. 8, p. 868-877, **DOI:10.1016/j.mspro.2015.04.147**.

[10] Piccini, J.M., Svoboda, H.G. (2017). Tool geometry optimization in friction stir spot welding of Al-steel joints. *Journal of Manufacturing Processes*, vol. 26, p. 142-154, **DOI:10.1016/j.jmapro.2017.02.004**.

[11] Van, A.-L., Nguyen, T.-T. (2022). Optimization of friction stir welding operation using optimal taguchi-based ANFIS and genetic algorithm. *Strojniški vestnik - Journal of Mechanical Engineering*, vol. 68, no. 6, p. 424-438, **DOI:10.5545/sv-jme.2022.111**.

[12] Badarinarayan, H., Shi, Y., Li, X., Okamoto, K. (2009). Effect of tool geometry on hook formation and static strength of friction stir spot welded aluminum 5754-0 sheets. *International Journal of Machine Tool Manufacture*, vol. 49, no. 11, p. 814-823, **DOI:10.1016/j.ijmachtools.2009.06.001**.

Strojniški vestnik - Journal of Mechanical Engineering 68(2022)11, 702-712
DOI:10.5545/sv-jme.2022.332
Original Scientific Paper
Received for review: 2022-06-06
Received revised form: 2022-08-18
Accepted for publication: 2022-08-18

Experimental Research on Transmission Characteristics of Elliptic Gear Transmission Systems

Changbin Dong[1] – Wangpeng Pei[1] – Yongping Liu[1] – Yongqiao Wei*[,1,2] – Dawei Li[1] – Rui Guo[1] – Zhongtao Ren[1]

[1] Lanzhou University of Technology, School of Mechanical and Electrical Engineering, China
[2] State Key Laboratory of High-Performance Complex Manufacturing, Central South University, China

The special variable ratio transmission characteristics and complex tooth profile curve of elliptic gears make it difficult to analyse their transmission characteristics, which restrict the application and development of elliptical gears. Given that, a transmission characteristic analysis method based on transmission testing is proposed in this paper. By building a high-precision elliptic gear test rig, the distribution laws of dynamic lost motion, static lost motion, back clearance, stiffness, friction torque and vibration with speeds and loads are analysed and obtained. The results show that the dynamic lost motion and friction torque will increase with the increase of rotating speed. The dynamic lost motion, static lost motion and back clearance will gradually decrease with the increase of load, and the stiffness will gradually increase. Enlarging the load and reducing the speed can restrain the vibration amplitude, which can ensure the transition of the gear system from a bilateral collision state to a unilateral collision state and thus improve the stability of the system.

Keywords: elliptic gears, transmission test, hysteresis characteristic, friction torque, vibration

Highlights

- *A transmission test rig suitable for elliptic gear transmission with a variable ratio is built.*
- *An analytical method for analysing the dynamic transmission characteristics of elliptic gears using transmission experiments is proposed.*
- *The hysteresis characteristic, dynamic lost motion, static lost motion, friction torque, and vibration characteristics of an elliptic gear transmission system are obtained via transmission experiments.*

0 INTRODUCTION

Elliptic gears break the fixed ratio transmission mode of cylindrical gear and differ from each other because their pitch curves are different from cylindrical gears [1]. An elliptic gear is suitable for low-speed and high-torque occasions, such as the printing press, packaging machines, pumping units, gear pumps, the weft insertion mechanisms of textile equipment, the frequency conversion vibrators of spacecraft and missile ground combat equipment, the ranging device of tank control systems, etc. [2]. With the increasing application of elliptic gears in precision transmission, the dynamic performance cannot meet the application requirements at this stage, which restricts its application to precision situations. Transmission testing is an effective method to analyse the transmission performance of gear systems. Through the experimental analysis of the transmission characteristics of elliptic gears, transmission performance can be significantly improved and its application expanded [3].

At present, the research on the performance of elliptic gears basically focuses on theoretical analysis and dynamic characteristic analysis, and there are few studies on the transmission test. Liu et al. [4] and [5] studied the vibration characteristics of elliptic gears. After analysing the instantaneous coincidence degree of elliptic gears, the effects of torque, speed, vibration acceleration, and speed on the dynamic response are obtained. Gao et al. [6] aimed at the vibration and instability of elliptic gear and established the torsional dynamic model based on the lumped parameter method, and analysed the influence of eccentricity, torque, external excitation, and torque on the vibration instability of elliptic gear system. Karpov et al. [7] studied the usability of non-circular gears (NCG) to prevent resonance oscillation in gear systems and analysed the influence of gear centre distance deviation on motion and vibration characteristics. The results show that due to the change in meshing frequency, the greater the eccentricity, the smaller the resonance amplitude and the greater the additional dynamic load. Lin et al. [8] and Cai and Lin [9] established a nonlinear dynamic model of meshing between orthogonal curved surface gear and NCG, and the influence of different meshing frequencies and tooth clearances on the dynamic response was obtained by solving the mathematical model. Liu et al. [10] to [13] studied the nonlinear characteristics of NCG and proposed that the transmission ratio curve of NCG can be linearly divided by using the idea of a micro-element method, which is used to solve the problem that it is difficult to characterize the time

*Corr. Author's Address: Lanzhou University of Technology, Gansu Lanzhou, 730050, China, scuwyq@163.com

variability of pitch curve in the establishment of a nonlinear dynamic model of NCG.

Supported by the research and analysis methods of the dynamic meshing characteristics of cylindrical gears, some scholars have studied the dynamic meshing characteristics of elliptic gears. Because kinematic analysis is usually the basis of meshing characteristics analysis, most of the research is focused on kinematics. Liu et al. [14] obtained the dynamic transmission characteristics and the distribution law of tooth root bending stress through theoretical calculation and experimental analysis of elliptic gear. Vasie and Andrei [15] proposed the generation method of elliptic gear pitch curve and tooth profile and simulated and analysed the meshing path, contact area, and its changes of gear teeth in 2D and 3D environments, respectively. Focusing on NCG transmission systems, Han et al. [16] proposed a helical NCG transmission mechanism to decrease the meshing impact and realize the backlash adjustment for stability and accuracy. The meshing backlash is analysed with a physical contact simulation method, and the influence of axial displacement adjustment on the meshing backlash of a gear pair is obtained. Based on the analysis of the structure form and transmission principle of elliptic gear transmission system, Lin et al. [17] and [18] carried out relevant research on the contact area of tooth surfaces and analysed the distribution relationship between the contact points and contact area of the tooth surface with the position of the teeth. Dooner and Mundo [19] analysed the no-load transmission error and instantaneous transmission ratio of eccentric NCG and put forward the calculation method for no-load transmission error. On this basis, the variation trend of no-load transmission error and instantaneous transmission ratio of generalized misalignment is predicted. Dong et al. [1] introduced installation error, manufacturing error, and other factors into the dynamic transmission error model of elliptic gears and analysed the influence of eccentricity on transmission pressure angle, instantaneous coincidence degree, and transmission error. Finally, the correctness of the analysis is verified with the finite element method.

It can be seen that most of the research only makes a basic analysis of the dynamic characteristics of elliptic gears and puts forward relevant analysis methods and analysis theories, which play an irreplaceable role in the analysis of the dynamic transmission characteristics of elliptic gears. However, there are some differences between each tooth of the elliptic gear. Most of the above studies are for a single tooth, and there are almost no test results and research methods related to the transmission characteristics of elliptic gears. Therefore, the proposed analysis method has certain limitations. Given that, the paper proposes and builds an elliptic gear test rig to analyse the dynamic transmission characteristics, which can lay a foundation for broadening the industrial application of elliptic gears.

1 CONSTRUCTION OF ELLIPTIC GEAR TRANSMISSION TEST RIG

Experimental analysis is an important part of scientific research. It is an effective way to obtain the motion characteristics of the system and verify the analysis results. The variable speed transmission action accomplished with an elliptic gear is a new type of gear transmission mode. At present, it remains in the primary stage, and there is no mature theory or method to provide reference and guidance. Therefore, the relevant transmission test analysis of elliptic gear is of great significance for guiding the subsequent design and engineering application of elliptic gears. The data obtained through the test analysis can accurately reflect the correctness of the theoretical research on the transmission principle, geometric

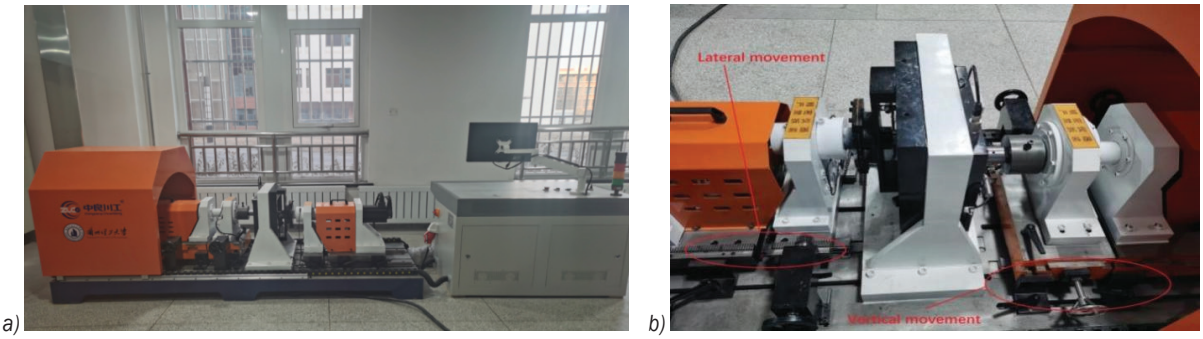

Fig. 1. *The elliptic gear transmission test rig; a) overall structure, and b) partial view of adjustable parts*

design, and time-varying meshing characteristics of elliptic gear, and then be used to guide the numerical control machining and error detection of elliptic gear.

Table 1. The design parameters of elliptic gears

Parameter	Value
Module, m [mm]	1.5
Number of teeth, z	53
Centre distance, a [mm]	80
Tooth width, B [mm]	28
Eccentricity, e	0.2
Pressure angle [°]	20
Equation of pitch curves	$r = 38.4 / (1 + 0.2 \cos \theta)$

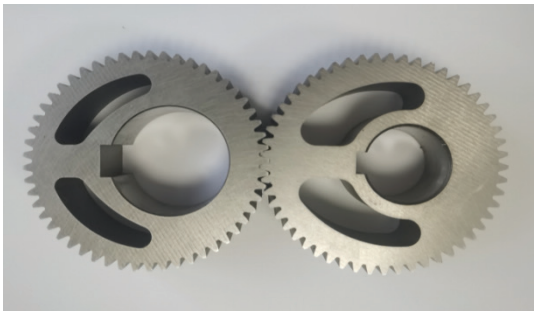

Fig. 2. *Machined elliptic gear pair*

The elliptic gear transmission test-bench adopts a horizontal mechanism, which is mainly comprises mechanical transmission system, measurement, and control system and data acquisition part [3]. Fig. 1 depicts the built elliptic gear test rig. The processed experimental gear is shown in Fig. 2, and the design parameters of elliptic gears are shown in Table 1. The precision mounting bracket and supporting multi-specification precision mounting accessories are designed to improve the universality of the test equipment, which can be applied to different types of NCG reducers. The established test rig is equipped with high-precision grating sensor system, high-precision torque sensor system and special measurement software to realize the automatic measurement of various performance of precision reducer. The reducer mounting bracket used in the test is fixed on the base, and a linear guide rail is installed on the platform base to realize the movement of each component [3]. The left-hand wheel and the right-hand wheel in Fig. 1b can ensure the longitudinal movement and lateral movement of the output assembly, which is convenient for the installation and disassembly of the accelerator and can be connected with the NCG transmission system suitable for different centre distances.

Fig. 3 shows the working principle of the test rig and the location and name of each component. The detailed configuration information of elliptic gear transmission test rig is shown in Table 2. The test rig can be used for the comprehensive performance test of the elliptic gear precision reducer. The test contents include the transmission efficiency of gear transmission, a fatigue life test, the temperature rise at the bearing end of the tested reducer, the transmission error of the tested reducer, the vibration at the input and output ends of the tested reducer, noise (including ambient noise), lost motion, torsional stiffness, backlash, starting torque, static friction torque, comprehensive measurement of dynamic friction moment, etc.

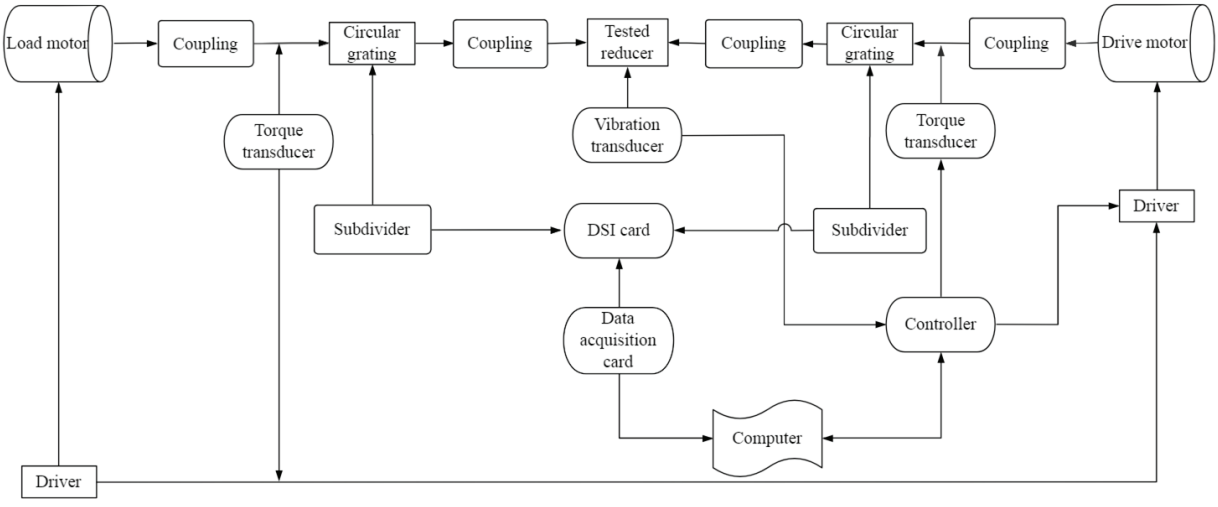

Fig. 3. *Working principle of the test rig*

Table 2. *Detailed configuration information of elliptic gear transmission test rig*

Part name	Model	Specifications
Torque sensor	YH-502	The measuring ranges are 20 N·m and 2000 N·m, respectively. Measurement accuracy: ±0.1 %. Power supply voltage: 24 V DC. Output signal: 10 ± 5k Hz. Torque accuracy: <± 0.1 % F·S. Frequency response: 100 μs
Noise sensor	RS-ZS-V05-2	Range: 30 dB to 120 dB. Frequency range: 20 Hz to 12.5 kHz. Measurement error: ±1.5 dB
Infrared temperature sensor	CK-01A	Temperature range: -20 °C to 300 °C. Spectral range: 8 μm to 14 μm. Measurement accuracy: ± 1 %. Response time: 50 ms to 300 ms optional
Vibration sensor	CA-YD-107	Frequency response: 0.5 Hz to 6000 Hz. Maximum lateral sensitivity: ≤ 5 %. Axial sensitivity: 50 PC/g. Magnetic sensitivity: 2 g/T. Base strain: 0.2 mg/μg
Circular grating	K-100	Power supply voltage: 24 V DC. Resolution: 48000 P/R. Protection grade: IP50
AC servo motor	MSME504G	Rated speed: 3000 rpm. Rated voltage: 400 V AC (three-phase). Torque: 15.9 N·m. Protection grade: IP67
Servo motor driver	MFDTA464	Rated voltage: 400 V AC (three-phase)
PLC	S7-200SMART	Power supply voltage: 220 V AC. I/O point: 30. AO channel: 4
Data acquisition card	NI-6351	Sampling rate: 1.25 MS/s. AI channel: 16. A/D accuracy: 16 bits. AO channel: 2. DIO channel: 24. Counting channel: 4

2 DYNAMIC TRANSMISSION CHARACTERISTIC ANALYSIS

By using elliptic gear test rig, this paper intends to analyse the dynamic lost motion, static lost motion, torsional stiffness, backlash, frictional torque, and vibration elliptic gear.

2.1 Dynamic Lost Motion of Elliptic Gear

Lost motion is an important factor to determine the transmission accuracy of a gear transmission system. When the movement direction of the gear system changes suddenly at a certain time, a certain lag appears in the output shaft, which will increase the dynamic transmission error of system [3]. Elliptic gears can realize specific motion laws of periodic motion, reciprocating motion, forward and reverse motion, etc. In reciprocating motion, the whole elliptic gear system needs frequent forward and reverse motion. The dynamic lost motion will lead to the disconnection between input and output in a short time, resulting in the sudden interruption of output and intermittent "beat vibration", which will reduce the transmission accuracy of the system. Therefore, the analysis of the dynamic lost motion is of great importance to improve its transmission accuracy.

The dynamic lost motion of a gear transmission system mainly includes back clearance and tooth deformation [3]. The measurement method is generally a two-way transmission error difference method, which refers to the measurement of the reverse transmission error first and then the forward transmission error under the stable load. At this time, the dynamic lost motion is defined as the difference between the transmission errors in the above two directions [20], that is:

$$DB = T_f E(\theta) - T_z E(\theta), \tag{1}$$

where DB is dynamic backlash, T_fE is counter-clockwise transmission error with no load condition, T_zE is clockwise transmission error with no load condition, *and* θ is rotation angle.

Fig. 4 shows the influence of load on the dynamic lost motion under the condition of constant speed (5 rpm). The maximum dynamic lost motion under three loads is 1.1 arcmin, 1.3 arcmin and 3.3 arcmin respectively at first cycle, and the second cycle is 1.5 arcmin, 1.8 arcmin and 3.5 arcmin, respectively. The dynamic lost motion changes periodically, and an amount of accumulation between adjacent cycles appears, which indicates that there is an error accumulation between the two cycles. The reason is that there is distortion between the transmission elements, which changes the centre distance and dynamic tooth side clearance. Therefore, the dynamic lost motion of elliptic gear will increase. The above analysis indicates that increasing of load promotes the generation of dynamic lost motion.

Fig. 5 shows the effect of rotating speed on the dynamic lost motion under constant load (10 N·m). Increasing the speed of the gear system can lead to the increase of its dynamic lost motion. The reason is that increasing the speed intensifies the elastic deformation between gear teeth and the dynamic backlash also increases, which are important components of dynamic backlash. Further analysis shows that there is a difference of dynamic lost motion between two cycles due to the accumulation in the previous cycle.

To summarize, the speed can promote the increase of dynamic lost motion of the elliptic gear.

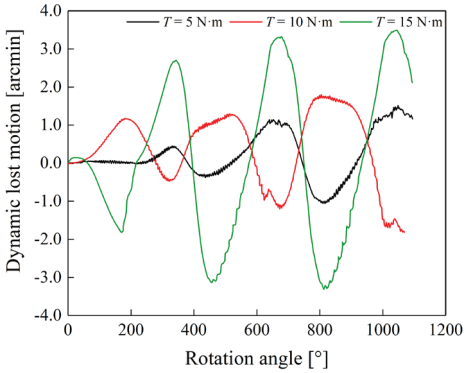

Fig. 4. *Influence of load on dynamic lost motion*

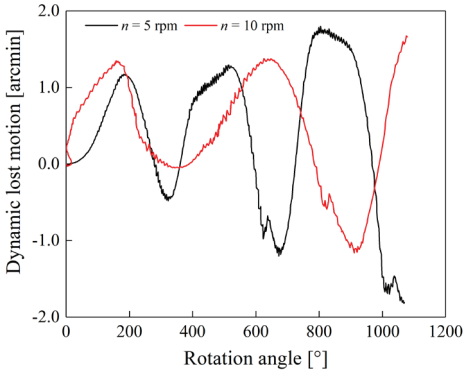

Fig. 5. *Influence of speed on dynamic lost motion*

2.2 Static Lost Motion of Elliptic Gear

Hysteretic characteristics are common in precision transmission systems, such as the gap in reducer and gear pair transmission, which can be regarded as a special case of hysteretic phenomenon. In general, the hysteretic characteristics of gears are mainly presented by static lost motion, which refers to the hysteresis of the output end on the angle when the moving direction of the precision reducer changes in the static state [21]. The static lost motion measurement can be used to verify whether the transmission accuracy of the designed gear reducer and the built test-rig meets the analysis requirements. In the industrial field, the hysteresis curve method is usually used to measure the static lost motion of gear transmission system [20], which is defined as the output shaft angle value caused by geometric factors such as tooth-side clearance and bearing clearance in the transmission chain when ±3 % rated torque is applied to overcome internal friction and oil film resistance, and when all components are in good contact [22]. The variation trend of static lost motion, backlash and stiffness with load parameters can be obtained from the hysteretic curve obtained from the test. In this paper, based on the lost motion model established in the literature [22], the lost motion of elliptic gear is obtained by means of transmission test. The distribution trend obtained is basically consistent with that in the literature [22], but there are some differences in the numerical value due to the consideration of many factors, such as lubrication, temperature, and friction during the test.

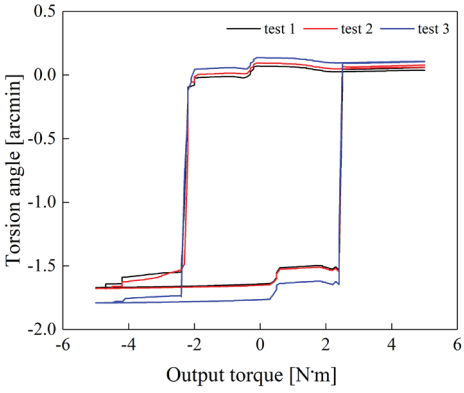

Fig. 6. *The hysteresis curve when T = 5 N·m*

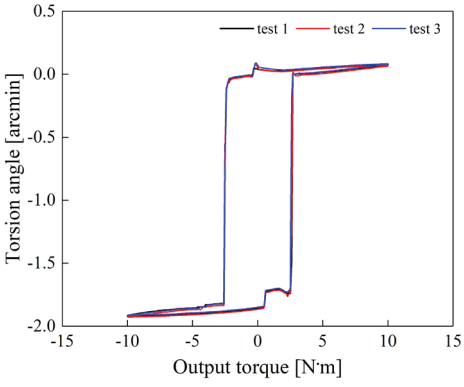

Fig. 7. *The hysteresis curve when T = 10 N·m*

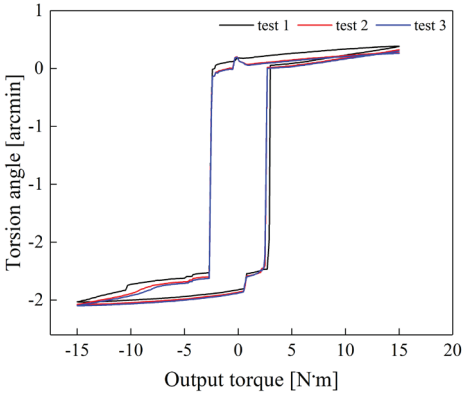

Fig. 8. *The hysteresis curve when T = 15 N·m*

When measuring the static lost motion, one end of the precision reducer is locked, and the other end forward gradient is loaded to the rated torque, and then the gradient is unloaded. In the same way, reverse gradient loading to the rated torque, then gradient unloading, real-time torque and torsional angle signals are collected, and hysteresis curves are drawn. High precision circular grating is used to collect the angle of input and output ends. While ensuring the measurement accuracy, it can measure the reducer of variable ratio transmission, which is more suitable for variable ratio transmission mechanism. During the test, the load torque is set as 5 N·m, 10 N·m, and 15 N·m, after measuring three times in each torque data, and the drawn hysteresis curve is shown in Fig. 6 to Fig. 9. The comparative analysis shows that there are some differences between them due to the variability of tooth profiles, but the hysteretic curves under the three torque values basically maintain the same change trend, which further verifies the correctness of data acquisition.

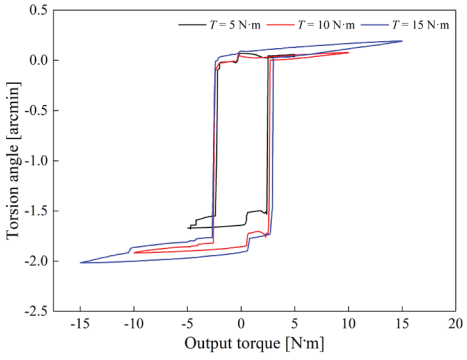

Fig. 9. *Variation trend of hysteretic curve with load*

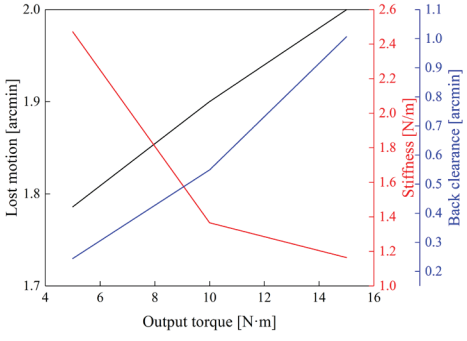

Fig. 10. *Variation trend of lost motion, stiffness, and back clearance of elliptic gear with load*

Fig. 9 depicts the variation of hysteresis curve with load. The value of torsional angle in hysteretic curve increases gradually with the increase of load. Because the load intensifies the deformation between gear teeth, the static lost motion shows an increasing trend. By collecting forward and reverse torsional angles at ±3 % of the rated torque on the hysteretic curve, the difference of the mean value of the angle is taken as the static lost motion of the system. On this basis, the variation trend of the lost motion, stiffness, and back clearance of the system with the torque is drawn, as shown in Fig. 10. During the test, the input end remains fixed, and the ratio of the torque borne by the output end to the elastic torsion angle of the output end, which is the stiffness is calculated. The difference between the torsion angle of the falling curve and the rising curve in the hysteretic curve when the load torque is 0 N·m is defined as the back clearance. As can be seen from Fig. 10, the load can increase the lost motion and backlash and inhibit the increase of stiffness of the elliptic gears. The reason is that the load intensifies the deformation between gear teeth and increases the clearance between gear teeth, which leads to the reduction of the ability of gear teeth to resist deformation.

2.3 Frictional Torque of Elliptic Gear

The measurement of friction torque is an important index to evaluate its tribological performance of gear system, [23] and [24], which is of great significance for the analysis of friction distribution law and tooth surface wear trend of elliptic gears. During the experimental analysis of gear transmission, when the operation is stable, the no-load friction torque is equivalent to the input torque of reducer. The input torque can be obtained through the torque sensor installed at the input, namely:

$$T_f = T_{in}, \tag{2}$$

where T_f is the no-load friction torque, and T_{in} is the input torque.

Generally, the mean value of torque signal is filtered, and the mean value of torque is taken as the friction torque at this speed, so as to obtain the one-to-one correspondence between friction torque and speed.

$$\bar{T}_f = \text{MEAN}(T_f). \tag{3}$$

During the experiment, the no-load friction torque is to measure the input torque at different stable speeds at the input under no-load conditions. collecting the torque model in real time and setting the input speed gradient to 50 rpm and the maximum input speed to 300 rpm. The variation trend of no-load

friction torque with speed is analysed by forward and reverse rotation.

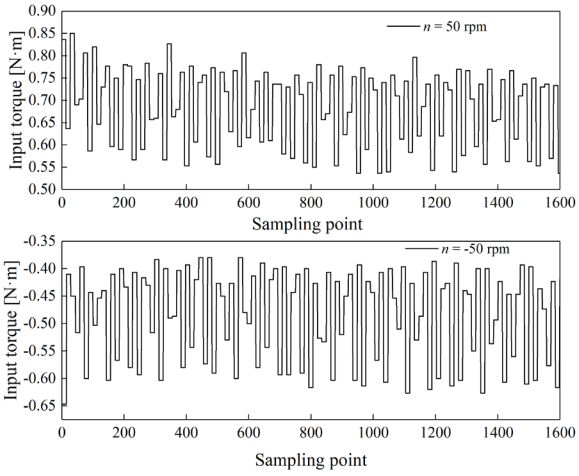

Fig. 11. *Torque distribution at n = 50 rpm, and n = –50 rpm*

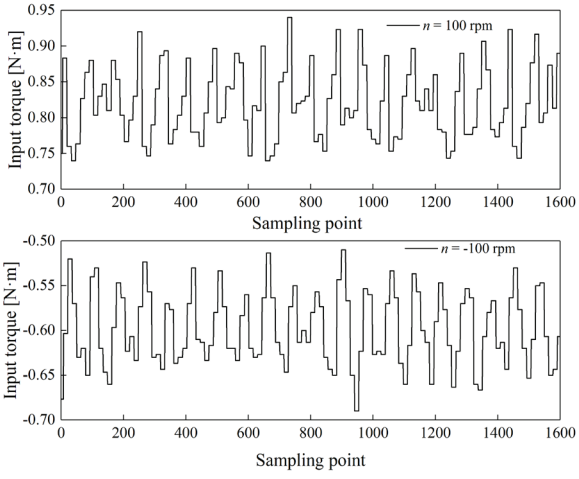

Fig. 12. *Torque distribution at n = 100 rpm, and n = –100 rpm*

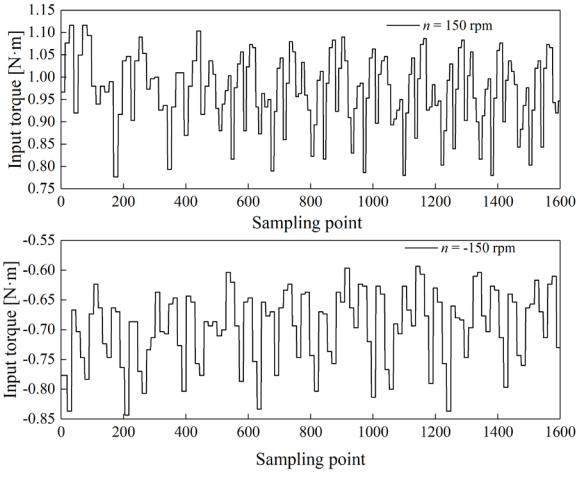

Fig. 13. *Torque distribution at n = 150 rpm, and n = –150 rpm*

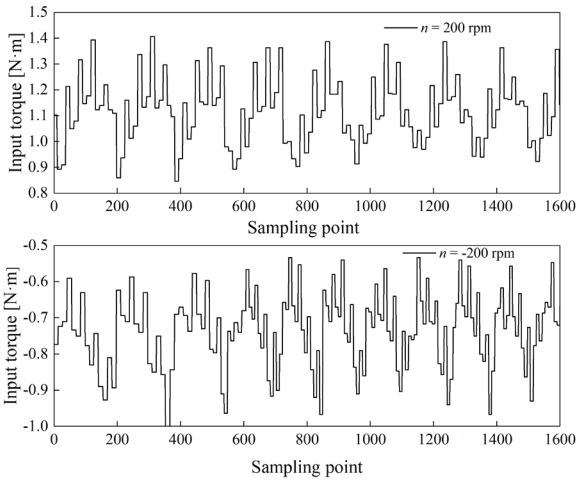

Fig. 14. *Torque distribution at n = 200 rpm, and n = –200 rpm*

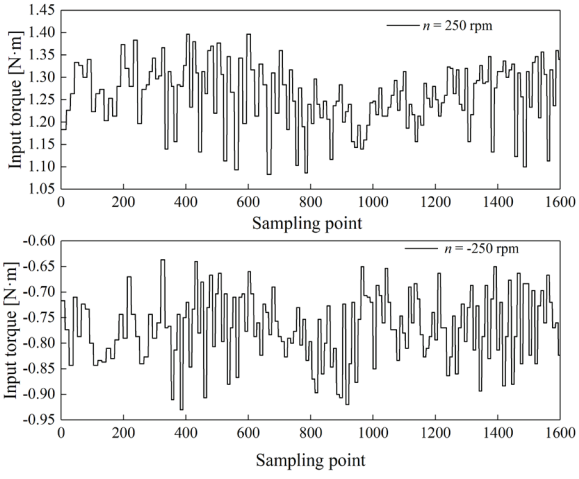

Fig. 15. *Torque distribution at n = 250 rpm, and n = –250 rpm*

Fig. 11 to Fig. 16 describe the variation trend of input torque of elliptic gear pair under different speed conditions. When the elliptic gears mesh with each other, the meshing forces at different meshing positions are different, and the inconsistency of elliptic gear tooth profile exacerbates this phenomenon. This leads to different unknown friction moments of different meshing of elliptic gear pairs and presents a periodic change trend. In contrast, the periodicity is less obvious at low speeds. With the increase of speed, it gradually shows a periodic change trend, and the forward rotation input torque is greater than the forward rotation input torque under the same conditions.

Fig. 17 shows the variation law of no-load friction torque of elliptic gear transmission system with speed. With the increase of gradient in the range of 50 rpm and 300 rpm, the no-load friction torque shows an upward trend, which indicates that there

is a positive correlation between friction torque and speed in a certain range. Therefore, in actual working conditions, in order to reduce power loss, the system speed should quickly reach a constant state, so as to reduce unnecessary work and power loss.

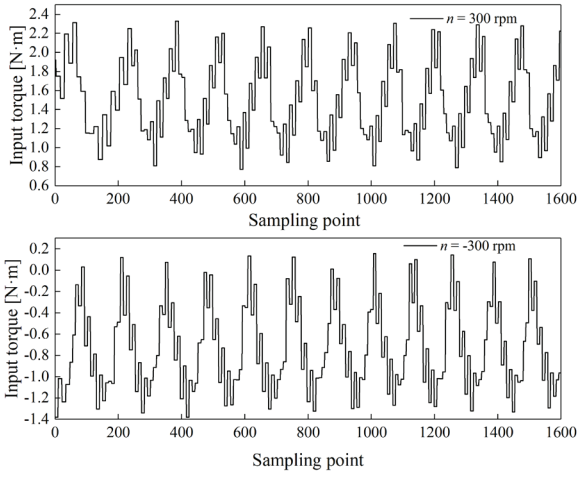

Fig. 16. *Torque distribution at n = 300 rpm, and n = –300 rpm*

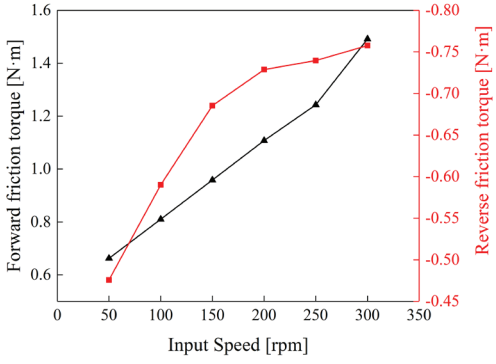

Fig. 17. *Corresponding relationship between input speed and friction torque*

2.4 Vibration Characteristics of Elliptic Gears

In the process of gear meshing transmission, impact and vibration are inevitable, and impact is also one of the main causes of vibration in gear transmission system. The inconsistency of elliptic gear profile intensifies the meshing impact between teeth, which leads to the increase of its vibration. The vibration signal collected through the transmission test can be used to determine whether there is unilateral and bilateral impact in the system. Then, it is used to optimize the gear system and improve its transmission accuracy and transmission performance. During the elliptic gear transmission test, the load gradient is set as 5 N·m, the maximum load as 15 N·m, the speed gradient as 10rpm, and the maximum speed as 80 rpm. The no-load speed gradient is 50 rpm, and the maximum speed is 300 rpm. The vibration signal of gear system obtained by vibration sensor can be used to analyse the variation trend of vibration of elliptic gear transmission system with working conditions.

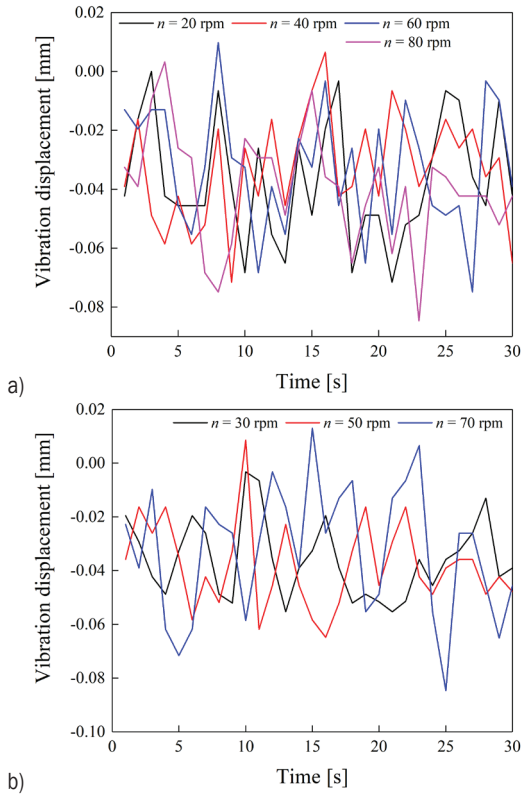

Fig. 18. *Vibration distribution under different speeds; a) T = 5 N·m, and b) T = 10 N·m*

In Fig. 18, with the increase of rotating speed, the vibration amplitude gradually increases, and the fluctuation is more obvious. Under the conditions of two loads (5 N·m and 10 N·m), they all show the same distribution law. The vibration displacement of the gear system is basically less than 0 mm when the rotating speed is 20 rpm and 30 rpm. With the further increase of rotating speed, the vibration displacement of the system is gradually greater than 0 mm, which indicates that the system gradually transits from the original unilateral impact to bilateral impact, and the vibration intensity and amplitude increase. The corresponding frequency domain response is shown in Fig. 19. In the theoretical state, when the vibration displacement of the gear system is 0 mm, it is a non-impact state [25] and [26]. When the vibration displacement of the system is all positive or negative, it is a unilateral impact state. If both positive and

negative values appear in the vibration displacement of the system, it is recognized as a bilateral impact state. The above analysis indicates that that the vibration amplitude is small at low speed, and there is only unilateral impact. When the rotating speed increases gradually, the system will have a bilateral impact state.

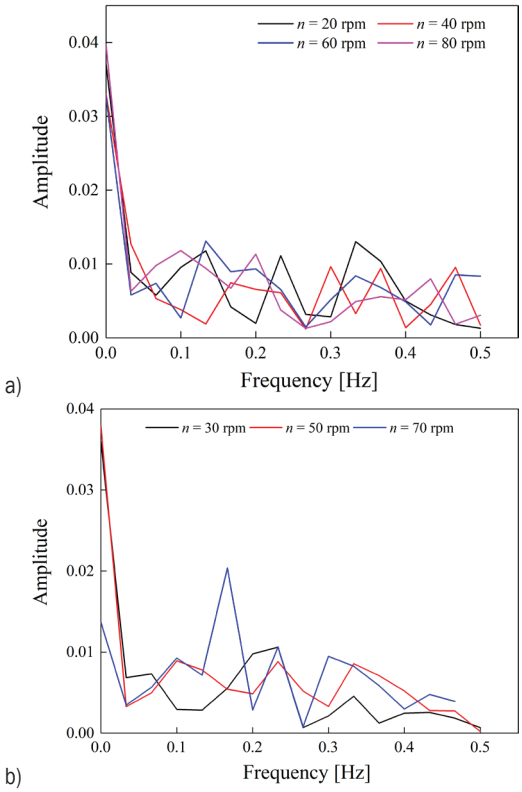

Fig. 19. *Frequency domain response of vibration at different rotational speeds; a) T = 5 N·m, and b) T = 10 N·m*

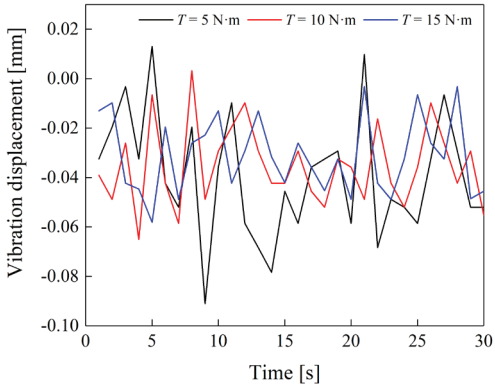

Fig. 20. *Vibration distribution law under different loads*

Fig. 20 depicts the variation trend of the vibration of the system with the load, and the corresponding frequency domain response is shown in Fig. 21. When the load gradient increases within 5 N·m to 15 N·m, the vibration amplitude tends to decrease, and the fluctuation increases gradually. The reason for this phenomenon is that the rated load applied on the driven wheel will be transmitted to the driving wheel through the time-varying transmission ratio between the driving and driven wheels. In this process, the inconsistency between the teeth increases the impact between the gears. Further analysis shows that when the load is 15 N·m, the vibration amplitude is less than 0 mm, indicating that it is a unilateral impact state. With the increase of load, both positive and negative conditions appear in the vibration displacement curve of the gear system, indicating that the gear transmission system is a bilateral impact state at this time.

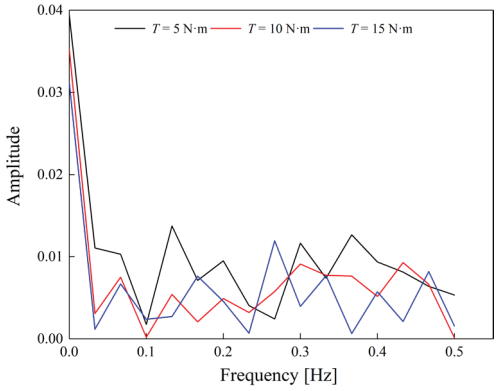

Fig. 21. *Frequency domain response distribution of vibration under different loads*

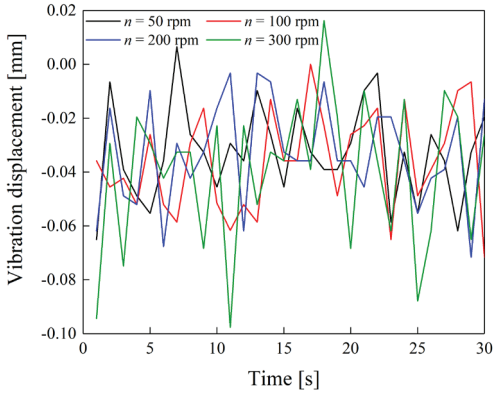

Fig. 22. *Influence of rotating speed on vibration under no-load condition*

Fig. 19 depicts the variation trend of vibration with speed when there is no load, and the corresponding frequency domain response is shown in Fig. 23. With the increase of rotating speed, the vibration amplitude of the system increases gradually,

and the fluctuation increases gradually, indicating that the meshing impact of the system is also increasing gradually. In contrast, the load in a certain range can inhibit the increase of the amplitude of the system vibration and will make the gear system transition from bilateral impact to unilateral impact. This indicates that increasing the load can improve the stability of the elliptic gear transmission system.

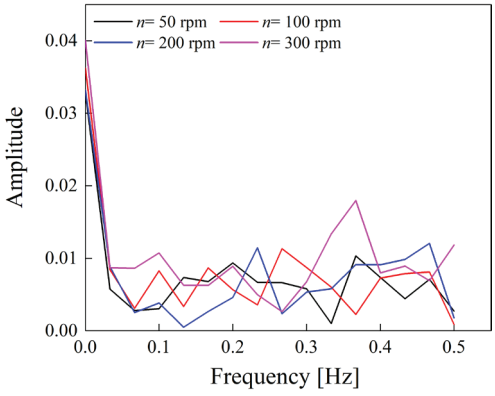

Fig. 23. *Frequency domain response of rotational speed to vibration*

3 CONCLUSIONS

This paper mainly carries out relevant experimental research on the transmission characteristics of elliptic gears. By building an elliptic gear transmission test-rig and collecting experimental data, the effects of working condition parameters on the transmission error, dynamic lost motion, static lost motion, and transmission efficiency of elliptic gear are obtained. The increase of speed and load will increase the dynamic lost motion and friction torque. The static lost motion and backlash will gradually increase with the increase of torque, and the meshing stiffness will gradually decrease with the increase of load. The vibration of the elliptic gear transmission system is sensitive to speed, which will increase the vibration displacement and volatility, and the system will transition from unilateral impact to bilateral impact. The load can restrain the generation of vibration in a certain range. With the increase of load, the system will transition from bilateral impact to unilateral impact. Therefore, in a certain range, the transmission accuracy and transmission stability can be improved by reducing the speed or increasing the load. The transmission characteristic analysis method and test method proposed can be applied not only to NCG transmission systems but also to other types of gear transmission systems.

4 ACKNOWLEDGMENTS

This study was supported by the National Natural Science Foundation of China (No.52265008, No.52105058,), and Natural Science Foundation of Gansu Province (No.21JR7RA23), and Open Research Fund of State Key Laboratory of High-Performance Complex Manufacturing, Central South University+ Kfkt2021-11.

5 REFERENCES

[1] Dong, C., Liu, Y., Wei, Y., Yun, B., Li, D., Dong, Z. (2020). Analysis on meshing characteristics and transmission error of elliptic gears. *Mathematical Problems in Engineering*, vol. 2020, art. ID 2017218, **DOI:10.1155/2020/2017218**.

[2] Dong, C., Liu, Y., Wei, Y. (2019). Dynamic contact characteristics analysis of elliptical cylinder gear under different load conditions. *Journal of Huazhong University of Science and Technology (Natural Science Edition)*, vol. 47, p. 103-107.

[3] Dong, C., Liu, Y. (2022). Experimental study on transmission error and dynamic backlash of elliptic gear transmission system. *Proceedings of the Institution of Mechanical Engineers, Part K: Journal of Multi-body Dynamics*, vol. 236, no. 1, p. 130-139, **DOI:10.1177/14644193221077494**.

[4] Liu, X., Nagamur, K., Ikejo, K. (2012). Simulation on the vibration characteristics of elliptic gears. *Proceedings of the Institution of Mechanical Engineers, Part C: Journal of Mechanical Engineering*, vol. 227, no. 4, p.819-830, **DOI:10.1177/0954406212454372**.

[5] Liu, X., Nagamur, K., Ikejo, K. (2012). Vibration and noise characteristics of elliptic gears due to non-uniform rotation. *Journal of Advanced Mechanical Design, Systems, and Manufacturing*, vol. 6, no. 4, p. 498-512, **DOI:10.1299/jamdsm.6.498**.

[6] Gao, N., Meesap, C., Wang. S. (2020). Parametric vibrations and instabilities of an elliptic gear pair. *Journal of Vibration and Control*, vol. 26, no. 19-20, p.1721-1734, **DOI:10.1177/1077546320902543**.

[7] Karpov, O., Nosko, P., Fil, P., Nosko, O., Olofsson, U. (2017). Prevention of resonance oscillations in gear mechanisms using non-circular gears. *Mechanism and Machine Theory*, vol. 114, p. 1-10, **DOI:10.1016/j.mechmachtheory.2017.03.010**.

[8] Lin, C., Liu, Y., Gu, S. (2015). Analysis of nonlinear twisting vibration characteristics of orthogonal curve-face gear drive. *Journal of the Brazilian Society of Mechanical Sciences and Engineering*, vol. 37, p. 1499-1505, **DOI:10.1007/s40430-014-0296-y**.

[9] Cai, Z., Lin, C. (2017). Dynamic model and analysis of nonlinear vibration characteristic of a curve-face gear drive. *Strojniški vestnik - Journal of Mechanical Engineering*, vol. 63, no. 3, p. 161-170, **DOI:10.5545/sv-jme.2016.3859**.

[10] Liu, D., Ba, Y., Ren, T. (2019). Flow fluctuation abatement of high-order elliptic gear pump by external noncircular gear drive. *Mechanism and Machine Theory*, vol. 134, p. 338-348, **DOI:10.1016/j.mechmachtheory.2019.01.011**.

[11] Liu, D., Gu, D., Liu, D. (2019). Coupled vibration modeling and dynamic characteristics of noncircular face gear drive system with time-varying instantaneous center excitation. *Proceedings of the Institution of Mechanical Engineers, Part C: Journal of Mechanical Engineering Science*, vol. 233, no. 14, p. 4947-4959, **DOI:10.1177/0954406219841085**.

[12] Liu, D., Wang, G., Ren, T. (2017). Transmission principle and geometrical model of eccentric face gear. *Mechanism and Machine Theory*, vol. 109, p. 51-64, **DOI:10.1016/j.mechmachtheory.2016.10.024**.

[13] Liu, D., Ren, T., Ba, Y. (2016). Torsional vibration model and its dynamic characteristics for a noncircular gear based on separation of elastic rotating angle. *Journal of Vibration and Shock*, vol. 35, p. 228-233.

[14] Liu, X., Nagamur, K., Ikejo, K. (2012). Analysis of the dynamic characteristics of elliptic gears. *Journal of Advanced Mechanical Design, Systems, and Manufacturing*, vol. 6, no. 4, p. 484-497, **DOI:10.1299/jamdsm.6.484**.

[15] Vasie, M., Andrei, L. (2012). Analysis of noncircular gears meshing. *Mechanical Testing and Diagnosis*, vol. 4, p.70-78.

[16] Han, J., Li, D., Tian, X., Xia, L. (2020). Meshing principle and transmission analysis of a beveloid non-circular gear. *Advances in Mechanical Engineering*, vol. 12, no. 11, p.1-11, **DOI:10.1177/1687814020971909**.

[17] Lin, C., Xia, X., Li, P. (2018). Geometric design and kinematics analysis of coplanar double internal meshing non-circular planetary gear train. *Advances in Mechanical Engineering*, vol. 10, no. 12, p. 1-12, **DOI:10.1177/1687814018818910**.

[18] Lin, C., He, C. (2018). Tooth contact analysis of elliptic bevel gear with different misalignment. *Proceedings of the Institution of Mechanical Engineers, Part C: Journal of Mechanical Engineering*, vol. 233, no. 7, **DOI:10.1177/0954406218791637**.

[19] Dooner, D.B., Mundo, D. (2022). Unloaded transmission error and instantaneous gear ratio for non-circular gears with misalignments. *Mechanism and Machine Theory*, vol. 170, art. ID 104728, **DOI:10.1016/j.mechmachtheory.2022.104728**.

[20] Xu, H., Shi, Z., Yu, B. Wang, H. (2019). Dynamic measurement of the lost motion of precision reducers in robots and the determination of optimal measurement speed. *Journal of Advanced Mechanical Design Systems and Manufacturing*, vol. 13, no. 3, **DOI:10.1299/jamdsm.2019jamdsm0044**.

[21] Zhang, C., Dong, H., Wang, D., Cheng, Y. (2021). Tolerance synthesis for lost motion requirement of planetary gear train based on a mechanism model. *Mechanism and Machine Theory*, vol. 164, art. ID104405, **DOI:10.1016/j.mechmachtheory.2021.104405**.

[22] Shi, Z., Xu, H., Lin, J., Yu, B. (2018). Research on measurement and evaluation system of precision reducer lost motion. *Chinese Journal of Scientific Instrument*, vol. 39, no. 6, p. 56-63, **DOI:10.19650/j.cnki.cjsi.J1803236**. (in Chinese)

[23] Han, L., Niu, W., Zhang, D., Wang, F. (2013). An improved algorithm for calculating friction force and torque in involute helical gears. *Mathematical Problems in Engineering*, vol. 2013, art. ID 575302, **DOI:10.1155/2013/575302**.

[24] Kar, C., Mohanty, A.R. (2007). An algorithm for determination of time-varying frictional force and torque in a helical gear system. *Mechanism and Machine Theory*, vol. 42, no. 4, p. 482-496, **DOI:10.1016/j.mechmachtheory.2006.04.007**.

[25] Liu, D., Lv, Z., Zhao, G. (2021). Rattle dynamics of noncircular face gear under multifrequency parametric excitation. *Mechanical Sciences*, vol. 12, p. 361-373, **DOI:10.5194/ms-12-361-2021**.

[26] Liu, D., Zhao, G., Fu, Z. (2022). Rattle dynamic model and vibration behaviors of noncircular face gear. *Journal of Computational and Nonlinear Dynamics*, vol. 17, no. 6, art. ID 061002, **DOI:10.1115/1.4053933**.

Strojniški vestnik - Journal of Mechanical Engineering 68(2022)11, 713-721
© 2022 The Authors. CC BY 4.0 Int. Licensee: SV-JME
DOI:10.5545/sv-jme.2022.242
Original Scientific Paper
Received for review: 2022-06-20
Received revised form: 2022-09-03
Accepted for publication: 2022-11-04

Comparison of Load-Carrying Capacity, Wear, and Resource of Metal-Polymer Corrected Spur Gears with a Gear Made of Polyamides PA6 or PA6+30CF

Myron Chernets[1] – Marek Opielak[2] – Anatolii Kornienko[1,*]
[1] National Aviation University, Aerospace Faculty, Ukraine
[2] Lublin University of Technology, Poland

Based on the developed calculation research method of metal-polymer gears the analysis of the influence of height and angular correction of engagement of spur gears on load-carrying capacity, linear teeth wear, and resources is carried out. Gears with a pinion made of carbon steel 0.45%C and a gear made of basic polyamide PA6 or carbon fibre composite PA6 + 30CF were investigated. Quantitative and qualitative patterns of influence of both types of correction, changes in the initial teeth profile due to wear, mating conditions on the load carrying capacity, teeth linear wear, and service life of investigated metal-polymer gears have been established. Profile correction causes a decrease in the contact pressure in the engagement by different amounts during the meshing cycle. They are most significantly reduced in the input area of two-pair engagement. It was found that when using PA6 + 30CF, the maximum contact pressures are about 1.29 times higher than with PA6 at all values of the shift coefficients, regardless of its type. The tooth linear wear has different values during the meshing cycle depending on the shift coefficients and parity of engagement. The resource first increases with increasing the shift coefficients, reaching their optimum, and then decreases again. Regularities of this influence for each type of correction of engagement are established. Metal-polymer gears with a gear made of PA6 + 30CF will have a significantly higher service life than with a gear made of PA6.

Keywords: metal-polymer spur gear, height and angular correction of engagement, polyamides PA6 and PA6 + 30CF, maximum contact pressures, linear teeth wear, resource

Highlights

- *Calculation of contact pressures, wear, and resources of corrected MP spur gears is performed.*
- *The influence of height and angular teeth correction on these service characteristics of gears is investigated.*
- *Quantitative and qualitative patterns of the effect of correction on these characteristics are given.*
- *The optimal values of the shift coefficients providing maximum gears resource are determined.*
- *A comparative evaluation of service characteristics of gears made of PA6 and PA6 + 30CF was performed.*

0 INTRODUCTION

Metal-polymer (MP) gears are common in various fields of human activity, in a variety of technical devices, mechanisms, and machines. As with metal gears in MP gears for the purpose of increasing their loading carrying capacity, resources, and wear resistance, profile shifting is used. However, effective methods for calculating tribotechnical parameters, i.e., the tooth wear and resource of both uncorrected and corrected MP have not been developed. There are standardized calculation methods **[1]** and **[2]** and numerical methods **[3]** to **[5]** for studying uncorrected gears with metal-toothed wheels. In **[3]** to **[5]**, the modelling of the tooth wear of spur and screw gears by numerical methods with Archard's linear law of abrasion wear was carried out. They were used to assess the load-carrying capacity of MP gears in **[6]** to **[10]**, where the contact and bending teeth strength was studied. In **[6]** and **[7]**, the MP gears with a gear made of polyamide PA6 were investigated for these stresses. In **[8]**, the load capacity of spur gears with PA66 was studied. In contrast, virtually no computational methods exist for studying the wear and resources of MP gears in the literature. **[9]** presents simplified and **[10]** presents improved methods for calculating the wear resistance of an MP spur gears with a gear made of PA6 + 30GF, PA6 + 30CF with dispersed glass and carbon fibres. Dry friction using Archard's law of abrasive wear is considered, by which the wear is directly proportional to the contact pressure and depends linearly on the path of sliding friction. This wear mechanism is not inherent, much less dominant for MP gears.

Regarding the study of the effect of correction (height or angle) on the load-carrying capacity, wear, and resources of MP gears, such methods and relevant calculations are not available in the literature. There are some results in the literature of studies of metal gears with corrected teeth **[11]** to **[16]** for their load-carrying capacity and efficiency. Accordingly, in **[11]**, on the basis of the wear model of screw gears, the influence of different types of profile shifting on wear according to Acrhard's law was investigated; in **[12]**,

*Corr. Author's Address: National Aviation University, Lubomyr Huzar 1, 03680 Kyiv, Ukraine, anatoliykor80@gmail.com

the influence of the angular correction of spur gears on the contact and bending stresses was investigated; in **[13]** and **[14]**, the analysis of influence of geometrical parameters of gears, including teeth correction to the specified stresses was given; in **[15]**, the optimization algorithm for spur gears with height correction of engagement is presented; in **[16]**, the influence of height correction on normal Mises stresses, bending stresses, and teeth deformation was studied.

Also, **[17]** provides an overview of various types of metal spur and helical gears with non-involute teeth, found in various applications. The comparison of involute and non-involute gears was carried out on the basis of the following criteria: Hertzian pressure, oil film thickness, bending stress at the root of the tooth, contact temperature, and gear noise.

Given the urgency of these scientific and technical problems, a modified method of calculating MP gears with correction of engagement was developed **[18]** and **[19]** based on the author's multicriteria generalized method of studying metal gears, including correction of engagement **[21]** to **[25]**. These calculation methods are based on the phenomenological methodology of research of wear resistance at sliding friction **[20]** and **[21]** by friction-fatigue mechanism. This approach is fundamentally different from the wear mechanism of metal-polymer tribocouples according to the adhesive-abrasive wear Archard's law.

The solution of the wear-contact problem is given in the article and the tribological behaviour of MP spur gears with a steel pinion and gears made of two polyamides: unreinforced PA6 or reinforced with short carbon fibres PA6 + 30CF composite is investigated. The study considered such real factors as the conditions of tooth engagement, height and angular correction of engagement, and the impact of tooth wear on contact pressures and resource.

1 CALCULATION METHODS

The calculation method aspects for the study of uncorrected MP spur gears are thoroughly presented in authors' previous works **[18]** and **[19]**. Therefore, the following are the basic design relationships for gears with height and angular correction of engagement.

The teeth contact strength of the MP gears is determined using the known Hertz formula for different gear materials. Respectively

$$p_{j\max} = 0.564\sqrt{N'/(\theta\rho_j)}, \qquad (1)$$

where $p_{j\max}$ is initial maximum contact pressures at the j^{th} point, which occur under the action of nominal torque; $j=0,1,2,\ldots,s$ the points of contact on the teeth profiles; $N'=N/(bw)$; $N=T_{nom}K_g/(r_1\cos\alpha)$ force in engagement; $T_{nom}=9550P/n_1$ rated torque; P power on the driving shaft; n_1 pinion rotational speed; K_g dynamic coefficient; $r_1=z_1m$ pitch circle diameter of the pinion; m module; $\alpha=20°$ pressure angle; z_1, z_2 numbers of teeth; $\theta=\left(1-\nu_1^2\right)/E_1+\left(1-\nu_2^2\right)/E_2$; E, ν Young's modules and Poisson's ratios; b face width; w the number of teeth pairs in engagement; ρ_j reduced radius of curvature of the tooth profiles at the j^{th} point.

Respectively,

$$\rho_j = \frac{\rho_{1j}\rho_{2j}}{\rho_{1j}+\rho_{2j}}, \quad j = 0,1,2,3,\ldots,s, \qquad (2)$$

where ρ_{1j}, ρ_{2j} are the radii of curvature of the teeth profiles of the spur pinion and gear at j^{th} point **[19]** and **[25]**, $j=0$ and $j=s$ correspond to the first and last point of the teeth engagement.

The linear teeth wear h'_{2j} of the polymer gear 2 at any point j of their profiles during a single time of their contact t'_j in a one-pair engagement at maximum contact pressure $p_{j\max}$ is calculated as follows **[18]**, **[21]**, **[22]** and **[24]**.

$$h'_{kj} = \frac{v_j t'_j \left(fp_{j\max}\right)^{m_k}}{C_k\left(0.5R_m\right)^{m_k}} = \frac{v_j t'_j \left(\tau_{j\max}\right)^{m_k}}{C_k\left(\tau_S\right)^{m_k}}, \qquad (3)$$

where $v_j=\omega_1 r_{b1}(tg\alpha_{1j}-tg\alpha_{2j})$ **[21]** and **[22]** sliding speed in the engagement; $t'_j=2b_j/v_0$ time of teeth contact at movement of j^{th} contact point on a tooth profile to hertz contact patch width $2b_j=2.256\sqrt{\theta N'\rho_j}$; $v_0=\omega_1 r_1\sin\alpha$ the speed of contact point movement on the tooth profile; ω_1 pinion angular velocity; f sliding friction coefficient; $\tau_{j\max}=fp_{j\max}$ specific force of friction according to Coulomb's law; R_m tensile strength of polymeric material under tension (compression); τ_{S2} the shear strength of the gear polymer material; C_k, m_k wear resistance characteristics of gear materials; k = 1, 2, toothed wheels numbering (1 – pinion, 2 – gear).

In spur gears two - one - two-pair teeth engagement is realized. The angle $\Delta\varphi_{1F_2}$ of exit from the two-pair and at the same time the entrance to the one-pair engagement and the angle $\Delta\varphi_{1F_1}$ of exit from it is determined according to the author's method

During the gears operation due to the teeth slippage in the engagement, their wear inevitably occurs. Its variable value during each subsequent act of their tribocontact is calculated as follows **[19]**, **[21]**, **[22]**, and **[25]**:

$$h'_{kjn} = \frac{v_j t'_{jh} \left(fp_{jh\max} \right)^{m_k}}{C_k \left(0.5R_m \right)^{m_k}}, \quad (4)$$

where $t'_{jh}=2b_{jh}/v_0$=var time of teeth wear during movement of j that point of their contact along a tooth contour to a variable due to wear width of a contact patch $2b_{jh}$; $p_{jh\max}$ variable maximum contact pressure at the j^{th} point of teeth interaction during wear.

As a result of tooth profiles wear their initial radii of curvature increase ρ_{1j}, ρ_{2j}. Consequently, the maximum contact pressures $p_{j\max}$ are reduced and the width of the contact patch $2b_j$ at j^{th} points is increased. Accordingly, their current values of $p_{jh\max}$ and $2b_{jh}$ are calculated according to modified Hertz formulas **[19]** and **[25]**:

$$p_{jh\max} = 0.564\sqrt{N'/(\theta\rho_{jh})}, \; 2b_{jh} = 2.256\sqrt{\theta N'\rho_{jh}}, \quad (5)$$

where $\rho_{jh}=(\rho_{1jh}\rho_{12h})/(\rho_{1jh}+\rho_{12h})$ is the reduced radius of curvature of the gear profile, changeable in the result of wear, ρ_{1jh}, ρ_{2jh} changeable curvature radii of pinion and wheel tooth profiles.

The variable radii of curvature ρ_{kjh} are calculated according to the method given in **[18]**, **[19]**, and **[25]**.

For the numerical solution, a block calculation procedure is used, in which, during a randomly selected number of teeth interactions (blocks of interactions B), the single wear is calculated according to Eq. (2) followed by linear summation **[18]** and **[25]**. In each subsequent block, the single wear of the teeth is calculated by Eq. (4).

For the number of revolutions of the pinion n_{1s} and the gear n_{2s} corresponding to a certain number of the accepted size of the interaction blocks B with constant contact conditions, their total wear h_{1jn} and h_{2jn} at j^{th} points of contact is determined as follows:

$$h_{1jn} = \sum_{1}^{n_{1s}} h_{1jB}, \quad h_{2jn} = \sum_{1}^{n_{2s}} h_{2jB}, \quad (6)$$

where $n_{2s}=n_{1s}/u$; $h_{kjB}=\Sigma\, h'_{kj}$ teeth wear in each block of their interaction.

Then, considering the change in initial contact pressures $p_{j\max}$ due to tooth wear, the gears resource t_B at the calculated number of revolutions n_{1s} or n_{2s} is expressed as follows:

$$t_B = \frac{n_{1s}}{60n_1} = \frac{n_{2s}}{60n_2}. \quad (7)$$

The above method of calculating the uncorrected MP gears is also used **[22]**, **[24]** and **[26]**. For gears with height and angular correction (Fig. 1).

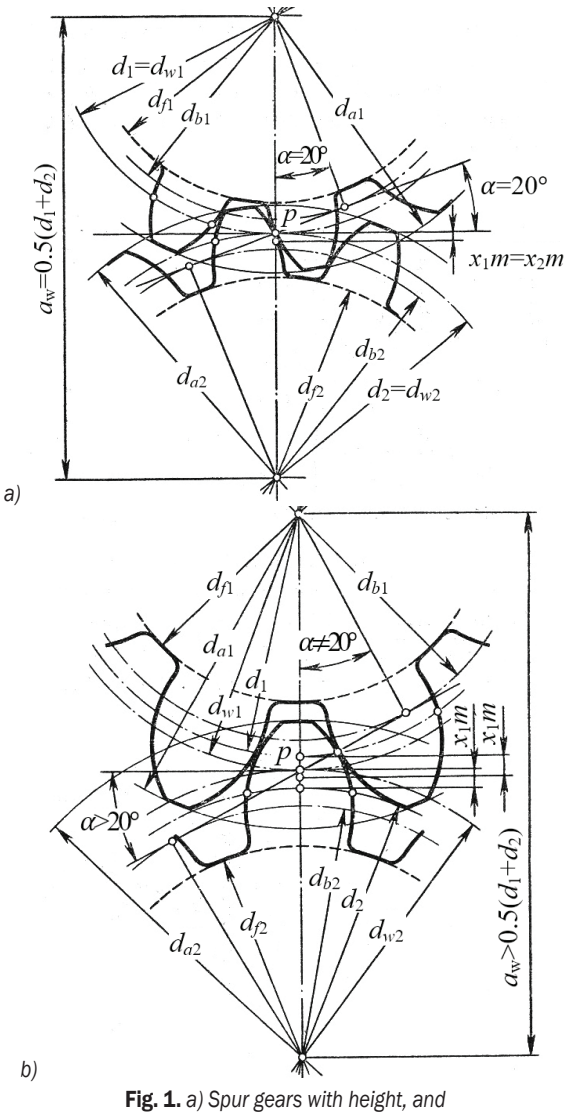

Fig. 1. *a) Spur gears with height, and b) correction and angular correction*

In gears with height correction, the shift coefficients are assumed to be the same $x_1=-x_2$ and the total shift coefficient is $x_\Sigma=x_1+x_2=0$. Accordingly, the centre distance $a=r_1+r_2$ remains the same as in the gears without offset. Only the addendum and dedendum radii will be variable

$$r_{a1} = r_1 + (1+x_1)m, \quad r_{a2} = r_2 + (1+x_2)m, \quad (8)$$

$$r_{f1} = r_1 + (1.25-x_1)m, \quad r_{f2} = r_2 + (1.25-x_2)m, \quad (9)$$

where $r_2=mz_2$ is a pitch radius.

All formulas for calculating other parameters have the same structure as for uncorrected gears **[22]**.

In gears with angular correction, the shift coefficients $x_1\neq x_2$ (usually $x_1>0$, $x_2>0$); total shift coefficient $x_\Sigma>0$; the corrected centre distance

$a_w=(r_{w1}+r_{w2})>a$; the corrected pressure angle $\alpha_w>\alpha$ on the initial pitch circle. Accordingly, the pitch radii of the pinion and the gear, radii of the addendum and dedendum are expressed as follows

$$r_{w1}=r_1\frac{\cos\alpha}{\cos\alpha_w},\quad r_{w2}=r_2\frac{\cos\alpha}{\cos\alpha_w}, \tag{10}$$

$$r_{a1}=r_1+(1+x_1-K)m,\quad r_{a2}=r_2+(1+x_2-K)m, \tag{11}$$

$$r_{f1}=r_1+(1.25-x_1+K)m,$$
$$r_{f2}=r_2+(1.25-x_2+K)m, \tag{12}$$

where $K=[(a-a_w)/m]+x_\Sigma$ is the reduction coefficient of the addendum heights.

At this type of correction due to changes in values of a_w, α_w, r_{w1}, r_{w2}, r_{a1}, r_{a2}, some formulas for calculation of geometrical parameters will have a changed structure **[21]** and **[22]**, compared to uncorrected gears.

In practice, for a positive correction $x_\Sigma>0$ the inversely proportional method of resolution of x_Σ is often used **[22]**:

$$x_1=\frac{z_2}{z_1+z_2}x_\Sigma,\quad x_2=x_\Sigma-x_1. \tag{13}$$

At height correction, the centre distance will not change, unlike the angular correction.

2 RESULTS OF THE SOLUTION, DISCUSSION

Data for calculation: $T_{nom}=4000$ Nmm, $n_1=700$ rpm; $B=420000$ revolutions (10 hours of operation) the size of the block with constant conditions of tribocontact; $K_g=1.2$; $m=4$ mm, $u=3$ gear ratio, $z_1=20$, $z_2=60$, $b=50$ mm, $h_{2*}=0.5$ mm acceptable teeth wear of the polymer gear.

Hight correction: $x_1=-x_2=0$, 0.1, 0.2, 0.3; $a=160$ mm; $\alpha=20°$. Angular correction:$x_\Sigma=0.3$; $x_1=0$, $x_2=0.3$; $x_1=0.05$, $x_2=0.25$; $x_1=0.1$, $x_2=0.2$; $x_1=0.2$, $x_2=0.1$; $x_1=0.25$, $x_2=0.05$; $a_w=161.169$ mm; $\alpha_w=21.11°$. The recommended values of the shift coefficients for the specified number of teeth in the case of angular correction are $x_1=0.225$, $x_2=0.075$.

The characteristics of materials of MP gears:

- Pinion: carbon steel 0.45%C, normalizing, grinding, $E_1=2.1\cdot10^5$ MPa, $\nu_1=0.3$; $C_1=10^9$, $m_1=2$, $\tau_{S1}=365$ MPa.
- Gear: polyamide PA6, $E_2=2300$ MPa, $\nu_2=0.4$; $C_2=1.34\cdot10^6$, $m_2=1.15$, $\tau_{S2}=40$ MPa; $f=0.23$; polyamide composite PA6+30CF, filled with 30 % fine carbon fiber, $E_2=3300$ MPa, $\nu_2=0.41$; $C_2=3.67\cdot10^6$, $m_2=1.15$, $\tau_{S2}=40$ MPa; $f=0.25$.

The wear resistance of materials of metal-polymer tribocouples was established according to the pin-on-disk scheme in the conditions of dry friction according to the ISO 7148-2 standard ($T=23\pm1$ °C, relative humidity of air 50 ± 5 %) **[27]**.

The results of research of height and angular correction influence on initial maximum contact $p_{j\max}$ and wear contact $p_{jh\max}$ pressures in engagement, linear wear h_{2j} of gear teeth, minimum gears resource $t_{B\min}$ are given in Figs. 2 to 6. Figs. 2 and 3 show the pressure level $p_{j\max}$ in the meshing cycle for both types of correction. To the left and right are the areas of two-pair engagement (input and output), and in the centre, the area of one-pair engagement. Here $\Delta\varphi$ is the angle of rotation of the pinion tooth from the point of the entry of the teeth into the engagement ($p.0$) to the next points with the selected step.

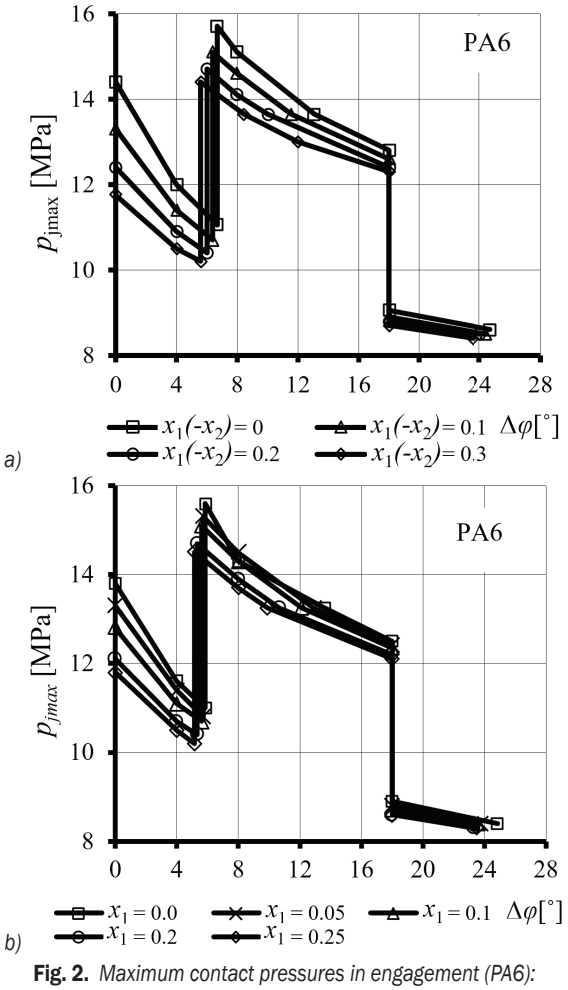

Fig. 2. *Maximum contact pressures in engagement (PA6): a) height correction [$x_1(-x_2)\equiv(x_1=-x_2)$], b) angular correction*

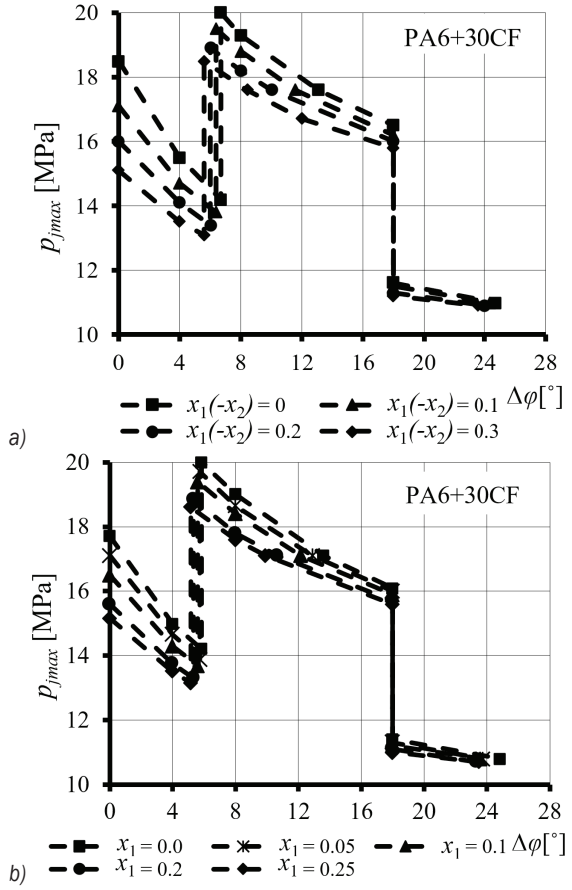

Fig. 3. *Maximum contact pressures in engagement (PA6+30CF): a) height correction, b) angular correction*

The obtained results of calculations show that at the entrance to the one-pair engagement, the initial contact pressures $p_{j\max}$ reach the highest value. When the teeth are corrected, the contact pressures will decrease in different ways during the meshing process. At the entrance to the two-pair engagement up to 1.23 times for the height correction and up to 1.17 times for the angular correction, and then up to 1.14 times. In the area of one-pair engagement, the pressure drop due to tooth correction will be smaller. Instead, in the initial area of two-pair engagement, the pressure drop will be much less noticeable. The specified qualitative regularities of reduction of the initial maximum contact pressures in engagement of MP gears at both types of correction are close irrespective of a type of polymeric materials. In terms of quantification, the pressures will be about 1.29 times higher in the gears with a gear made of PA6 + 30CF than with a gear made of PA6 at different values of the shift coefficients. When the engagement is corrected, the angle of entry into the one-pair engagement and the pitch point are shifted to the left. With both types of correction, the pressure level in the pitch point will not change.

The wear of the gear teeth of the corrected gears leads to a certain differentiated reduction of pressures $p_{j\max}$ in the engagement. For the example of the gears with height correction trends of these changes are shown in Fig. 4. The figure shows the trends of these changes on the example of the gears with height correction.

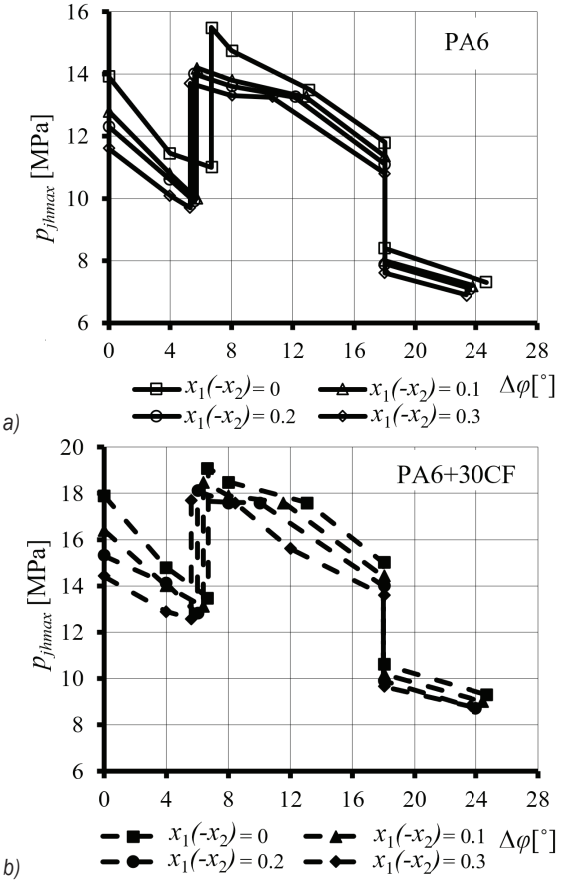

Fig. 4. *Maximum wear contact pressures: a) PA6, b) PA6+30CF*

The smallest decrease in $p_{j\max}$ (up to 1.053 times) is observed in the input area of engagement and in the transition to the central region. In contrast, at the exit from the central region the duction will be up to 1.15 times and much more up to 1.24 times at the exit from its right region. Wear-contact pressures at angular correction have similar quantitative and qualitative laws, as in case of height correction.

Correction of the engagement affects the course of linear wear h_{2j} of the gear polymer teeth in different ways at selected points of their profile. The research results are shown in Fig. 5.

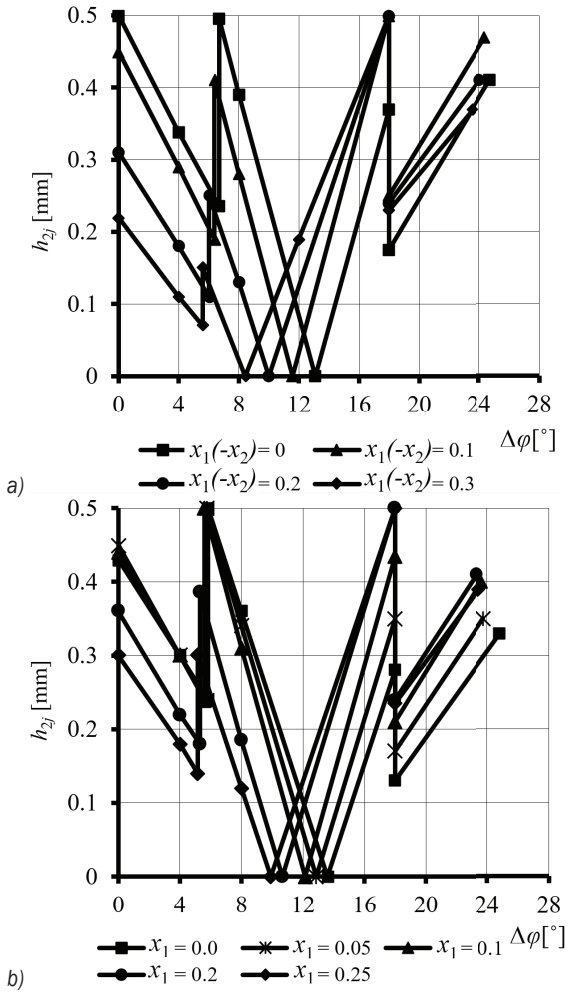

Fig. 5. *Linear wear of the teeth profile of the polymer gears during engagement: a) height correction, b) angular correction*

Correction of engagement leads to changes in tooth wear at characteristic points: at the entrance to the left area of two-pair engagement, at the entrance to the area of one-pair engagement, at the exit from it, and at the exit from the right area of two-pair engagement. In all cases of height correction, the acceptable wear is achieved at the exit of the teeth from the area of one-pair engagement. For angular correction, the acceptable wear is achieved at the point of entrance of the teeth into one-pair engagement at x_1 = 0, 0.05, 0.1, and at x_1 = 0.2, 0.25 the acceptable wear is achieved at the exit from this engagement. As already noted, the correction leads to a shift of the pitch point to the left, which is clearly seen in the figures because here the wear of the teeth is close to zero. This is because the slippage speed at the pitch point is almost zero.

The estimated minimum resource $t_{B\min}$ of MP gears for both types of correction and the studied gear materials is shown in Fig. 6. Of the gears resource determined at all characteristic points of engagement, the minimum will be that where the accepted allowable wear of the gear teeth is achieved (Fig. 5).

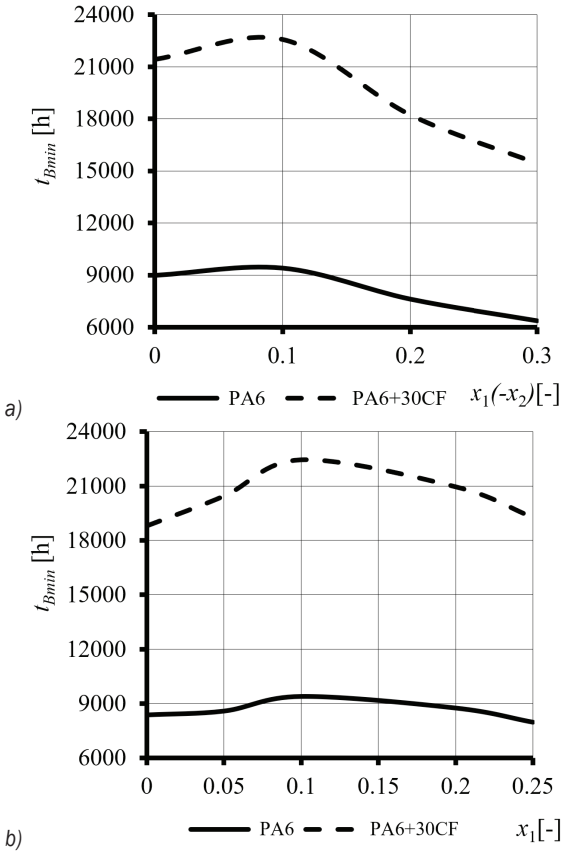

Fig. 6. *Influence of the teeth correction on the minimum resource $t_{B\min}$ of MP gears at a teeth inclination: a) height correction, b) angular correction*

The gears with a gear made of PA6 + 30CF will have a significantly higher resource $t_{B\min}$ than a gears with a gear made of PA6 in the whole range of shift coefficients. It is 2.4 times larger at the optimal values of the shift coefficients of height correction $x_1 = -x_2 = 0.1$ and angular correction $x_1 = 0.1$, $x_2 = 0.2$. Therefore, the results show that the correction of the engagement in relation to the gears resource will be most effective at these coefficients. It should be noted that with these optimal shift coefficients, the gears resource with height correction increases about 1.05 times, and with angular correction in 1.1 times (gear made of PA6) and in 1.22 times (gear made of PA6+30CF. A comparison of the effectiveness of engagement correction by both methods shows that at height correction at $x_1 = -x_2 = 0.126$ the gears resource will be lower than at $x_1 = -x_2 = 0$. That is, in the future such

correction will not make sense given the reduction of gears resource. Instead, with angular correction in the gears at $x_1=0.3$, $x_2=0$, its resource will be the same as the uncorrected gears. For the angular correction in the case of normative distribution of coefficients $x_1=0.225$, $x_2=0.075$, the gears resource will be somewhat higher, as at $x_1=0$, $x_2=0.3$, but less in 1.13 times than at the optimal values of the coefficients $x_1=0.1$, $x_2=0.2$. Presented in Fig. 6, the nature of the hange in the gears resource indicates that the pre-optimal shift coefficients are better for height correction, and the post-optimal are better for angular correction.

The results of this type of analytical research realize the possible optimization of gears by three criteria:

1) The load carrying capacity of the gears by $p_{\max}$ or $p_{h\max}$.
   This confirms the well-known trend that the correction of engagement leads to a decrease in the level of $p_{\max}$, and the above also shows their change during tooth wear. Contact pressures will be lowest at the highest values of the shift coefficients.
2) Linear wear h_{2j} of the tooth profile
   Given this criterion, larger coefficients are more rational for height correction $x_1=-x_2$ or angular correction x_1. Then the acceptable wear will not be at the entrance to the two-pair engagement, as is the case of uncorrected gears, but at the exit of the teeth from the one-pair engagement or at the entrance to it.
3) Gears resource $t_{B\min}$
   As established, the longest life of corrected gears will be achieved with the specified optimal shift coefficients. Since the service life of the gears is its most important characteristic from a practical point of view, the other two criteria will be subordinate. It should be noted that with the specified optimal shift coefficients, the second criterion will actually be provided as well.

3 CONCLUSIONS

1. The initial maximum contact pressures $p_{j\max}$ in the studied MP gears with height and angular correction have converged quantitative and qualitative patterns of change during the cycles of two-one-two-pair engagement. Correction of teeth has the most significant effect on their reduction in the entrance area of two-pair engagement, and less in one-pair engagement. The contact pressure in the gears with a gear made of PA6 + 30CF will be 29 % higher than with a gear made of PA6 regardless of the shift coefficients. Due to the wear of the polymer gear teeth, there is no noticeable effect on the change of initial pressures $p_{j\max}$ in the first and second areas of engagement. Instead, such a change in pressure is more significant in the initial region of two-pair engagement. Quantitative and qualitative patterns of changes in wear and contact pressures are similar in both types of tooth correction.
2. The linear wear h_{2j} of the polymer gear teeth profiles depends not only on the specific friction force (nonlinear) and sliding speed (linear), which are variable at each point of contact, but also on the number of pairs of teeth simultaneously engaged. Therefore, it systematically changes with successive contact of the teeth during their rotation, reaching the acceptable value of h_{2*} at any of the three characteristic points: at the entrance to the two-pair engagement, at the entrance or exit of the one-pair engagement. This fact depends on the combination of the shift coefficients. In fact, for both types of correction, the maximum wear h_{2*} will be achieved at the edges of one-pair engagement
3. Along with the contact teeth strength, which must be ensured when designing uncorrected gears according to ISO 6336: 2006-10, DIN 3990: 1987-12 **[1]** and **[2]** for calculating the load capacity of gears with metal toothed wheels or also the recommendations of VDI 2736 Blatt 2:2014-06: 2014 **[28]** for thermoplastic gears, from a practical point of view, the most desirable tribotechnical parameter is their forecast resources. According to the developed calculation method of research of MP gears, such estimation of resources was carried out both for uncorrected, and for corrected gears. Accordingly, both quantitative and qualitative patterns of the impact of height and angular correction of engagement on the resource are established above. It is shown that there are optimal shift coefficients that provide a higher gears life compared to uncorrected gears. Also, expedient areas of shift coefficients values at height and angular correction are established. In fact, this method can be a reasonable basis for the rational choice of shift coefficients, both metal and metal-polymer gears.
4. It should be noted that it is known from practice that, as a result of the increased bending of the teeth of polymer composite gears, a positive effect arises, which consists in an increased area of two-pair engagement, that is, in an increase

in the overlap coefficient. Moreover, this should lead to some reduction of the contact pressures at the entrance to the one-pair engagement. Perhaps they will then have values close to or lower than the pressures at the entrance to the two-pair engagement (Figs. 1 and 2). Due to the reduction of the maximum contact pressures, the gears resources will increase. The method of calculating MP gears developed by us does not take into account the influence of tooth deflection on the studied contact and tribocontact parameters. However, based on it, it is possible to carry out their full-scale quantitative and qualitative analysis, which has not yet been carried out by other researchers. Its results should be interpreted as reflecting worse conditions of contact and wear-contact interaction of teeth in engagement. The deflection of the teeth in the actual state of engagement of MP gears even improves in view of the above-mentioned typical geometric condition.

4 REFERENCES

[1] ISO 6336:2006-10 (2006). *Calculation of Load Capacity of Spur and Helical Gears*. International Organization for Standardization, Geneva

[2] DIN 3990:1987-12 (1987). *Trägfähigkeitsberechnung von Stirnrädern, Einführung und allgemeine Einflussfaktoren*. Deutsches Institut für Normung, Berlin.

[3] Brauer, J., Andersson, S. (2003). Simulation of wear in gears with flank interference - a mixed FE and analytical approach. *Wear*, vol. 254, no. 11, p. 1216-1232, **DOI:10.1016/S0043-1648(03)00338-7**.

[4] Flodin A., Andersson S. (1999). Wear simulation of spur gears. *Tribotest*, vol. 5, no. 3, p. 225-250, **DOI:10.1002/tt.3020050303**.

[5] Flodin, A. Andersson, S. (2001). A simplified model for wear prediction in helical gears. *Wear*, vol. 249, no. 3-4, p. 285-292, **DOI:10.1016/S0043-1648(01)00556-7**.

[6] Hooke, C.J., Kukureka, S.N., Liao, P., Rao, M., Chen, Y.K. (1996). The friction and wear of polymers in non-conformal contacts. *Wear*, vol. 200, no. 1-2, p. 83-94, **DOI:10.1016/S0043-1648(96)07270-5**.

[7] Keresztes, R., Kalacska, G. (2008). Friction of polymer / steel gear pairs. *Plastics and Rubber*, vol. 45, p. 236-242.

[8] Cathelin, J., Letzelter, E., Guingand, M., De Vaujany, J.P., Chazeau, L. (2013). Experimental and numerical study a loaded cylindrical PA66 gear. *Journal of Mechanical Design*, vol. 135, no. 4, p. 89-98, **DOI:10.1115/1.4023634**.

[9] Shil'ko, S.V., Starzhinskii, V.E. (1993). Prediction of Wear Resistance of Gearing with Wheels Made of Reinforced Composites. *Journal of Friction and Wear*, vol. 14, no. 3, p. 7-13.

[10] Shil'ko, S.V., Starzhinsky, V.E., Petrokovets, E.M, Chernous, D.A. (2013). Two-level calculation method for tribojoints made of disperse-reinforced composites: Part 1. *Journal of Friction and Wear*, vol. 34, p. 65-69, **DOI:10.3103/S1068366613010133**.

[11] Kahraman, A., Bajpai, P., Anderson, N.E. (2005). Influence of tooth profile deviations on helical gear wear. *Journal of Mechanical Design*, vol. 127, no. 4, p. 656-663, **DOI:10.1115/1.1899688**.

[12] Pasta, A., Mariotti Virzi, G. (2007). Finite element method analysis of a spur gear with a corrected profile. *The Journal of Strain Analysis for Engineering Design*, vol. 42, no. 5, p. 281-292, **DOI:10.1243/03093247JSA284**.

[13] Zwolak, J., Martyna, M. (2011). Analysis of contact stress and bending stress occuring in tooths of gear transmission power shifts. *Tribologia*, vol. 42, no. 3, p. 155-165. (in Polish)

[14] Zwolak, J., Wittek, M. (2011). Optimization of the geometrical parameters of toothed gears in the aspect of contact stress minimization. *Tribologia*, vol. 45, no. 6, p. 283-291. (in Polish)

[15] Miler, D., Loncar, A., Žeželj, D., Domitran, Z. (2017). Influence of profile shift on the spur gear pair optimization. *Mechanism and Machine Theory*, vol. 117, p. 189-197, **DOI:10.1016/j.mechmachtheory.2017.07.001**.

[16] Bodzás, S. (2019). Analysis of the effect of the addendum modification coefficient for contact surfaces of spur gear. *Journal of Mechanical Engineering*, vol. 69, no. 1, p. 5-16, **DOI:10.2478/scjme-2019-0001**.

[17] Okorn, I., Nagode, M., Klemenc, J. (2021). Operating Performance of External Non-Involute Spur and Helical Gears: A Review. *Strojniški vestnik - Journal of Mechanical Engineering*, vol. 67, no. 5, p. 256-271, **DOI:10.5545/sv-jme.2020.7094**.

[18] Chernets, M. (2019). Method of calculation of tribotechnical characteristics of the metal-polymer gear, reinforced with glass fiber, taking into account the correction of tooth. *Maintenance and Reliability*, vol. 21, no. 4, p. 546-552, **DOI:10.17531/ein.2019.4.2**.

[19] Czerniec, M., Kornienko, A. (2020). Prediction of the service life of metal-polymer gears made of glass and carbon fibre-reinforced polyamide, considering the impact of height correction. *Advances in Science and Technology Research Journal*, vol. 14, no. 3, p. 15-21, **DOI:10.12913/22998624/124553**.

[20] Chernets, M.V., Kelbinski, J. (2004). Computional evaluation of the wear and service life of helical involute cylindrical gears. *Problems of Tribology*, no. 3, p. 104-112.

[21] Chernets, M.V., Kelbinski, J., Yarema, R.Ya. (2011). Generalized method for the evaluation of cylindrical involute gears. *Materials Science*, vol. 47, p. 45-51, **DOI:10.1007/s11003-011-9366-9**.

[22] Chernets, M.V., Yarema, R.Y., Chernets, Y.M. (2012). A method for the evaluation of the influence of correction and wear of the teeth of a cylindrical gear on its durability and strength. Part 1. Service life and wear. *Materials Science*, vol. 48, p. 289-300, **DOI:10.1007%2Fs11003-012-9505-y**.

[23] Chernets, M.V., Yarema, R.Y., Chernets, Y.M. (2013). A method for the evaluation of the influence of correction and wear of the teeth of a cylindrical gear on its durability and strength. Part 2. Contact strength. *Materials Science*, vol. 48, p. 752-756, **DOI:10.1007/s11003-013-9565-7**.

[24] Chernets, M.V., Chernets, J.M. (2016). Evaluation of the strength, wear, and durability of a corrected cylindrical involute gearing, with due regard for the engagement conditions. *Journal of Friction and Wear*, vol. 37, p. 71-77, **DOI:10.3103/S1068366616010050**.

[25] Chernets, M., Chernets, J. (2017). The simulation of influence of engagement conditions and technological teeth correction on contact strength, wear and durability of cylindrical spur gear of electric locomotive. *Proceedings of the Institution of Mechanical Engineers, Part J: Journal of Engineering Tribology*, vol. 231, no. 1, p. 57-62, **DOI:10.1177%2F1350650116645024**.

[26] Chernets, M., Kornienko, A., Chernets, Y., Fedorchuk, S. (2021). Modelling of contact and tribotechnical parameters of metal-polymer gears taking into account wear and correction of teeth. *Proceedings of the Institution of Mechanical Engineers, Part J: Journal of Engineering Tribology*, vol. 236, p. 1263-1272, **DOI:10.1177/13506501211054683**.

[27] ISO 7148-2: 2012. *Plain Bearings - Testing of the Tribological Behaviour of Bearings Materials. Part 2. Testing of Polymer - Based Bearing Materials*. International Standard Organizytion, Geneva.

[28] VDI 2736 Blatt 2:2014-06: 2014. Thermoplastische Zahnräder - Stirnradgetriebe - Tragfähigkeitsberechnung. Deutsches Institut für Normung, Berlin.

Vsebina

Strojniški vestnik - Journal of Mechanical Engineering
letnik 68, (2022), številka 11
Ljubljana, november 2022
ISSN 0039-2480

Izhaja mesečno

Razširjeni povzetki (extended abstracts)

Strojniški vestnik - Journal of Mechanical Engineering 68(2022)11, SI 85

Prejeto v recenzijo: 2022-06-25
Prejeto popravljeno: 2022-09-06
Odobreno za objavo: 2022-10-04

Konstruiranje filtrov za montažo, optimizacija varjenja in terenski preizkusi

Hakan Maden[1,*] – Kerim Çetinkaya[2]

[1] Ihlas Home Appliance, Turčija

[2] Univerza Antalya AKEV University, Fakulteta za umetnost in dizajn, Turčija

Pokrov in deli ohišja cevnih filtrov za hišne vodne čistilne naprave se spajajo po postopku rotacijskega varjenja z gnetenjem. Pri varjenju z gnetenjem prihaja do zbiranja delcev delno raztaljenega materiala na notranji in zunanji strani območja zvara, ti pa povzročajo mašenje sedimentnega filtra in zmanjšanje pretoka vode. Omenjeni delci na notranjem delu filtra z aktivnim ogljem odtečejo na klobučevino na zgornjem pokrovu in zmanjšajo uporabno površino klobučevine za 30 %. Članek obravnava odpravo težav z mašenjem filtrov in podaljšanje njihove življenjske dobe z lovljenjem nakopičenih delcev v notranjosti. Zaradi napak pri brizganju in montaži plastičnih delov sedimentnih filtrov in filtrov z aktivnim ogljem prihaja po rotacijskem varjenju z gnetenjem do kopičenja raztaljenega materiala, ki lahko zapre vodne kanale v zgornjem delu pokrova filtra proti klobučevini. Za kontrolo kakovosti se uporablja zrak in izdelek je sprejemljiv, če kanali niso popolnoma zamašeni. Po vgradnji pri stranki pa lahko nato nastopijo težave z majhnim pretokom vode ali prehitrim mašenjem filtrov.

V programu ABAQUS so bili določeni parametri za simulacijo toka skepljenih delno raztaljenih delcev, ki nastanejo po varjenju. Rezultati analize so pokazali, da je kopičenje delcev omejeno na predvideno območje. Orodje za brizganje plastike je bilo zato treba ustrezno prilagoditi izvajanju testov in kontroli profila zvarnega spoja. Po varjenju je bil narejen izrez, ki je bil nato pregledan. Kopičenje delcev na notranji strani ni bilo opaženo.

Nastavitve stroja za varjenje z gnetenjem so vsaj tako pomembne za kakovost spoja pokrova cevnega filtra kot zasnova varjene konstrukcije. Za določitev optimalnih parametrov stroja za varjenje je bila uporabljena eksperimentalna metoda po Taguchiju. Optimalne vrednosti so: vrtilna frekvenca 2490 obr./min, tlak 6 bar, čas varjenja 2 s in čas hlajenja 4 s.

Trdnost ustvarjenega zvarnega spoja presega želeno raven v statičnih tlačnih preizkusih. Tudi pri visoki statični trdnosti pa je lahko dinamična tlačna trdnost nezadostna. Za preučitev omenjene lastnosti je bil opravljen dinamični preizkus delov. Izdelana je bila pilotna serija s 1500 filtri, varjenimi z gnetenjem, ki bodo pri kupcih uporabljeni v različnih vremenskih pogojih in pri različnih tlakih vodovodnega omrežja. Preizkušeno bo tesnjenje vode, nastajanje razpok v predelu zvara, deformacije filtrov in ali spremembe resnično prinašajo izboljšave.

V okviru študije so bila izdelana orodja in brizganci z razvito konstrukcijo za varjenje z gnetenjem. Z eksperimentalno metodo po Taguchiju in z analizo ANOVA parametrov stroja za varjenje so bile pridobljene spodnje vrednosti. (i) Parametri varjenja z gnetenjem za maksimalno trdnost so: vrtilna frekvenca 2490 obr./min, tlak 6 bar, čas varjenja 2 s in čas hlajenja 4 s. (ii) Vrtilna frekvenca ima 42,74-odstotni vpliv na kakovost zvara. (iii) Izdelani so bili ustrezni deli z optimalnimi parametri za statični in dinamični preizkus.

Opravljeni so bili terenski preizkusi za preverjanje izboljšav z razvitim profilom zvarnega spoja. Frekvenca potrebnih menjav zaradi kopičenja delno raztaljenih delcev v notranjosti sedimentnih filtrov in filtrov z aktivnim ogljem se je zmanjšala na nič.

V opisani študiji je bilo obravnavano samo rotacijsko torno varjenje. V preteklosti je bilo opravljenih že veliko analiz in simulacij spajanja kovinskih delov po postopku varjenja z gnetenjem, v pregledu literature pa je bilo najdenih le malo objav o plastičnih delih. S pomočjo programa za analizo po metodi končnih elementov ABAQUS je bila razvita nova konstrukcija zvarnega spoja za plastične dele. Orodja za brizganje plastike so bila popravljena glede na profil novega zvarnega spoja in izdelani so bili brizganci. Za določitev parametrov stroja za varjenje z gnetenjem je bila uporabljena optimizacijska metoda po Taguchiju. Določene so bile optimalne vrednosti parametrov stroja in njihov vpliv na kakovost zvarov. Uspešnost razvoja je bila preverjena s terenskimi preizkusi in izkazalo se je, da so bile težave zaradi kopičenja delno raztaljenih delcev v celoti odpravljene. V prihodnje bo obravnavano še kopičenje delcev na zunanjem delu. Razvoj profila zvarnega spoja odpira tudi možnosti za izdelavo cevnih membranskih filtrov.

Ključne besede: rotacijsko varjenje z gnetenjem, eksperimentalna metoda po Taguchiju, analiza ANOVA, kopičenje delno raztaljenih delcev, čiščenje vode NSF, analiza po metodi končnih elementov, terenski preizkus, statično in dinamično preizkušanje

*Naslov avtorja za dopisovanje: Ihlas Home Appliance, Istanbul, Turčija, hakanmaden74@gmail.com

Strojniški vestnik - Journal of Mechanical Engineering 68(2022)11, SI 86

Prejeto v recenzijo: 2022-06-02
Prejeto popravljeno: 2022-08-09
Odobreno za objavo: 2022-10-13

Dinamični model togo-hiperelastične sklopitve in dinamične lastnosti vzmetnega vlečnega robota

Jianguo Zhao[1,2,3,*] – Binfan Wang[1,3] – Qingyou Liu[1,3] – Guorong Wang[1,3] – Xiangfeng Zeng[4]

[1] Šola za mehatroniko, Jugozahodna univerza za naftno industrijo, Kitajska
[2] Laboratorij za procesno opremo in krmiljenje province Sečuan, Kitajska
[3] Inštitut za energetsko opremo, Jugozahodna univerza za naftno industrijo, Kitajska
[4] Yunnan Shuifu Yuntianhua Co., Ltd, Kitajska

V članku je podan predlog elastičnega sidrnega mehanizma za teleskopske vlečne robote, ki preprečuje obtičanje v vrtini v primeru nezgode (npr. izpada električnega napajanja, odpovedi krmiljenja elektromagnetnih ventilov). Z optimizacijo konstrukcije vzmetne sidrne roke je bila dosežena funkcija samodejnega odpenjanja.

Glavni cilj je bil preverjanje izvedljivosti in ustreznosti zasnove vlečnega robota s simulacijo modela dinamike in eksperimenti na prototipu. Z mehansko analizo modela sidrnega mehanizma so bile pridobljene enačbe elastične povratne sile sidrne roke kot osnova za prihodnje študije. Elastična povratna sila in največje napetosti v vzmetni sidrni roki z različnimi velikostmi konstrukcije so bile določene s simulacijami v paketu ABAQUS, cilj pa je bil oblikovanje optimalne konstrukcije sidrne roke. Z uporabo paketov ABAQUS in ADAMS za kosimulacijo je bil postavljen dinamični model togo-hiperelastične sklopitve za analizo dinamičnih lastnosti vlečnega robota. Izdelan je bil prototip z optimalno konstrukcijo vzmetne sidrne roke za preverjanje rezultatov teoretičnih raziskav in simulacij. V članku je bila uporabljena zasnova mehanske konstrukcije, mehanska analiza, analiza po metodi končnih elementov in simulacija dinamičnega modela za validacijo izvedljivosti in ustreznosti konstrukcije vlečnega robota.

Rezultati, ugotovitve:

1. Predstavljen je predlog novega vzmetnega sidrnega mehanizma za vlečne robote z nagnjenimi bloki, ki zagotavlja veliko vlečno silo in preprečuje obtičanje.
2. Opravljena je bila mehanska analiza procesa vleke in optimizacija konstrukcije vzmetnega sidrnega mehanizma.
3. S simulacijo modela togo-hiperelastične sklopitve je bila določena največja vlečna sila pri različnih konstrukcijskih parametrih.
4. Eksperimenti so pokazali vrednost največje vlečne sile 14.262 N, oz. 4,9-odstotno razliko glede na rezultate simulacij. Ustreznost teoretične maksimalne vlečne sile je bila preverjena eksperimentalno.

S člankom je zaključena zasnova konstrukcije in delovnega mehanizma vlečnega robota ter dokončana optimizacija konstrukcije vlečnega robota. Vrednosti največje vlečne sile so bile določene pri različnih parametrih konstrukcije in eksperimentalno potrjene na prototipu. Rezultati raziskave so skladni s pričakovanji, manjkajo pa še nadaljnje študije hitrosti vleke navitih cevi in orodij v vrtino, ki bodo lahko predmet prihodnjih raziskav.

V članku je predstavljen predlog novega vzmetnega sidrnega mehanizma za vlečne robote z nagnjenimi bloki. Sidrni mehanizem lahko samodejno odpne elastična povratna sila vzmetne sidrne roke, da ne bi prišlo do zapore vrtine. Konstrukcija vzmetnega sidrnega mehanizma je optimizirana. Določene so največje vlečne sile pri različnih parametrih konstrukcije. Rezultati raziskav v tem članku bodo lahko osnova za konstrukcijsko zasnovo in tehnično uporabo vzmetnih vlečnih robotov. Ta lahko učinkovito zagotavlja varnost v naftnih in plinskih vrtinah.

Ključne besede: vzmetni vlečni robot, dinamični model togo-hiperelastične sklopitve, optimizacija konstrukcije, sidranje, dinamične lastnosti

*Naslov avtorja za dopisovanje: Šola za mehatroniko, Jugozahodna univerza za naftno industrijo, Chengdu 610500, Kitajska, zhaojianguo_1@qq.com

Strojniški vestnik - Journal of Mechanical Engineering 68(2022)11, SI 87

Prejeto v recenzijo: 2022-08-08
Prejeto popravljeno: 2022-10-01
Odobreno za objavo: 2022-10-17

Optimizacijske tehnike za načrtovanje zelene prostorske razmestitve opreme v proizvodni industriji: metahevristična analiza

Sheik Sulaiman Sherfudeen[1,*] – Muthiah Athinamilagi[2] – Janakiraman Venkataramanujam[3]

[1] Tehniški kolidž Francis Xavier, Oddelek za strojništvo, Indija
[2] Tehniški kolidž P.S.R., Oddelek za strojništvo, Indija
[3] Tehniški kolidž Vaigai, Oddelek za strojništvo, Indija

Cilj pričujočega raziskovalnega projekta je iskanje optimalne prostorske razmestitve strojev v delavnicah za izboljšanje produktivnosti delavcev in opreme s povečanjem učinkovitosti potekov dela. Namen je tudi ustvariti do uporabnikov najprijaznejšo zeleno prostorsko razmestitev tovarne z najnižjimi emisijami CO_2. Zastavljeni so bili naslednji cilji: (i) kreiranje strategij na področju transporta in načrtovanja poti za uravnoteženje emisij CO_2 in skupnih stroškov ravnanja z materialom (TMHC) na najboljši možen način, (ii) zasnova najboljše prostorske razmestitve za upravljanje s surovinami za proizvodnjo med terminali ob upoštevanju razdalje med oddelki, (iii) znižanje skupnih emisij CO_2 po metodi adaptivne optimizacije kolonije plaščarjev (ASSO), in (iv) primerjava rezultatov pri doseganju ciljev z modelom ASSO in na podlagi različnih pristopov, kot so ABC, DFO, SA in GA.

Glavni cilj raziskave je bilo ustvarjanje in vrednotenje iskalnih hevristik za identifikacijo rešitev problema prostorske razmestitve obratov v proizvodni industriji, ki bodo bližje optimalnim. Ločimo tri vrste omejitev za zmanjšanje skupnih emisij vozil in skupnih transportnih stroškov: načrtovanje poti, kapaciteta vozil in urniki. Do okolja prijazna zasnova prostorske razmestitve ima v primerjavi z drugimi optimizacijskimi metodami minimalno, 25-odstotno stopnjo emisij in 50-odstotni TMHC.

Zmanjšanje celotnega pretoka in rabe energije v različnih oddelkih je pozitivno korelirana z ASSO. Nastali operativni načrti so tako najbolj ekonomični in obenem znižujejo emisije CO_2.

Rezultati in ugotovitve:

- Metodologija ASSO je najučinkovitejša s 40-odstotnim zmanjšanjem THMC v primerjavi z ABC, 38 % z DFO, 50 % z SA in 40 % z GA. Povprečno zmanjšanje emisij pri zeleni prostorski razmestitvi je 20-odstotno.
- V študiji so bili preučeni trije glavni viri emisij CO_2 v industriji: TMHC v zvezi s prometom med oddelki, emisije zaradi porabe plina in emisije zaradi porabe električne energije.
- Metoda ASSO ločuje dve različni poti kolonij z nizom identitet strank, ki določa vrstni red dobav oz. ruto vozila.

V prihodnje bo z različnimi optimizacijskimi tehnikami obravnavana ciljna funkcija za probleme zelene logistike. Izboljšani hibridni algoritmi bodo prilagojeni malim in srednjim podjetjem.

Ključne besede: adaptivna optimizacija kolonije plaščarjev, dvociljna funkcija, emisije, evolucijsko računanje, zasnova prostorske razmestitve, skupni stroški ravnanja

*Naslov avtorja za dopisovanje: Tehniški kolidž Francis Xavier, Oddelek za strojništvo, Indija, sssulaiman1980@gmail.com

Strojniški vestnik - Journal of Mechanical Engineering 68(2022)11, SI 88

Prejeto v recenzijo: 2022-08-25
Prejeto popravljeno: 2022-11-02
Odobreno za objavo: 2022-11-07

Vpliv geometrije orodja v območju mešanja na oblikovanje kavljev pri varjenju dveh različnih aluminijevih zlitin: parametrična analiza metalurških in mehanskih lastnosti

Nandakumar Navaneethakannan* – Periyasamy Sivanandi – Balakrishnan Somasekaran
Vladni tehniški kolidž, Oddelek za strojništvo, Indija

Točkovno varjenje s trenjem in mešanjem (FSSW) je nedavno razvita tehnika spajanja v trdnem stanju, ki se uporablja za kombiniranje kovinskih zlitin s slabo varivostjo. Cilj pričujoče raziskave je analiza varivosti pri točkovnem varjenju dveh različnih aluminijevih zlitin s trenjem in mešanjem. Pri tej vrsti varjenja geometrija orodja in profil mešalnega čepa vplivata na metalurške in mehanske lastnosti varjencev.

Za boljše rezultate je zato treba poznati in izbrati optimalen profil mešalnega čepa. Glavna težava pri točkovnem varjenju s trenjem in mešanjem je oblikovanje kavljev. Sila, ki povzroča rinjenje materiala iz spodnje plasti navzgor, razvoj območij v obliki kavlja ter rast območja mešanja in širine spoja, se pojavi med časom zadrževanja zaradi penetracije rame orodja v površino zgornje plasti in penetracije čepa v spodnjo plast. Območja kavljev, ki nastanejo na preseku termomehansko vplivane cone (TMAZ) in toplotno vplivane cone (HAZ), se po formiranju odmaknejo od osi vrtečega se orodja. Tok materiala povzroča spremenljivo obliko kavljev. Geometrija kavljev sicer v veliki meri vpliva na mehanske lastnosti spojev FSSW, še vedno pa ni znano, kako bi bilo mogoče izboljšati geometrijo kavljev. Znano je, da temperatura in plastična deformacija materiala vplivata na makroskopski videz spoja FSSW. Na razvoj toplote zaradi trenja med varjenjem vplivajo naslednji parametri: vrtilna hitrost, čas zadrževanja, globina pogreznitve in hitrost pomika orodja v material. Prilagoditve varilnih parametrov lahko tako povzročijo spremembe v makroskopskem videzu.

V obsežnem eksperimentalnem delu študije je bilo opravljeno varjenje zlitin AA6063 in AA5083 po postopku FFSW. Na rezkalnem stroju so bila pripravljena vpenjala za različne velikosti varjencev. Uporabljena sta bila valjasta rama in konkaven profil (10°) kvadratnega čepa, varjenje pa je bilo opravljeno z različnimi procesnimi parametri. Za orodni material je bilo uporabljeno toplotno obdelano mnogogljično jeklo. Za eksperimentalni model je bilo izbrano ortogonalno polje Taguchi L9. Preučen je bil vpliv dejavnikov FSSW, kot so hitrost vretena, čas in globina, kakor tudi odvisnosti med natezno trdnostjo, trdoto v predelu stika in razvojem kavljev. S tem so bila zajeta osnovna metalurška dogajanja v coni varjenja med ploščami. Kavljasta struktura je bila odkrita v območju stika, termomehanski pojavi pa v območju točkovnega varjenja. Zaradi tokov materiala v smeri navzgor med fazo pogrezanja orodja se prekine stik. Oblikuje se kavelj, ki se postopoma rine navzgor. Kavelj nadaljuje z gibanjem v smeri nizkotlačnega predela, ki v fazi zadrževanja orodja obdaja cono mešanja. Za mehansko kakovost zvarov je težko jamčiti zaradi negotovosti glede napredovanja vrha razpoke vzdolž kavlja. Zvare s kljuko idealne oblike je mogoče izdelati pod pogojem, da konica kavlja ob zaključku varjenja še ne vstopi v nizkotlačno območje.

Izkazalo se je, da sta vplivni veličini hitrost vretena in globina pogreznitve. Boljše mehanske lastnosti so bile dosežene pri vrtilni hitrosti vretena 1200 obr/min, času 25 s in globini pogreznitve 0,10 mm. Mikrostrukturna analiza območja zvara je bila opravljena pod vrstičnim elektronskim mikroskopom. Hitrost vretena je obratovalni parameter, ki ima največji vpliv na trdnost zvarov plošč iz materialov Al6063-T6 in Al5083-O-H111. Čas zadrževanja je najpomembnejši dejavnik za obvladovanje trdote. Na trdoto vplivata tudi hitrost vretena in globina pogreznitve. Metalurška preiskava je pokazala, da je višina kavlja minimalna pri naslednjih varilnih parametrih: hitrost vretena 1000 obr/min, čas zadrževanja 25 s in globina 0,20 mm, prispevek parametrov pa znaša 4,2 % za vrtljaje, 66,23 % za čas in 15,75 % za globino. Povprečna širina kavlja se formira pri naslednjih parametrih: 2000 obr/min, 3 s in 0,10 mm, prispevek parametrov pa znaša 32,55 % za vrtljaje in 27 % za čas. Trdnost spoja je obratno sorazmerna z njegovo trdoto.

Ključne besede: mikrostruktura, geometrija kavlja, območje mešanja, tehnika Taguchi, multipla regresijska analiza, ANOVA

*Naslov avtorja za dopisovanje: Vladni tehniški kolidž, Oddelek za strojništvo, Indija, nandakumar@gct.ac.in

Strojniški vestnik - Journal of Mechanical Engineering 68(2022)11, SI 89

Prejeto v recenzijo: 2022-06-06
Prejeto popravljeno: 2022-08-18
Odobreno za objavo: 2022-08-18

Eksperimentalna analiza prenosnih lastnosti eliptičnih zobniških prenosnikov

Changbin Dong[1] – Wangpeng Pei[1] – Yongping Liu[1] – Yongqiao Wei*[,1,2] – Dawei Li[1] – Rui Guo[1] – Zhongtao Ren[1]

[1] Tehniška univerza v Landžovu, Šola za strojništvo in elektrotehniko, Kitajska
[2] Državni laboratorij za visokozmogljivo kompleksno obdelavo, Univerza srednjega juga, Kitajska

V članku je predstavljen predlog metode za analizo lastnosti prenosnikov na podlagi preizkusov, ki rešuje problem težavne analize lastnosti eliptičnih zobniških prenosnikov. Z njo bodo izboljšane možnosti za razvoj in uporabo omenjenih prenosnikov.

Zgrajeno je bilo preizkuševališče za eliptične zobniške prenosnike in iz zbranih rezultatov preskusov so bile izračunane lastnosti eliptičnih prenosnikov.

Na preizkuševališču, ki omogoča spreminjanje prestavnega razmerja eliptičnih zobniških prenosnikov, so bili zbrani podatki o ubiranju. Določeni so bili zakoni variabilnosti dinamične in statične zračnosti pri gibanju, torni moment in vibracije eliptičnega prenosnika v obratovalnih pogojih. Potrjeno je bilo, da so eliptični zobniški prenosniki primerni za majhne vrtilne hitrosti in velike momente.

Zaradi pomanjkanja ustreznih referenčnih raziskav in visokih stroškov gradnje preizkuševališč za eliptične prenosnike je na voljo le malo literature v zvezi z eksperimentalnimi raziskavami dinamičnih lastnosti eliptičnih prenosnikov. V članku je zato predstavljen predlog metode za analizo dinamičnih lastnosti eliptičnih zobniških prenosnikov na osnovi preizkusov. Rezultati raziskave bodo lahko teoretična osnova za izboljšave v tehničnih aplikacijah eliptičnih zobniških prenosnikov.

Ključne besede: eliptični zobniški prenosniki, preizkus transmisije, histerezne lastnosti, torni moment, vibracije

*Naslov avtorja za dopisovanje: Tehniška univerza v Landžovu, Šola za strojništvo in elektrotehniko, Gansu Lanzhou, 730050, Kitajska, scuwyq@163.com

Strojniški vestnik - Journal of Mechanical Engineering 68(2022)11, SI 90

Prejeto v recenzijo: 2022-06-20
Prejeto popravljeno: 2022-09-03
Odobreno za objavo: 2022-11-04

Primerjava nosilnosti, obrabe in obstojnosti korigiranih kovinsko-polimernih čelnih zobniških dvojic z večjim zobnikom iz poliamida PA6 oz. PA6+30CF

Myron Chernets[1] – Marek Opielak[2] – Anatolii Kornienko[1,*]

[1]Fakulteta za letalski in vesoljski inženiring, Nacionalna univerza za letalstvo, Ukrajina
[2]Tehniška univerza v Lublinu, Poljska

Cilj pričujoče raziskave je uporaba razvite analitične metode za določitev količinskih in kakovostnih zakonitosti v zvezi z vplivom korektur ubirne višine in kota, obrabe polimernih zob in stopnje prekritja na nosilnost, linearno obrabo zob in obstojnost kovinsko-polimernih (MP) zobniških dvojic z večjim zobnikom iz poliamida PA6 oz. PA6 + 30CF.

Avtorji so pri reševanju tega pomembnega znanstvenega in praktičnega problema uporabili rezultate svojih teoretičnih in eksperimentalnih triboloških študij. Opravljeni so bili tribološki eksperimenti s suhimi tornimi kombinacijami jeklo/poliamid PA6, PA6 + 30CF po metodi valjček na disku. Na podlagi rešitev tega kompleksnega problema so bile opredeljene količinske in kakovostne zakonitosti v zvezi z vplivom korektur, obrabe profila zob in pogojev ubiranja na nosilnost, linearno obrabo zob in obstojnost MP zobniških dvojic, ki so predmet raziskave.

Članek analizira tribološke lastnosti MP čelnih zobniških dvojic z manjšim zobnikom iz jekla in večjim zobnikom iz dveh vrst poliamida - neojačenega PA6 in ojačenega s kratkimi ogljikovimi vlakni PA6 + 30CF. Korektura zob povzroči zmanjšanje kontaktnega tlaka med ubiranjem v spremenljivi meri. To zmanjšanje je najbolj izraženo na začetku ubiranja dveh parov zob. Kontaktni tlak pri čelnih zobniških dvojicah z večjim zobnikom iz poliamida PA6 + 30CF je za 29 % višji kot pri večjem zobniku iz PA6 za vse vrednosti koeficientov profilnega premika, ne glede na tip.

Linearna obraba zob se spreminja med ciklom ubiranja, odvisna pa je od koeficientov premika in od stopnje prekrivanja. Pri obeh vrstah korektur je največja obraba prisotna na začetku in na koncu ubiranja enega para zob.

Ugotovljeno je bilo, da obstajajo optimalni koeficienti premika, ki v primerjavi z nekorigiranimi zobniki zagotavljajo daljšo obstojnost zobnikov. Določene so bile tudi primerne vrednosti koeficientov premika za višinske in kotne korekture. MP zobniške dvojice z večjim zobnikom iz PA6 + 30CF imajo znatno daljšo obstojnost kot dvojice z večjim zobnikom iz PA6.

Tovrstna računska metoda je nova, zato je bila uporabljena za konstrukcijsko vrednotenje delovnih lastnosti MP zobniških dvojic. Opisana kompleksna analitična metoda omogoča tudi optimizacijo MP zobniških dvojic po treh kriterijih:

1. Nosilnost zobnikov pri maksimalnih kontaktnih tlakih. Tlaki so manjši pri večjih vrednostih koeficientov premika.
2. Linearna obraba zob. Večji koeficienti premika so primernejši za višinske ali kotne korekture. Sprejemljiva obraba je v tem primeru prisotna na začetku ali na koncu ubiranja enega para zob.
3. Obstojnost zobnikov. Največja obstojnost korigiranih zobnikov je dosežena pri optimalni vrednosti koeficientov premika. S praktičnega vidika je najpomembnejša lastnost zobnikov prav obstojnost, zato sta ji ostala kriterija podrejena.

V razpoložljivi literaturi pa sicer ni bilo mogoče najti podobnih osnutkov predlaganega pristopa ali nastavkov, ki bi mu bili analogni.

Ključne besede: kovinsko-polimerna čelna zobniška dvojica, korektura ubirne višine in kota, poliamida PA6 in PA6 + 30CF, maksimalni kontaktni tlak, linearna obraba zob, obstojnost zobnikov

*Naslov avtorja za dopisovanje: Državna univerza za letalstvo, Lubomyr Huzar 1, 03680 Kijev, Ukraina, anatoliykor80@gmail.com